

Heterogeneous multi-sensor data fusion using geometric transformations and Parzen windows for the nondestructive evaluation of gas transmission pipelines

by

Joseph Anthony Ogaro

A Thesis Submitted to the
Graduate Faculty in Partial Fulfillment of the
Requirements for the Degree of
MASTER OF SCIENCE

Department: Electrical and Computer Engineering
Major: Engineering (Electrical Engineering)

Approved:

Members of the Committee:

In Charge of Major Work

For the Major Department

For the College

Rowan University
Glassboro, NJ
2004

TABLE OF CONTENTS

LIST OF FIGURES	iii
LIST OF TABLES	v
ACKNOWLEDGEMENTS	vi
ABSTRACT	1
CHAPTER 1: INTRODUCTION	2
1.1 Nondestructive Evaluation	3
1.2 Multi-sensor Data Fusion	11
1.3 Objectives of Thesis	15
1.4 Expected Contributions	16
1.5 Scope and Organization of Thesis	16
CHAPTER 2: BACKGROUND	18
2.1 Previous Work in Data Fusion for NDE	18
2.2 NDE Inspection Techniques	23
2.2.1 Ultrasonic Testing	23
2.2.2 Magnetic Flux Leakage	28
2.2.3 Acoustic Emission	31
2.2.4 Thermal Imaging	32
2.3 Geometric Transformations	33
2.3.1 Spatial Transformations	36
2.3.2 Gray-Level Interpolation	39
2.4 Density Estimation	41
2.4.1 Parzen Windows	44
2.4.2 K – Nearest Neighbors	47
CHAPTER 3: APPROACH	48
3.1 Definition of Redundant and Complementary Information	50
3.2 Dimensionality Transform using Parzen Windows	50
3.3 Geometric Transforms	51
CHAPTER 4: IMPLEMENTATION/RESULTS	57
4.1 Experimental Setup	57
4.1.1 Test Specimen Suite	57
4.1.2 Ultrasonic Scanning Test Setup	60
4.1.3 Magnetic Flux Leakage Test Setup	63
4.1.4 Thermal Imaging Test Setup	65

4.1.5	Acoustic Emission Test Setup	67
4.2	Results.....	71
4.2.1	Definition of Redundant and Complementary Information.....	71
4.2.2	Homogeneous Training and Test Datasets	72
4.2.2.1	Ultrasound and MFL Data Fusion Results.....	76
4.2.2.2	Thermal and Ultrasound Data Fusion Results	93
4.2.2.3	MFL and Thermal Data Fusion Results.....	111
4.2.3	Heterogeneous Data Fusion	129
4.2.4	Heterogeneous Training and Testing Datasets	132
4.2.4.1	Acoustic Emission and Ultrasound Data Fusion Results.....	134
4.2.5	Discussion of Results.....	137
CHAPTER 5: CONCLUSIONS		142
5.1	Summary of Accomplishments.....	143
5.2	Directions for Future Work.....	144
BIBLIOGRAPHY.....		146

LIST OF FIGURES

Figure 1.1: Inspection with single NDE technique.....	4
Figure 1.2: Multi-sensor NDE inspection.....	10
Figure 1.3: Block diagram of data fusion process.....	14
Figure 1.4: Redundant and complementary information extraction from two NDE sources.....	15
Figure 2.1: Through transmission ultrasonic testing.....	25
Figure 2.2: Pulse echo ultrasonic testing.....	25
Figure 2.3: B-scan and C-scan ultrasound data.....	26
Figure 2.4: Defect detection parameters.....	27
Figure 2.5: MFL inline inspection tool: the “Pig”.....	29
Figure 2.6: Magnetic flux lines through pipe wall.....	30
Figure 2.7: Acoustic emission process.....	31
Figure 2.8: Thermal imaging technique.....	33
Figure 2.9: Geometric transformation pixel mapping.....	34
Figure 2.10: Geometric transformation types.....	35
Figure 2.11: Spatial transformation on pixel level.....	36
Figure 2.12: Corresponding tie-points in quadrilateral regions of input and output images.....	37
Figure 2.13: Gray Level Interpolation using Nearest Neighbor Approach.....	40
Figure 2.14: Gaussians used as window Functions.....	46
Figure 3.1: Generalized approach for multi-sensor data fusion.....	49
Figure 3.2: Block diagram of the redundant data extraction RBF training process.....	55
Figure 3.3: Block diagram of the redundant data extraction RBF testing process.....	55
Figure 4.1: Homogeneous test specimen suite.....	58
Figure 4.2: Test specimens for AE inspection with biaxial and uniaxial loading.....	59
Figure 4.3: Ultrasonic testing station.....	61
Figure 4.4: UT C-scan TOF NDE signatures from test specimen suite 1: Dataset 1.....	61
Figure 4.5: UT C-scan TOF NDE signatures from test specimen suite 1: Dataset 2.....	62
Figure 4.6: UT C-scan amplitude NDE signatures from test specimen suite 2.....	62
Figure 4.7: Magnetic flux leakage testing system.....	63
Figure 4.8: Y-component MFL NDE signature for test specimen suite 1: Dataset 1.....	64

Figure 4.9: Y-component MFL NDE signature for test specimen suite 1: Dataset 2.....	64
Figure 4.10: Thermal imaging test setup.	65
Figure 4.11: Thermal images from test specimen suite 1: dataset 1.....	66
Figure 4.12: Thermal images from test specimen suite 1: dataset 2.....	66
Figure 4.13: Acoustic emission loading platform.....	67
Figure 4.14: Acoustic emission sensor placement.....	68
Figure 4.15: Acoustic emission dataset	70
Figure 4.16: Redundant and complementary data definitions between two NDE signatures	71
Figure 4.17: UT & MFL combination Trial 1.....	81
Figure 4.18: UT & MFL combination Trial 2.....	86
Figure 4.19: UT & MFL combination Trial 3.....	72
Figure 4.20: Thermal & UT combination Trial 1.	98
Figure 4.21: Thermal & UT combination Trial 2.	104
Figure 4.22: Thermal & UT combination Trial 3.	110
Figure 4.23: MFL & Thermal combination Trial 1.	116
Figure 4.24: MFL & Thermal combination Trial 2.	122
Figure 4.25: MFL & Thermal combination Trial 3.	128
Figure 4.26: K-means clustering on AE data of uniaxial specimen with 0.16” deep defect.....	130
Figure 4.27: Parzen windows density estimation of each class separately.....	130
Figure 4.28: Binary representation of Parzen windows AE images.	131
Figure 4.29: Defect location representation from AE data.	131
Figure 4.30: AE location estimation plots for the data fusion algorithm.....	132
Figure 4.31: AE & UT Combination Trial 1.....	135
Figure 4.32: AE & UT Combination Trial 2.....	136
Figure 4.33: MSE plot of Trial 1 for homogeneous data fusion.....	138
Figure 4.34: MSE plot of Trial 2 for homogeneous data fusion.....	139
Figure 4.35: MSE plot of Trial 3 for homogeneous data fusion.....	139
Figure 4.36: MSE plot of Trial 1 for heterogeneous data fusion.	140
Figure 4.37: MSE plot of Trial 2 for heterogeneous data fusion.	141

LIST OF TABLES

<u>Table 2.1</u> : Previous work in data fusion for NDE	18
<u>Table 4.1</u> : Test specimen suite 1 used for homogeneous sensor data fusion.....	58
<u>Table 4.2</u> : Test specimen suite 2 used for heterogeneous sensor data fusion.....	60
<u>Table 4.3</u> : Trial 1 training and test dataset.....	72
<u>Table 4.4</u> : Trial 2 training and test dataset.....	73
<u>Table 4.4</u> : Trial 3 training and test dataset.....	74
<u>Table 4.6</u> : Trial 1 training and test dataset.....	133
<u>Table 4.7</u> : Trial 2 training and test dataset.....	133

ACKNOWLEDGEMENTS

I would like to thank my family and friends for their support throughout my entire education. I would like to especially thank my parents for their continued guidance, love and, moral support. Everything I am and everything I have accomplished I owe to them, and hope one day I can give back all they have given me. I would also like to thank the Rowan University Electrical and Computer Engineering department for providing me with the opportunity to achieve an excellent undergraduate and graduate degree. Particularly I would like to thank my advisor, Dr. Shreekanth Mandayam for his continual guidance and wisdom throughout this sometimes trying process. His genuine kindness and confidence has truly meant a lot to me. Additionally I would like to thank my committee members, Dr. John Schmalzel, Dr. Robi Polikar, and Dr. John Chen along with my fellow graduate students. Special thanks to Min Kim, Philip Mease, and Mike Possumato for their help in this research. Finally, I would like to thank the United States Department of Energy (DE-FC26-02NT41648) and Exxon Mobil (PERF 95-11) for their support of my graduate studies at Rowan University.

ABSTRACT

The natural gas transmission pipeline network in the United States is a key component of the nation's energy supply infrastructure and extends for over 280,000 miles and has an average age of over 60 years. The integrity of the pipeline is maintained by periodic in-line inspections using magnetic or ultrasonic pigs. Defect characterization algorithms developed using current pigging data are hampered by the fact that single inspection techniques (either magnetic or ultrasonic) do not yield sufficient information for accurately and repeatably characterizing defects. This thesis demonstrates that defect characterization algorithms using multiple inspection techniques can accomplish this task. In particular, it is shown that the varying depth of a surface breaking pipeline defect can be precisely determined using a combination of multiple inspection methods. Also the precise location of such defects can be predicted using dissimilar interrogation methods. A judicious combination of signal and image processing strategies, including geometric transformations, radial basis function approximations and Parzen windows density estimations, have been used to fuse data from both homogeneous and heterogeneous sensors. Application results using data from laboratory experiments demonstrate the consistency and efficacy of the proposed approach.

CHAPTER 1: INTRODUCTION

Nondestructive evaluation (NDE) techniques have long played a fundamental role in assuring the integrity of a variety of large-, medium- and small-scale infrastructure in the United States today. The increase in the number of aging aircraft in the civilian fleet, deteriorating bridges and roadways (especially on the East coast) that are essential for maintaining increased transportation needs, have contributed to a concerted effort by the research and development community to devise more reliable techniques for in-line nondestructive inspection [1, 2]. In New Jersey alone, over 17 percent of roadways and 38 percent of bridges are considered to be structurally deficient [3]. In the prevalent climate of terrorism threats, concerns have been expressed regarding the security and safety of the nation's 104 nuclear power plants and oil and natural gas pipelines – key contributors towards maintaining the nation's energy supply [4, 5].

This thesis addresses techniques for improving the reliability of nondestructive evaluation of the nation's gas transmission pipeline network which extends for over 280,000 miles and has an average age of over 60 years [6, 7]. Gas transmission pipelines (above and under-ground) are primarily inspected for pipe-wall defects using an inspection vehicle called a "pig". The pig is conveyed inside a pipe, either under the pressure of natural gas, or is pulled externally. While magnetic methods of inspection predominate, ultrasonic and visual techniques are also employed. The pig contains an on-board microprocessor with memory modules that can store inspection data. At the conclusion of the pigging process, inspection data is retrieved and analyzed for predicting the condition of the pipe-wall – a process referred to as defect characterization.

Defect characterization mechanisms prevalent in the industry range from calibration based approaches to simple parametric methods to sophisticated techniques using artificial neural networks. A complete signal characterization system provides the following capabilities:

- Signal classification – this isolates defect signatures from signals obtained due to benign changes in geometry.
- Signal location – this is used to provide a precise location of the flaw with respect to specimen geometry
- Flaw profiling – this provides a 3-dimensional geometrical description of the flaw that can be used by subsequent visualization stages.

Defect characterization algorithms developed using current pigging data are hampered by the fact that single inspection techniques (magnetic or ultrasonic) do not yield sufficient information for accurately and repeatably characterization of defects. This thesis demonstrates that defect characterization algorithms using multiple inspection techniques can accomplish this task. In particular, it is shown that the varying depth of a surface breaking pipeline defect can be precisely determined using a combination of multiple inspection methods. Also the precise location of such defects can be predicted using dissimilar interrogation methods.

1.1 Nondestructive Evaluation

Nondestructive testing is defined as those testing methods used to examine or inspect a part or material without impairing its usefulness in the future [8]. Originally, the concept behind NDE inspection was to send one form of energy into the specimen, and measure

the change in the returned single energy. Any abnormal alteration in the original signal would demonstrate characteristics of an anomaly or defect in the specimen. This concept is illustrated in Figure 1.1.

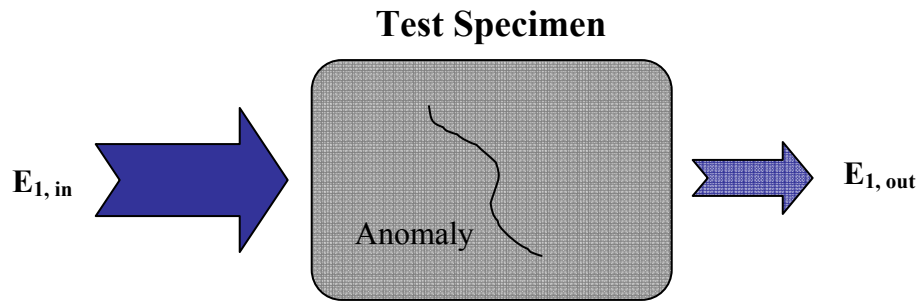


Figure 1.1: Inspection with single NDE technique.

Inspection techniques have long been a necessary element of society since the realization of the unreliability of mankind and their inventions [9]. A wide variety of inspection techniques have been employed, either destructive or nondestructive, in order to prevent and minimize failures in any type of infrastructure. Nondestructive testing (NDT) allows for the inspection of materials for flaws that could potentially cause catastrophic failures such as bridges to collapse, airplanes to crash and the primary focus of this research, pipelines to rupture. Nondestructive testing does exactly as its name states by performing analysis without affecting the future functionality of the object under test. Since inspection can be performed without interfering with the use of the product, nondestructive testing provides a common ground between quality assurance and cost-effectiveness [10].

Nondestructive testing technicians operate under three main assumptions [9]:

1. All materials contain flaws,
2. Flawed materials are not always unfit for use, and

3. The detection of defects increase with size.

The concept of materials being used in operation after flaws have been detected makes the distinction between nondestructive testing and nondestructive evaluation. In this case it is no longer enough to identify the presence of defects as in NDT, but it becomes necessary to characterize the size, shape, and orientation of the defect. NDE methods provide a more quantitative assessment of the flaws providing information that can estimate its severity.

Generally NDE methods are characterized as either active or passive techniques with the distinction of inspecting surface, near surface, or internal defects in materials. Active inspection techniques operate by exposing the material under test to some form of energy. In the presence of a defect or anomaly, the input energy is distorted in some way allowing for the change in energy to be measured. Typical active NDE inspection techniques include the use of magnetics, ultrasound, eddy currents, radiography, and thermal sources. Passive techniques alternatively measure anomalies by monitoring the specimen under its normal operation. The presence of defects becomes apparent with a response or release of energy from the specimen due to its operational load. Common passive NDE methods are acoustic emissions, penetrant testing, leak testing, and visual examination. Examples of surface inspection methods include visual and penetrant testing techniques that are only capable of determining defects located on the surface of the specimen. Other techniques such as eddy current testing and magnetic testing can provide surface and near surface defect characterization but are unable to produce full volumetric estimations of the specimens under test. Volumetric methods are capable of inspection throughout the entire specimen to uncover any internal defects present. This

type of detection is possible with ultrasonic, acoustic emission, and radiographic NDE techniques.

The research presented in this thesis utilizes four of the inspection techniques mentioned above including ultrasonic testing, magnetic flux leakage, thermal imaging, and acoustic emission. Although these four techniques will be described later in extensive detail, a brief summary of all previously mentioned NDE techniques is given below [8, 9, 10, 11].

- **Visual Inspection:** A method of inspection that searches for defects visible with normal eyesight. Tools such as magnifying glasses and mirrors are used to increase the inspector's visibility of the object under inspection. Although a simplistic method of inspection, defects are often located with this procedure as they become larger and more visible. More technology based NDE systems are still needed to locate defects at earlier stages to ensure prevention of critical failures to the infrastructure.
- **Penetrant Testing:** Penetrant testing, used for detection of surface discontinuities, exploits the natural occurrence of fluid accumulation near surface defects. The accumulation is caused by the capillary process at the location of the defect which attracts a higher volume of fluid to the discontinuity relative to the surrounding area. More advanced methods of penetrant testing make use of visible or fluorescent dye solutions. A thick coating of dye is layered onto the specimen. The excess dye is then removed leaving only the dye trapped in surface defects. A developer or ultraviolet

light is then used to draw forth any remaining dye making it easy for the naked eye to view.

- **Leak Detection:** Leak detection methods are commonly used in NDT of gas transmission pipelines. In this type of testing, the specimen is some type of pressure vessel that contains a pressurized substance. Leak detection as an NDT method searches for any presence of exiting material from the pressure vessel using electronic listening devices, monitoring of pressure gauges, and insertion of liquid or gas penetrants that could be easily seen exiting the pressure vessel.
- **Electromagnetic or Eddy Current Testing:** This type of NDE testing requires a ferromagnetic material in which electrical currents can be induced with the presence of a magnetic field. The eddy currents which flow in circular patterns at the surface of the specimen are interrupted at the presence of a discontinuity or changes in the metal surface. The disruption in current flow can be measured with a Hall probe or coil of wire to catch the induced magnetic field.
- **Magnetic Flux Leakage:** Similar to electromagnetic testing, MFL testing requires a ferromagnetic material. In this type of testing, the specimen is magnetized with the presence of large magnet or with an induced magnetic field from lines of current. In the presence of a defect, magnetic flux will leap out of the specimen. A Hall probe can be used to measure the leakage magnetic flux density.

- **Thermal Imaging:** Thermal imaging relies on the transfer of heat to determine the presence of defects. Heat sources such as high intensity lamps are directed at the surface of the specimen. The heat transfer throughout the specimen varies in the location of a defect. The change in energy throughout the specimen can be viewed by taking multiple frames with an infrared camera.
- **Acoustic Emissions:** Acoustic emission, a passive NDE technique, listens for high frequency noise created by cracking, dislocations, and disbonding. An effective technique for metals, concrete, and composites, acoustic emission waves are generated by local stress redistributions as a specimen yields while under use. A stress stimulus that simulates normal use or overloading is needed to induce the emission of acoustic waves. Piezoelectric transducers are used to constantly monitor the specimen under test.
- **Ultrasonic testing:** Ultrasound is one of the most effective active NDE methods providing defect information throughout the entire thickness of the specimen. Ultrasound searches for defects by bombarding the specimen with high frequency sound waves. As the sound waves propagate through the material, they scatter and reflect at the presence of any discontinuity. The change in the sound waves after propagation through the specimen is measured to indicate the presence of any defects.
- **Radiography:** Radiography is considered to be the most accurate and reliable testing procedure for NDE engineers, providing exceptional results

when finding internal defects. Radiographic inspection employs the propagation of energy sources such as X-ray and penetrating gamma radiation through its specimens. The energy sources are passed through the object under inspection, allowing analysis of the energy pattern exiting to make a determination of the specimen condition. The exiting radiation is directed onto a film or other imaging device to depict the dimensional features of the object similar to that of a medical x-ray.

Unfortunately no single NDE method is capable of inspecting all types of infrastructure. Therefore to properly extract the necessary defect characterization information, multiple NDE techniques must be employed to the same specimen. This is largely due to the wide variety of materials used in past and present infrastructures which consist of composites with different types of metals and dielectrics present. This presents the need for a combination of NDE methods working in conjunction with each other to produce additional information about the object under inspection. This technique is illustrated in Figure 1.2 where three different NDE modalities are entered into a test specimen. Each NDE method provides different information about the test specimen allowing analysis of this data to characterize any anomalies present.

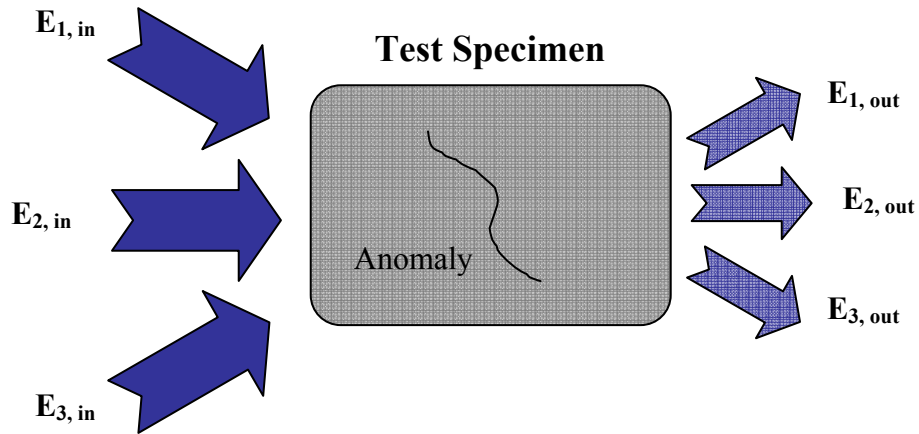


Figure 1.2: Multi-sensor NDE inspection.

With the addition of multi-sensor inspection comes the need for multi-sensor data fusion. The resulting NDE signature after the data fusion process will contain additional information about the defect that was not available from any one of the original NDE signatures alone [12].

Although multi-sensor interrogation provides added information about the defect, the data fusion process of combining the various NDE signatures produces an array of complications. High complexity can arise when the data fusion process is being performed with heterogeneous data sources where the dimensionality of the data may vary between each NDE signature. Heterogeneous multi-sensor data fusion is the combination of dissimilar NDE inspection signatures that vary in dimensionality of data and information available for combination. This means NDE signals found in practice are a compilation of 1-D time-domain signals, 2-D spatial domain images, singular events describing time-history, anecdotal evidence and a priori knowledge [13]. Many NDE inspection modalities such as ultrasound, MFL, X-ray, and eddy-current testing provide two dimensional analysis of the specimen providing information of defect geometry as

well as defect location. The homogeneous data fusion combination of these sources is less complicated since the same type of information is present in each source. Other NDE inspection methods such as acoustic emission do not provide the specific geometrical or location information of the defect that is provided by the previously mentioned sources. Therefore when combining heterogeneous NDE signatures it becomes necessary to ensure the combination of information pertaining to the same characteristics of the defect. Data fusion between dissimilar testing methods such as these can provide valuable information providing the necessity for heterogeneous data fusion algorithms.

Another common problem is difficulty in registering the data so the different NDE signatures correspond to the exact same section of the specimen under test. It also becomes necessary to optimize the data fusion combination technique in order to increase the amount of relevant information pertaining to the defect characterization. It is the goal of this thesis to address these concerns with the use of experimental NDE data.

1.2 Multi-sensor Data Fusion

A significant amount of resources have been designated to the advancement of multi-sensor data fusion in recent years. The objective of data fusion techniques is to combine the related information found in multiple sensors to develop more specific conclusions than could be determined with a single sensor or source [14]. A wide variety of both military and non-military applications have been researched including earth resource monitoring, weather forecasting, vehicle traffic control, and military target classification and tracking [15]. The concept of multi-sensor data fusion has been present throughout nature, but only recently has become a practical technique with the advancement of

sensors and computer processing capabilities. Humans and animals regularly utilize a form of multi-sensor data fusion when combining their five senses to make determinations about their surrounding environment. For example, when an animal is determining whether something is edible it does not only rely on its sense of sight [14]. It is also necessary for the animal to smell, taste and touch the object before determining the safety of the situation. It is this type of combination of information that engineers of multi-sensor data fusion techniques hope to replicate as their methods advance.

The data fusion model was first introduced by the U.S. Joint Directors of Laboratories (JDL) Data Fusion Group in 1985. The first attempts at data fusion model were very specific and restricted to only military applications. In order to apply the data fusion model to other non-military processes, the model was redesigned in 1998. The updated data fusion model definition reads as follows: “Data fusion is the process of combining data or information to estimate or predict entity states”. The object of the data fusion process can either be to predict entities of physical states (such as: identity, attributes, activity, location, etc.) or that of perceptual states. Perceptual state data fusion processes predict the actions of individuals or groups of individuals [14]. The data fusion model also accounts the interaction between physical and perceptual states.

There are many inherent advantages to combining information from multiple sensors. First and most obvious, when combining the output of multiple identical sensors, a greatly improved estimate of the objects characterization can be obtained. This provides a statistical advantage for each addition sensor N introduced to the network improving the estimate by a factor proportional to $N^{1/2}$ [14]. Second, the observation process can be improved by strategic placement and movement of multiple sensors.

Multiple sensors with angular direction measurement capability can triangulate the position of an object. A known movement of one sensor relative to another stationary sensor can be used to determine the position and velocity of an object in comparison to the sensors. Most importantly, additional information about an object can be ascertained with the use of multiple varying sensors. Each sensor measures a different aspect about the objects functionality and characterization that the other sensor can not produce. The combination of this data provides a more accurate and informed estimation of the object that could not have been determined without the use of multiple sensors.

There is substantial potential in applying data fusion techniques to the area of non-destructive evaluation. It is the intention of NDE to use data fusion methods to combine data from non-commensurate NDE signals to gather additional information concerning the specimen under test. The addition of multiple independent sensors will provide a more detailed characterization of any anomalies present in the specimen. The NDE signatures to be combined correspond to the same test specimen and location scanned. The data fusion process is performed on the NDE signatures to produce the fused data which contains a more accurate and detailed description of the specimen. Figure 1.3 illustrates the data fusion process. The NDE inspection signals are considered to be any of the NDE techniques listed in section 1.1 of this chapter.

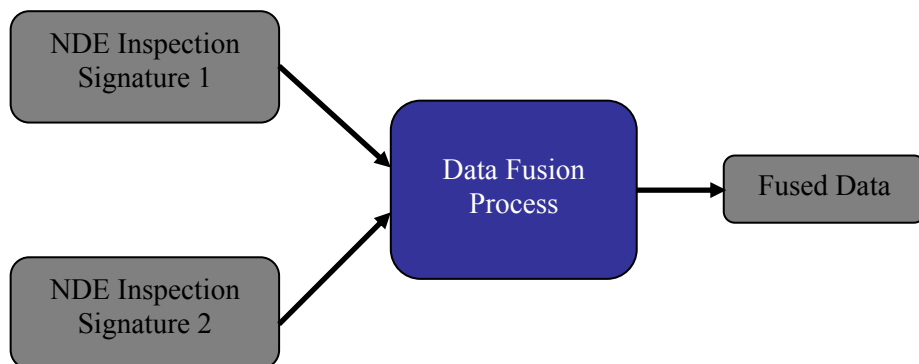


Figure 1.3: Block diagram of data fusion process.

The NDE signatures are comprised of different information corresponding to the test specimen. In this particular case, redundant and complementary information between the two NDE signals is the focus of this research. The redundant data feature represents the information that is present in both NDE signatures. If a defect is present in a test specimen and both NDE signatures are able to locate and characterize the size and shape of that defect, those features would be redundant between the two NDE signatures. For example, given three measurable parameters x , y , and z , where NDE method 1 is able to determine parameters x and y only while NDE method 2 is able to determine parameters y and z only. In this instance, the resulting redundant data would be parameter y . The addition of redundant information as a features helps to improve the confidence in the measurement taken since two methods have now verified that parameter.

Complementary information is the information present in the NDE signals that is unique to each signal when testing the same object. An example of this would be an NDE method that is capable of determining the full geometry of a defect including the length, width, and depth of the anomaly, where as the second NDE method can only ascertain the two dimensional profile limited to length and width of the defect. In this case, the unique or complementary data is the depth of the anomaly. Again focusing on parameters x , y , and z , the complementary information in these signals would be parameter x and z , were parameter x being determined by NDE source 1 and parameter z characterized by NDE source 2. Complementary information is an important feature to focus on because it improves the accuracy of the testing results. Each NDE method provides a different element to the fused data providing a total characterization of the

defect present in the specimen. Figure 1.4 provides a visual representation of the redundant and complementary data extraction process.

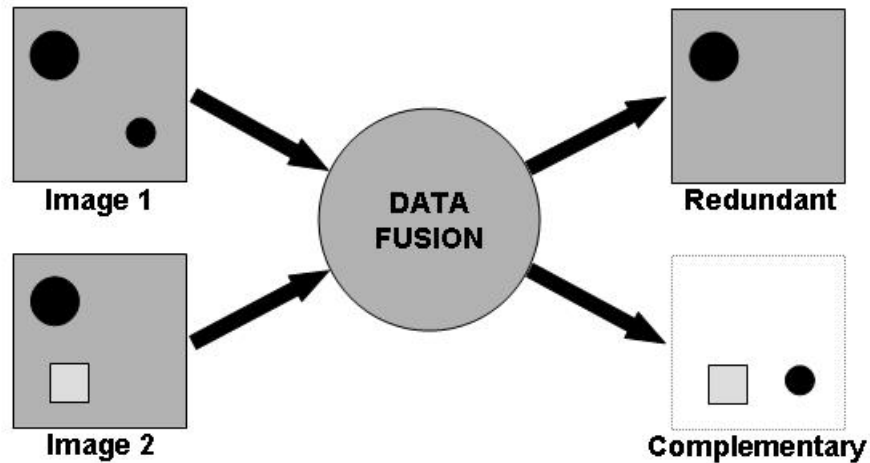


Figure 1.4: Redundant and complementary information extraction from two NDE sources [13].

1.3 Objectives of Thesis

The objectives of this thesis are:

1. Design and development of a geometric transformation based data fusion algorithm for the prediction of specific information fusion measures – redundancy and complementarity;
2. Application of the data fusion algorithm to accurately and confidently predict the varying depth profile of surface-breaking pipe wall defects in a gas transmission pipeline;
3. Demonstration of the algorithm's ability to fuse data from multiple homogeneous and heterogeneous sensors;
4. Design and development of experimental validation test platforms and protocols for measuring the efficacy of the data fusion techniques.

1.4 Expected Contributions

The overall objective of this research work is to design data fusion algorithms that can synergistically combine defect related information from multiple heterogeneous sensors used in gas pipeline inspection for reliably and accurately predicting the condition of the pipe-wall. The multi-sensor data fusion algorithms are exercised using the following set of NDE techniques – magnetic flux leakage, ultrasonic testing, and thermal imaging provide homogeneous data that are gray-level intensity images whose pixels are co-located with the defect profile. Additionally, acoustic emission testing provides “hit” information that can be used to predict defect location, but does not provide a defect profile. The multi-sensor dataset is experimentally obtained in the laboratory; test-specimens representative of anomalies found in gas pipelines have been fabricated.

1.5 Scope and Organization of Thesis

This thesis is organized as follows. Chapter 1 provides an introduction to NDE techniques and the role of multi-sensor data fusion to characterize natural gas transmission pipeline anomalies. Chapter 2 describes the previous work performed in this area of research, provides a detailed description of NDE methods used in this research, and the necessary background information on geometrical transformations and density estimation techniques that form part of the proposed approach. Chapter 3 describes the proposed approach for performing multi-sensor data fusion using geometric transformations Parzen Windows for combining homogeneous and heterogeneous data sets. Chapter 4 discusses the data collection experiments and implementation of the proposed data fusion methods. Results presenting the effectiveness of these techniques

are also provided in this section. Chapter 5 provides conclusions drawn from this research work, as well as the recommendations for further research in the area.

CHAPTER 2: BACKGROUND

This chapter provides a summary of previous work performed in the area of data fusion, particularly with NDE applications. A detailed explanation of the NDE methods used for multi-sensor data collection will also be given. Finally, the theoretical background information is provided on geometric transformations and Parzen windows, which are used as methods for performing multi-sensor data fusion.

2.1 Previous Work in Data Fusion for NDE

In the past ten years, the use of data fusion for NDE purposes has steadily increased. Table 2.1 outlines some of the prominent research in this area, including fusing data from a variety of sources including: ultrasound, eddy currents, X-ray, MFL, and thermal images. This research includes the use of fusion methods such as Dempster-Shafer and Bayesian analysis, as well as the use of artificial neural networks (ANNs) for data fusion purposes.

Table 2.1: Previous work in data fusion for NDE.

Authors and Paper Title	Area of Research
M.Mina, J. Yim, S. Udpa, L. Udpa, et. al., "Two-dimensional multi-frequency eddy current data fusion," 1996 [16]	Data fusion to combine multi-frequency eddy current images of same specimen
X. E. Gros, J. Bousigue and K. Takahashi, "NDT data fusion at pixel level," 1999 [17]	Data fusion of eddy current and infrared thermographic images using weighted averaging, Bayesian analysis, and Dempster Shafer among other techniques
D. Horn and W. R. Mayo, "NDE reliability gains from combining eddy-current and ultrasonic testing," 2000 [18]	Bayesian analysis and Dempster Shafer to combine ultrasound and eddy current images of Zr-Nb pressure tube specimens with manufactured defects
S. Gautier, B. Lavayssiere, E. Fleuet and J. Idier, "Using complementary types of data for 3D flaw imaging," 1998 [19]	Used Dempster Shafer and Bayesian inference to fuse X-ray and ultrasound images to reveal complementarities
J. Yim, "Image Fusion Using Multi-resolution decomposition and LMMSE filter," 1995 [20]	Proved ANN are viable method for data fusion. Used MLP and RBF to combine eddy current and ultrasound images

P.J. Kulick, "Multi-sensor data fusion using geometric transformations for the nondestructive evaluation of gas transmission pipelines," 2003 [13]	Extraction of redundant and complementary information using RBF neural networks from ultrasound, MFL, and thermal imaging data.
--	---

The authors of [16] performed a 6, 7, 8, and 12-block Discrete Cosine Transform (DCT) for the fusion of multi-frequency eddy current images in the spectral domain. The images had undergone some form of linear degradation. It was the goal of the research to reconstruct the true image by using two or more degraded images obtained at various excitation frequencies. The fusion method was based on the ratio of the spectrum of images as well as the signal to noise ratio of each image. This method was used as a measure of quality for each image to develop a weighting function for the image fusion. The image with a higher SNR was ultimately weighted more heavily in the final image fusion process. The reconstructed image was then synthesized from the fused spectrum. A series of eddy current images ranging in frequency from 50 kHz to 250 kHz were taken from the same test specimen to be combined. The test specimen consisted of a machined aluminum block with two surface and two subsurface defects. The results showed that the reconstruction worked best when used with the 7 and 8 block DCT.

An array of pixel level data fusion techniques were used by the authors of [17] in hopes of combining eddy current and infrared thermographic images. A carbon fiber reinforced plastic (CFRP) panel that had been subjected to impact damage by a low energy source, was interrogated using both NDE modalities. C-scan ultrasound images were also collected of the damaged area to generate a point of reference to compare the data fusion methods. The data fusion methods employed included: maximum amplitude, integration, averaging, weighted averaging, Bayesian analysis and Dempster-Shafer theory. The maximum amplitude data fusion method performed pixel level fusion by

choosing the pixel with the higher amplitude from the two initial images. The integration data fusion procedure performed a logical AND function on each of the original pixels. The averaging technique simply averaged the pixel values of the original images. The weighted average method assigned rankings to different NDE methods depending on their accuracy and reliability. This allowed for certain images to have a greater effect in the data fusion process when the pixels are averaged. Finally the Bayesian analysis and Dempster-Shafer methods utilized probability and belief combinations to perform data fusion. An area of impact analysis was performed on both ultrasound images and fused data images. It was found that the maximum amplitude and Dempster-Shafer methods produced the results nearest to the ultrasound inspection reference.

The author of [18] performed data fusion on a database of 108 artificial flaws with test specimens made of Zr-Nb. The specimens, a mineral metal bond, were pressure-tube billets that contained either notched or drilled defects. Ultrasound and eddy current images of the specimens were combined using a series of elementary and more complex data fusion methods to provide classification between the notched defect, drilled defect, and no defect. The data fusion techniques ranging from simplistic to complex were performed using logical OR, averaging and weighted averaging, classical inference, Bayesian analysis and Dempster-Shafer theory. The data fusion process using the OR function provides a zeroth-order combination that does not consider defect flaw size into the decision but rather only provides a yes/no decision. This process rejects any sample from which one or more individual measurements signify rejection. The averaging process provides a first order combination where the signal amplitudes being averaged relate to the defect's size. Weighted averaging provides extra dimensionality by

including a priori knowledge into the decision. The classic inference, Bayesian inference, and Dempster-Shafer method provide decision level identity fusion where each decision is either accepted or rejected based on a joint probability distribution. Different probability density functions and relative operating characteristics were used to determine how accurately the data fusion methods classified the defects. The author's results showed a significant improvement in classification when using the combined ultrasound and eddy current data with the OR logic combination compared to either data set by itself. Additional improvement in classification was obtained by using the averaging and weighted averaging data fusion methods. The classic inference, Bayesian inference, and Dempster-Shafer method also provide very good classification results but are only marginally better than the averaging combination results.

In [19], a dataset of X-ray and ultrasound images were collected from a steel test specimen with a previously known discontinuity. Bayesian inference and Dempster-Shafer theories were used for three different processing architectures: decentralized, cascade, and centralized. The decentralized architecture performs fusion on the two datasets after preprocessing has been applied to each dataset separately. The cascade architecture processes the first dataset independently then reprocesses the result with the second dataset together before performing the data fusion. In the centralized architecture the datasets are fused directly without any preprocessing. The inference theory is independent of which preprocessing architecture is chosen. The difference between the architectures is noticed in the number of preprocessing steps taken before the fusion process. The data collection process was focused on obtaining the complementary features between the two inspection modalities. Optimal results were achieved using the

centralized architecture method, despite its higher complexity and longer run-time. This is attributed to the additional preprocessing in other architectures causing a loss of information before the fusion process.

The authors of [20] experiment with using artificial neural networks to perform data fusion. Multi-layer perceptrons (MLPs) and radial basis functions (RBFs) were used in the combination of ultrasound and eddy current images, and additionally the fusion of multi-frequency eddy current images. The images were fused using pixel level logic operations AND and OR. The AND (maximum) operator brings forth the common features between the images, where as the OR (minimum) operator determines the complementary information in the images. The tests were performed on two different aluminum specimens of 6 mm thickness with varying defects. The first specimen contained a 1/32 inch diameter through hole that was then covered with a thin layer of copper foil to conceal the defect. The second specimen also contained a hole of 1/32 inch diameter but that only penetrated the surface by 5.5 mm. Initial results were obtained for the combination of ultrasound and eddy current images performed on the first specimen, using both the MLP and RBF networks with two hidden layer nodes. In this case the results yielded very poor and unclear images. Additional results were also achieved using the RBF network with five hidden layer nodes with center identification from a K-means algorithm. These results yielded more accurately fused images with a higher SNR and recognizable defects. The second specimen was used in the combination of the multi-frequency eddy current images. The combination of 6 kHz and 20 kHz eddy current images using the five hidden layer RBF network with the K-means algorithm was

performed. These combinations yielded fused images with clearly visible defects present.

Portions of this current research are a continuation on the work performed by Philip J. Kulick [13]. In his research, geometric transformations and RBF neural networks were used to extract the redundant and complementary information found in different NDE testing modalities. A test specimen suite with various simulated pipeline anomalies including pitting, stress corrosion cracking, dents and welds was created. The test specimens were subjected to ultrasound, MFL, and thermal imaging methods to create a rich database. The results were promising, providing the extraction of redundant and complementary information of binary NDE images. This current research extends this work by incorporating multilevel signatures into the algorithm and also integrating NDE data from heterogeneous sources.

2.2 NDE Inspection Techniques

The following NDE inspection techniques were used in this research to obtain multi-sensor data. The fundamental principles of each technique will be explained in detail in this section, including their use and application as nondestructive evaluation tools.

2.2.1 Ultrasonic Testing

Ultrasound was first used as an evaluation technique in the early 1900s and has since advanced to be the benchmark technique when performing nondestructive evaluation. Ultrasonic inspection uses high frequency sound energy, typically between 1 and 25 MHz, for inspection and examination of materials. Ultrasonic testing is well suited to perform flaw detection as well as other tasks such as dimensional measurements and

material characterization. As an NDE method, ultrasound is valuable due to its capability in detecting both surface and subsurface discontinuities all while providing an extremely accurate determination of defect geometry and location.

A typical ultrasonic inspection system consists of a pulser/receiver, transducer, and display components. The pulser/receiver generates high voltage electrical pulses that drive the transducer. The transducer, made of a piezoelectric material, has the ability to convert the electrical energy into a mechanical vibration. When the intensity of the vibration is large enough, high frequency ultrasonic energy is created. The generated sound energy has the ability to propagate through materials as waves. At the presence of a defect or discontinuity, the sound waves will reflect back or scatter in different directions providing a marker for flaws in material.

Currently there are both transmission and reflection techniques when performing ultrasound testing. These techniques are known as through transmission and pulse echo respectively. During a through transmission test, the ultrasonic energy is directed into the test object with a transmitter, and the energy exiting the opposite side of the test specimen is measured with a receiver. In this scenario the presence of a defect would be detected by the decrease of energy at the receiver transducer. The through transmission method is presented pictorially in Figure 2.1.

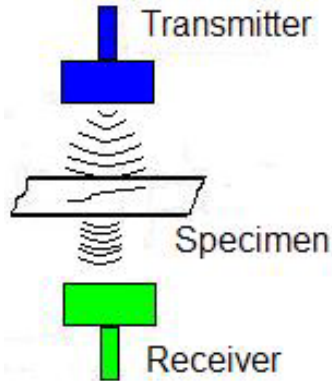


Figure 2.1: Through transmission ultrasonic testing.

Unlike through transmission, the pulse echo method uses only one transducer for both transmission and reception. The ultrasonic energy is directed into the test specimen and the energy reflected back from any discontinuities present in the object is measured. The pulse echo ultrasonic technique can be seen in Figure 2.2.

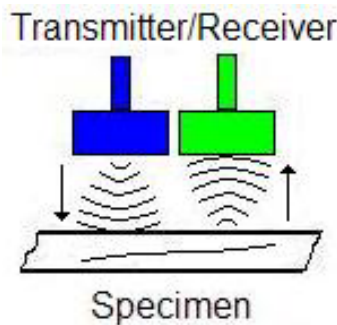


Figure 2.2: Pulse echo ultrasonic testing.

Typically, ultrasonic testing generates three forms in which to measure the status of the specimen. These forms of measurements are referred to as the A-scan, B-scan, and C-scan data, each providing different information about the specimen. The A-scan depicts the voltage vs. time representation of the ultrasound data. This depiction provides size and depth information that can be determined through a combination of amplitude and phase shift information. The B-scan provides a cross sectional view of the specimen by plotting the x and y location of the transducer verses the ultrasonic values. C-scan

similar to B-scan plots a top down view of the discontinuity area providing the defect location and size determined from variation in signal amplitude as a function of position.

Figure 2.3 shows the variation in B-scan, and C-scan data.

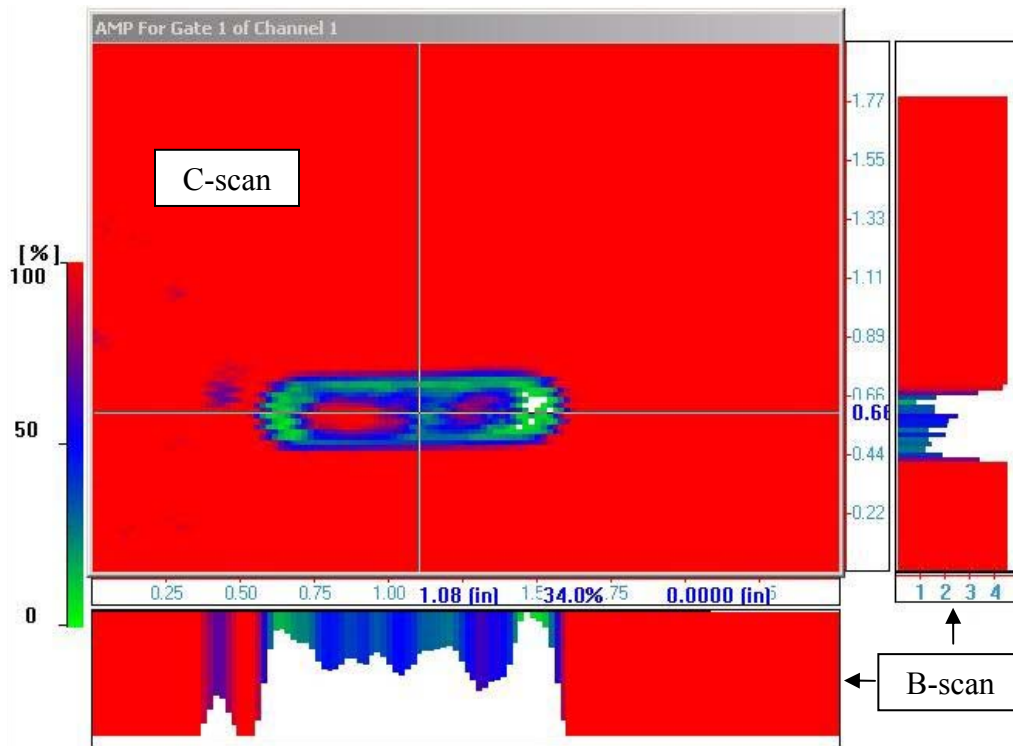


Figure 2.3: B-scan, and C-scan ultrasound data.

There are three main parameters of interest when determining the presence of discontinuities in a specimen. These parameters include back surface reflection amplitude, amplitude of extraneous reflections, and Time of Flight (TOF) measurements, which can all be determined by examining the A-scan of the ultrasound test. These features are illustrated on a sample A-scan in Figure 2.4.

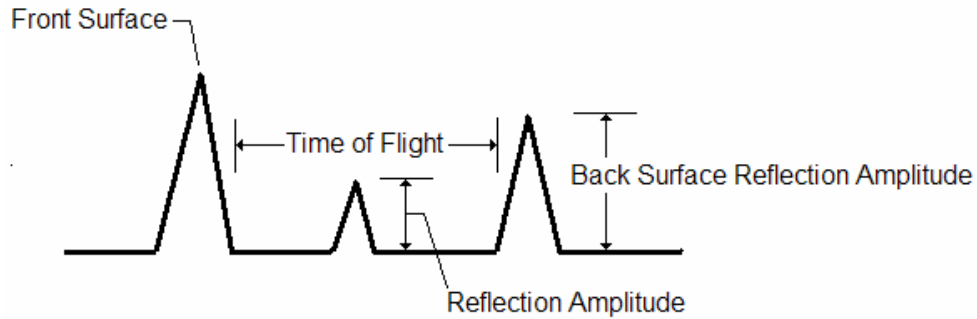


Figure 2.4: Defect detection parameters [21].

The back surface reflection amplitude provides a measure of attenuation by measuring the difference between the amplitude of the front surface reflection to the back surface reflection. A decrease or absence of a back surface reflection provides a quick indication that the transmitted sound was absorbed, refracted, or reflected by a defect. The defect can potentially be described from comparison of back surface reflection amplitude over no defect to defect area. The extraneous reflection amplitude provides detection of discontinuities by measuring reflections appearing between the front and back surface waves. The reflection pattern can be used to indicate the discontinuity type while the reflection amplitude provides a measure of the discontinuities size. Amplitude gating is set to determine the area of interest and threshold setting for waves that become present. Finally, the time of flight measurement determines the time between the front surface reflector to the next significant reflection in the signal. When the next significant reflection is the back surface reflection, this is an indication of no discontinuities present. The addition of a peak before the back wall reflection indicates the presence of a defect that is reflecting the original signal. Determining the time difference between the back wall reflection and defect reflection can provide an estimate of how deep the

discontinuity lies within the specimen. Timing gates are used to define the boundaries of the time domain.

Ultrasonic testing is a viable NDE method because there is minimal loss of ultrasonic energy in homogeneous materials. The only energy loss is due to the interception or reflection of the ultrasonic beam by a discontinuity in the specimen. Despite ultrasounds exceptional ability to locate and characterize defects, it does possess some minor limitations. In order to perform ultrasonic testing, a coupling or medium is needed to transmit the sound energy into the specimen. Typically immersion tanks are used to submerge the specimen to use water as the medium, but this can become increasingly difficult as the specimen under test grows in size. Another drawback to ultrasound is that heterogeneous or composite materials are difficult to inspect. This is due to the same reason that makes ultrasound a viable method for testing homogeneous materials, in that ultrasonic testing strength lies in determining changes throughout the material. In a composite structure that is composed of varying types of materials, ultrasound would misjudge the changing material structure as a defect, when no defect is actually present.

2.2.2 Magnetic Flux Leakage

Magnetic flux leakage methods have been used in practice for well over one hundred years dating back to 1868. In the early 1900s magnetic particle testing was discovered when metal shavings were held in place by changes in the magnetic flux near the surface of a defect. MFL testing was soon made possible by the addition of magnetic field sensors in the 1930s [22]. The sensors allowed for measurement of the magnetic field around the defect area and provided a more quantitative measurement than could be

gained by the scattering of magnetic particles. In 1965 the first inline inspection tool (known as the “pig”) for magnetic testing of pipelines was developed by a company called Tuboscope. Figure 2.5 shows a more modern version of the “pig” equipped with rings of magnets and hall sensors to perform inline inspection of pipelines. Today, MFL is the oldest and most commonly used inline inspection method for finding metal loss in natural gas transmission pipelines [22]. MFL is well equipped to detect metal loss defects due to corrosion and gouging, and additionally can occasionally provide reliable results for other types of metallurgical and geometric conditions such as hard spots, inclusions, laminations, cracks, dents and buckles.



Figure 2.5: MFL inline inspection tool: the “Pig”.

The actual process of performing MFL testing consists of magnetizing a specimen of ferromagnetic material and scanning the surface with a magnetic flux sensitive sensor for changing magnetic fields [9]. The specimen under test is normally magnetized by placing it in close proximity to a permanent magnet or to a conductor with a high amount of current passing through it. In some cases the magnetic field is created by passing current through the specimen directly. Once a high magnetic flux density level is created the changing flux can be measured with a variety of sensors including coils, C-core yokes, and solid state magnetic sensors [9].

MFL testing is possible because when a magnetic field comes in contact with a defect the natural flux lines are diverted or forced to leak out of the pipeline. Figure 2.6 (a) shows a magnetic field in contact with an intact pipe wall. The figure shows that most of the flux lines will naturally flow through the pipe wall which acts as a conductor between the north and south poles of the magnet. When metal loss is present in the pipeline, this scenario is altered and can be viewed in Figure 2.6 (b). The decrease in the thickness of the pipe wall causes the flux leakage to occur at the metal loss region. The total flux that can be carried at the metal loss region is less than that of the full pipe wall region forcing the flux lines to find an alternate route. The magnetic flux density in the metal loss region will be higher than that of the other regions, allowing it to be measured with an inline inspection tool.

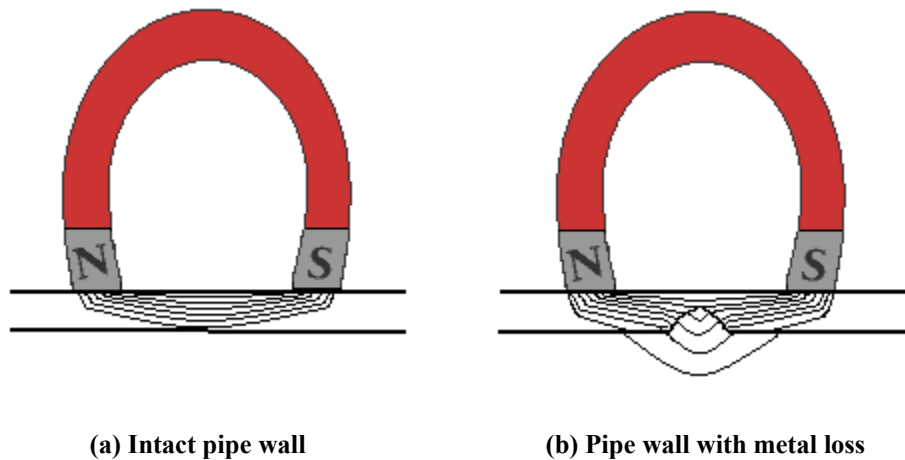


Figure 2.6: Magnetic flux lines through pipe wall [22].

The magnetic flux leakage that is measured corresponds to the geometry and magnetic properties of the anomaly present allowing the defect to be characterized by the measurement. In some occasions the shape of the leakage field can resemble the shape of the defect, but this is usually not the case. The leakage field measured is also dependent on the defects location being closer to the inside or outside of the pipe wall.

2.2.3 Acoustic Emission

The acoustic emission technique is a relatively new NDE method with the ability to monitor the behavior of materials while under stress and strain. Acoustic emissions can be characterized as transient elastic waves generated by the spontaneous release of energy within a material while undergoing deformation [23]. A passive method of testing, acoustic emission was originally developed for the inspection of pressure vessels. It was noticed that growing cracks would emit high frequency noise that could be measured. In addition to cracking, acoustic waves are also generated from dislocations, fiber breaks, and disbonding making AE an ideal method for inspection of metal, concrete, composites, and leak detection. Typically waves are generated due to local stress redistributions associated with the aforementioned defects that appear on both a microscopic and macroscopic level. In order to achieve this sound wave generation a stress or stimulus must be applied to the specimen. Figure 2.7 demonstrates the acoustic emission process.

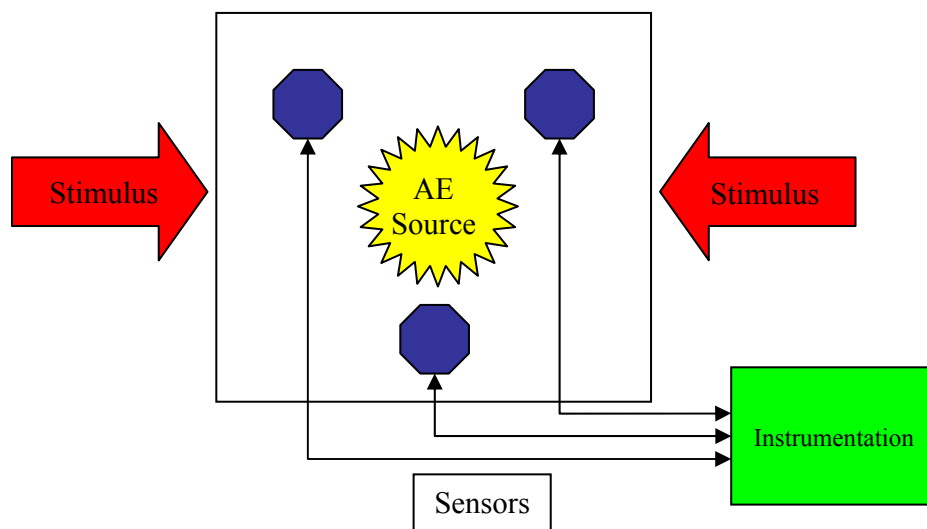


Figure 2.7: Acoustic emission process [23].

Acoustic emission systems consist of piezoelectric transducers that convert the mechanical energy of an elastic waveform to an electrical signal that can be amplified and filtered to produce meaningful results. Current AE sensors have the capability of detecting frequency ranges as low as 10 kHz and up to 2000 kHz. This translates to the detection of a microstructure movement as small as 10^{-12} inches, providing enough sensitivity to detect the breaking of a single grain of metal, a single fiber of a composite, or a single bubble from a pinhole leak [23]. With devices this sensitive, AE testing can provide an early warning system about the structural integrity of the specimen under test.

When performing an acoustic emission test, software will display points corresponding to the (x, y) position of any AE event. Multiple sensors arranged in arrays on the surface of the specimen listen for any acoustic activity. When an AE event occurs the time lapse between the sound wave arriving at each sensor is recorded and allows for the position of AE source to be triangulated. Multiple AE events in the same position indicate the possible presence of a defect at that location. Acoustic emission also has a passive nature that makes it advantageous since the only energy needed to perform a test is exhibited from the specimen while under its normal use. This allows for specimens to be monitored continuously over a long period of time being much more cost effective than other active NDE methods.

2.2.4 Thermal Imaging

Thermal imaging is a relatively new NDE technique for the inspection of natural gas transmission pipelines. Like most other NDE methods, thermal imaging relies on the transfer of energy to characterize defects present in specimens. Heat energy in the form of high intensity lamps is directed into the specimen under test. The transfer of heat

through the specimen varies in the presence of an anomaly providing a difference in temperature from defect to non-defect areas of the specimen. A highly sensitive infrared imaging device can then be used to monitor the temperature variations over time as the specimen heats up and returns to its normal temperature. The thermal imaging process is depicted in Figure 2.8. Although at this point thermal imaging has not been proven as a viable method for pipeline inspection, recent research anticipates incorporation of thermal imaging in conjunction with an inline MFL inspection process, using the residual heat generated by the MFL testing as a heat source.

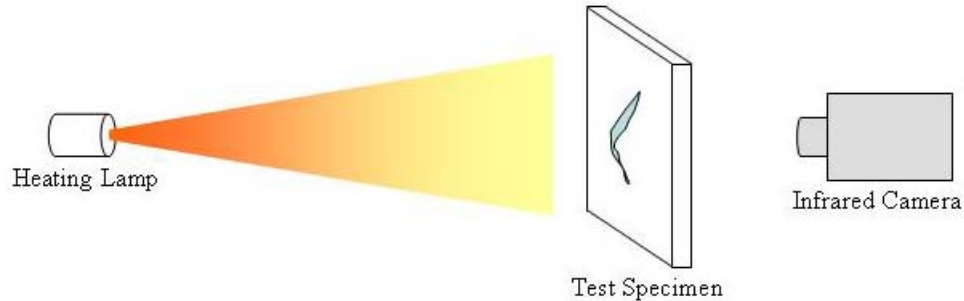


Figure 2.8: Thermal imaging technique.

2.3 Geometric Transformations

Geometric transformations are a widely used method in digital image processing. Geometric transformations are often used to perform image restoration, the process of objectively restoring an image by modeling the degradation phenomenon and inverting the process to reconstruct the original image. Unlike most common image restoration techniques, geometric transformations modify the spatial relationship between the image pixels, rather than the spectral or frequency relationship. Geometric transformations are often referred to “rubber sheet transformations. This is because they can be interpreted as printing an image on a sheet of rubber, and then stretching the rubber sheet to some

predefined set of parameters. In other words, the goal of a geometric transformation is to map a pixel (x,y) to a new position (x',y') by using a set of predetermined transformation equations. Figure 2.9 helps to illustrate this principle. The necessary transformation equations can often be determined from the known original and transformed/distorted images.

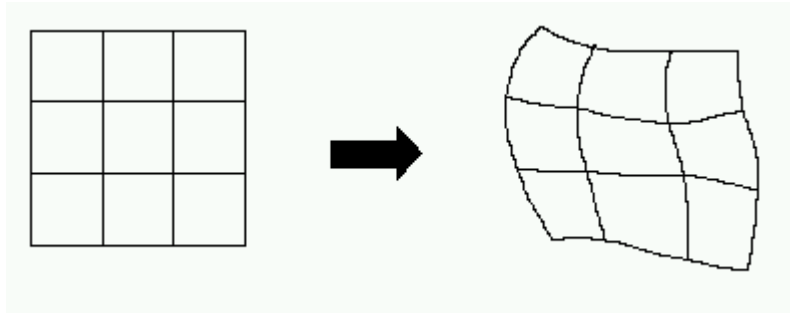


Figure 2.9: Geometric transformation pixel mapping [24].

Geometric transformations allow for the reduction or elimination of geometric distortion that occurs during the image capture process. Geometric transformations are often used in computer graphics and image analysis. They are particularly useful for matching different images of the same object. An example of such an application would be to match remotely sensed images taken over the length of a year. This becomes a challenge because the more recent images were most likely not taken from the exact same position. In order to analyze the images it is first necessary to determine the geometric transformation that occurred by subtracting one image from the other to characterize the geometric calibration that is needed. Another application that geometric transformations are often used for is correcting document skew in document image processing applications. This is when an image with a set orientation (a printed page) is scanned or copied in a different orientation. The orientation change may be insignificant

at first, but if the same skew is exploited in later reproductions of the image then the effects may become more severe. This becomes a problem when optical character recognition systems are set in place to characterize these images.

There are four main types of geometric transformations: translation, rotation, sizing, and shear. These geometric transformations are illustrated in Figure 2.10. Translation is simply applying an offset to the entire image in a 2-D plane. Rotation is the result of rotating or applying rotary movement to the original image. Sizing is achieved by scaling the original image, and shear refers to a skew in some manor by changing the relationship between the pixels in the image.

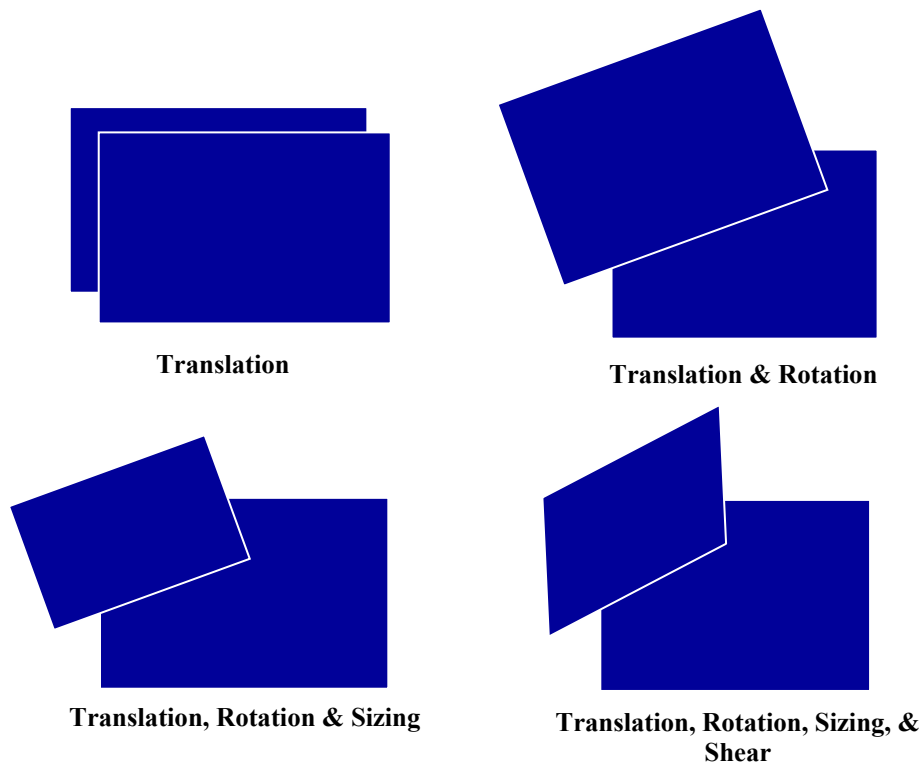


Figure 2.10: Geometric transformation types.

From a digital image processing standpoint, there are two basic operations involved in geometric transformations: spatial transformations and gray-level

interpolation. Spatial transformation is the rearrangement of pixels on the image plane by using the determined pixel coordinate transform. This process usually yields non-integer values for the output points because the transforms mapped positions do not normally match up with the digital grid. For this reason, gray level interpolation is necessary, and is defined as the assignment of integer gray level values to the pixels in the spatially transformed image. Both of these methods will be discussed in detail in following sections of this chapter.

2.3.1 Spatial Transformations

As previously stated the spatial transformation process maps the coordinates of the input image pixel to the corresponding point in the output image. In actuality, as seen in Figure 2.11, a pixel from the original image f with point (x,y) experiences a geometric distortion process and produces image g with point (x',y') .

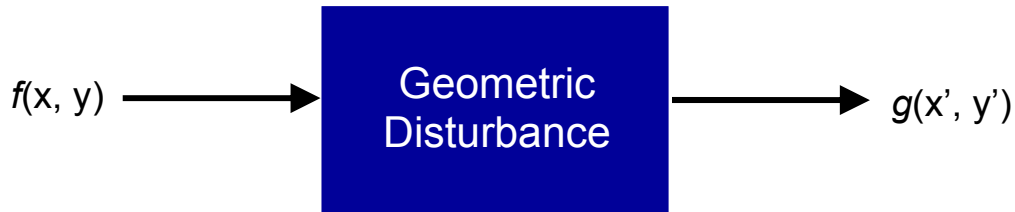


Figure 2.11: Spatial transformation on pixel level.

The spatial transform is expressed by the following equations, where $r(x,y)$ and $s(x,y)$ represent the spatial transformations that produces the output image $g(x',y')$.

$$x' = r(x,y) \tag{2.1}$$

$$y' = s(x,y) \tag{2.2}$$

In the above equations, x' is denoted as the spatial transformation in the x direction, while y' is the spatial transformation in the y direction. An example of a simplistic spatial transformation would be if $r(x,y) = x/2$ and $s(x,y) = y/2$. The distortion applied

would simply shrink the original image f to $\frac{1}{2}$ its original size in both the x and y directions.

If both distortion parameters $r(x,y)$ and $s(x,y)$ can be fully described analytically, then it is theoretically possible to recover the original image f by applying the inverse spatial transformation. Unfortunately, in practice, it is considered impossible to generate a single set of analytical equations to describe $r(x,y)$ and $s(x,y)$ over the entire image plane. To overcome this problem, a method must be devised to generate spatial relationships between the image pixels. This is often done by using “tiepoints” which are a subset of pixels whose (x,y) locations are precisely known in the input (distorted image) and output (corrected image). Tiepoints are represented as the vertices of quadrilateral regions defined in the image. This is further represented in Figure 2.12.

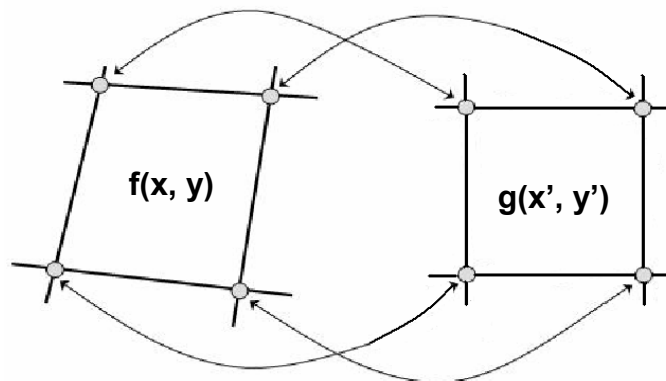


Figure 2.12: Corresponding tie-points in quadrilateral regions of input and output images [25].

Tie-points can be generated by a number of different methods. A common technique is to embed physical features with known positions into the image during acquisition. This produces a set of known points called “Reseau” marks that can be correlated between images before and after a geometric disturbance.

The use of bilinear equations to model the geometric distortion process within the quadrilateral region is a popular spatial transformation method. The equations below characterize the x and y direction displacement.

$$x' = r(x,y) = c_1x + c_2y + c_3xy + c_4 \quad (2.3)$$

$$y' = s(x,y) = c_5x + c_6y + c_7xy + c_8 \quad (2.4)$$

Corresponding quadrilateral regions between the input and output images produce a total of eight known tiepoints. The above equations can be solved for the eight coefficients (c_i , $i = 1, 2, \dots, 8$) which represent the geometric distortion model that is used to transform the pixels located in the quadrilateral region. For this method to be effective, enough tiepoints are needed to cover the entire image with quadrilateral regions. Once the coefficients have been generated, the process of reconstructing the image becomes trivial. To find the value of the undistorted image at any point (x_0, y_0) , it is necessary to know where the original distorted image $f(x_0, y_0)$ was mapped to. To find this, substitute (x_0, y_0) into the set of bilinear equations to generate the geometrically distorted coordinates x_0' and y_0' . Since $g(x_0', y_0')$, is the value of the point in the undistorted image that was mapped to (x_0', y_0') , the restored point $\hat{f}(x_o, y_o)$ is equal to $g(x_0', y_0')$. An example of this process would be to generate the restored pixel $\hat{f}(x_o, y_o)$. This is simply done by substituting $(x, y) = (0, 0)$ into the bilinear equations to obtain (x', y') , and setting $\hat{f}(x_o, y_o)$ equal to $g(x', y')$ where x' and y' are the points just calculated. This process is repeated for all the remaining pixels to restore the entire image.

Polynomial approximation is another method that uses tiepoints between the input and output images to model the geometric distortion process. In this method the

functions $r(x,y)$ and $s(x,y)$ are given by polynomial equations in x and y of degree N whose coefficients P and Q represent the matching points the of distorted and corrected images respectively. The polynomial approximations are given in Equations 2.5 and 2.6.

$$x' = r(x, y) = \sum_{i=0}^N \sum_{j=0}^N P_{i,j} x^j y^i \quad (2.5)$$

$$y' = s(x, y) = \sum_{i=0}^N \sum_{j=0}^N Q_{i,j} x^j y^i \quad (2.6)$$

The coefficients can be determined by solving a set of linear simultaneous equations involving the known matching points between the images. Solving for $(N+1)^2$ coefficients requires a minimum of $(N+1)^2$ independent pairs of points. If possible, it is recommended to use a higher number of matched point pairs than needed to minimize the mean squared error of the reconstructed image. The polynomial order is determined by a trade-off between accuracy and computational cost. In a relatively simple geometric distortion where the transform does not change rapidly over the image, a degree of $N = 2$ or 3 with approximately 8 pairs of corresponding points is sufficient to reconstruct the image. The matching points between the images must be distributed uniformly across the entire image. As the degree of the approximating polynomial increases, the method becomes more sensitive to the distribution of the pairs of corresponding points in the transform.

2.3.2 Gray Level Interpolation

To regenerate an image it is necessary that the output contain only integer pixel values. This is because the digital nature of the image only defines gray level values on integer

components. Under some circumstances it is possible that the spatial transformation method will calculate non-integer values for x' and y' , causing mapping to locations where no gray level values are assigned. Gray level interpolation modifies the gray level values to account for this occurrence.

Nearest neighbor approximation is the simplest method of gray level interpolation. Also known as zero-order interpolation, the gray level value is chosen to be the integer value closest to the calculated (x',y') point. This method is illustrated in Figure 2.13.

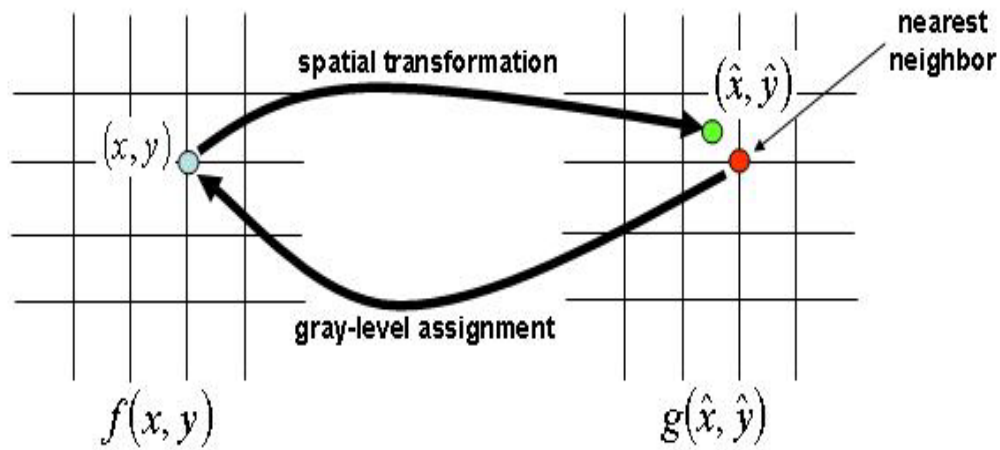


Figure 2.13: Gray Level Interpolation using Nearest Neighbor Approach [25].

Figure 2.13 shows first the mapping of the original point (x,y) to the geometrically transformed point (x',y') , second the selection of the nearest integer gray level value, and thirdly the assignment of the gray level value to the reconstructed image [25]. Although the nearest neighbor approach is easily implemented, it often produces undesirable effects in higher resolution images, such as the distortion of straight edges producing step like boundaries at transitions.

For smoother results a bilinear interpolation process is used for gray level interpolation. The bilinear interpolation method chooses a gray level value based on the gray levels of its four surrounding neighbors. In this case a gray level value is actually interpolated using a bilinear equation instead of just being chosen because it is the closest gray level. The interpolated gray level value is denoted as $v(x',y')$, and can be calculated using the following bilinear equation:

$$v(x', y') = ax' + by' + cx'y' + d \quad (2.7)$$

Since the gray level values of the four nearest integer neighbors are known, $v(x',y')$ can be interpolated. The four unknown coefficients can easily be determined by the four equations from the known integer neighboring points of (x',y') . When these values are determined, $v(x',y')$ is calculated and assigned to the reconstructed image $f^{\wedge}(x,y)$. This process helps reduce the rigid edges produced from the nearest neighbor approach.

2.4 Density Estimation

In pattern classification, density estimation techniques are essential to produce optimal classifiers. Prior probabilities $p(\omega_i)$ and class conditional densities $p(x|\omega_i)$ are rarely known in pattern recognition problems making it difficult to design or train classifiers. Furthermore, Bayes classifier, a benchmark of pattern recognition algorithms, can rarely be used without the knowledge of the probability distributions [26]. Fortunately methods exist for parameter and distribution estimations.

Parameter density estimation techniques assume the distribution of the probability is known and thereby reducing the problem to estimation of parameters such as mean and variance. Methods such as the Maximum Likelihood Estimation and Bayesian Estimation provide good techniques for parameter estimation but assuming a classic

distribution is not always correct. In most cases the distribution functions are not known and hardly ever fit the common distribution function assigned. Also most probability densities are multimodal as opposed to the unimodal distribution of classic probability densities. Additionally, it is difficult to achieve a multidimensional density by taking the product of a one-dimensional function. For these reasons nonparametric density estimation techniques can be used to create arbitrary distributions without the knowledge of the underlying densities.

Density estimation techniques rely on the assumption that the probability P that a vector x will lie in region R given by:

$$P = \int_R p(x') dx' \quad (2.8)$$

By this assumption P represents an averaged version of the density function $p(x)$. The density function $p(x)$ can be estimated by determining the probability of P . Consider the example where a large number of n fish are observed and all those with a length that falls into a range predefined by R are counted resulting in the value k . This allows an estimation of the probability P by performing the ratio k/n as $n \rightarrow \infty$. Therefore the integral can be approximated by the product of the density function and the volume enclosed by the region R , or by the ratio of the area to the volume of the region otherwise determined as k/n [29]. This can be seen in Equation 2.9.

$$P = \int_R p(x') dx' \approx p(x)V \approx \frac{k}{n} \quad (2.9)$$

To ensure an accurate estimate of $p(x)$, it is necessary to have a vast amount of data points that correspond to the region R . This can be done by fixing the volume V enclosed by R and taking more samples that fall inside this region. This will make certain that k/n

will approach the probability P , but unfortunately this will only produce an estimate or average of $p(x)$ due to the variance of P in any nonzero volume region. In order to obtain a true value of $p(x)$, as opposed to just an averaged value, the volume of the region must approach a value of zero while the number of samples is held constant. However, in common practice there is only a finite number of sample points, allowing for the possibility of an arbitrarily shrinking volume to become small enough to contain no samples. This would provide a result of $k = 0$ making the density function $p(x)$ also equal to zero rendering the result worthless. Therefore a small amount of variance is required when determining the value of $p(x)$ producing a tradeoff when determining the size of the volume. The volume must be large enough to ensure an adequate number of samples falls inside the region, but small enough that $p(x)$ remains constant in that region.

In order to adhere to these limitations the following procedure in Equation 2.10 is used. When estimating the density at x , a sequence of regions $R_1, R_2 \dots R_n$ that contain x are formed. The first region created is used with one sample, the second with two samples and continued on where R_i is used with i samples.

$$p_n(x) = \frac{k_n / n}{V_n} \quad (2.10)$$

V_n designates the volume enclosed in region R_n , k_n is the number of samples that lie in the region R_n , and $p_n(x)$ is the n th estimate for $p(x)$ [26]. In order for $p_n(x)$ to be an accurate estimate of $p(x)$, the following three conditions must be met:

- $\lim_{n \rightarrow \infty} V_n = 0$
- $\lim_{n \rightarrow \infty} k_n = \infty$
- $\lim_{n \rightarrow \infty} k_n / n = 0$

The first condition is necessary to ensure the space averaged value P/V will converge to $p(x)$ providing that the region's volume shrinks uniformly and the density function is continuous at x . The second condition is needed to guarantee that the frequency ratio k_n/n will converge to the probability P . Finally the third condition is essential to make sure that the estimate $p_n(x)$ will converge to the true value of $p(x)$ [26].

Two techniques commonly used for nonparametric density estimation that adhere to the above criteria are Parzen windows and K- Nearest Neighbors (KNN). The Parzen windows method, also known as Kernel Density Estimation, aims to shrink the region R by making the volume V_n a function of the total number of samples n . The KNN method updates the k value by making it a function of n so that V_n increases in size until it encloses k_n samples. The changing size in the volume V_n ensures that both Parzen windows and KNN will converge to an accurate density estimation of $p(x)$ as $n \rightarrow \infty$.

2.4.1 Parzen Windows

As previously stated, the Parzen windows method provides a true density estimation by reducing the size of the region as the number of samples in the region increases. In order to determine the number of samples entering into the region k_n , a window function must be used. For explanation purposes, the region R_n will be assumed to be a d -dimensional hypercube with edge length h_n [26, 27, 28]. The resulting volume of the hypercube is given below in Equation 2.11.

$$V_n = h_n^d \quad (2.11)$$

The window function $\varphi(u)$ is defined as a unit hypercube that is centered at the origin seen in Equation 2.12.

$$\varphi(u) = \{1, |u_j| \leq 1/2, j = 1, \dots, d; \text{ or } 0, \text{ otherwise}\} \quad (2.12)$$

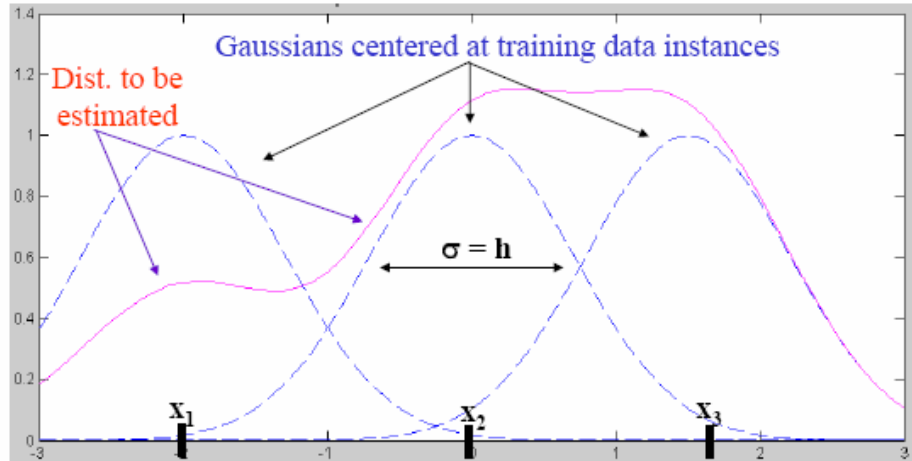
Therefore the window function $\varphi((x - x_i) / h_n)$, centered at x , will be equal to one when x_i falls inside the unit cube, and equal to zero otherwise. The number of samples in the hypercube is then given by:

$$k_n = \sum_{i=1}^n \varphi\left(\frac{x - x_i}{h_n}\right) \quad (2.13)$$

By inserting this into Equation 2.10 the following estimate of the density is attained seen in Equation 2.14. This results in a density estimation of the number of samples falling into the region, when the region is centered at x and has a width of h . V represents the volume encompassed by the region, φ is the window kernel function, and h demonstrates the width of the window function [29].

$$\tilde{p}(x) = \frac{1}{n} \sum_{i=1}^n \frac{1}{V} \varphi\left(\frac{x - x_i}{h_n}\right) \quad (2.14)$$

For application purposes the hypercube window function can be substituted with a smoother more continuous generalized function. Under this scenario the density estimation $\tilde{p}(x)$ becomes the superposition of the window functions. This allows for a type of interpolation where the window function contributes to the estimate by determining the distance each sample is from x . Typically, x_i are the training data points being used where x is the point the density estimation is being performed. The object of the window function is to numerically determine the distance between each x_i and x .



In the case of using a normal or Gaussian function, the density estimation would be determined by centering each Gaussian over the training data instances and taking the superposition of the overlapping areas to provide a distribution. The window width parameter h would then pertain to the variance of each Gaussian. Figure 2.14 helps to further explain this concept [29].

The window width parameter h also acts as a smoothing variable or bandwidth feature and has a great impact on the accuracy of the density estimation. If the value of h is too large, then the result will become a more generalized summation of the density. This is because the width of the window is so large it will now encompass all points surrounding x . On the other hand, a small value for h will create a very narrow window causing most points to fall outside of the window. The result of this is essentially over fitting the data causing multiple sharp pulses for the density that represent mainly noise. Optimal conditions would provide a wide window when the data is sparse and a narrow window for more densely populated data.

2.4.2 K- Nearest Neighbor

The K-Nearest Neighbor technique offers a solution to the variability in the h parameter, by making the window width a function of the actual training data rather than that of the overall number of samples. The KNN methods computes the density $p(x)$ at a specific point by centering the volume V_n around that point x . The volume is then increased until it captures k_n number of points, where k_n is a fixed specified function of n . KNN determines the optimal window function automatically in each case providing a narrow window when the density of points is high, and a wider window otherwise. Once the volume encompasses the k -nearest neighbors to x , the density is estimated in that area using Equation 2.15.

$$p_n(x) = \frac{k_n / n}{V_n} \quad (2.15)$$

Although KNN provides a more accurate kernel size, it does have drawbacks that can make the Parzen windows technique a better choice for density estimation. The disadvantages include highly noisy density estimations, densities that are often discontinuous, and in some cases of k values $p(x)$ will diverge making the estimation not a density at all. It should be noted that larger values of k and n will increase the accuracy of the density estimation greatly, thereby proving its viability as a quality density estimation technique.

CHAPTER 3: APPROACH

The primary objective of this research is to develop multi-sensor NDE data fusion algorithms for the prediction of information fusion measures – redundancy and complementarity (as illustrated in Figure 1.4); specifically to include the effects of defect size and sensor data heterogeneity. The approach proposed in this thesis expands on previously developed work in invariance transformations for compensating NDE signatures for the effects of variations in operational parameters [30, 31, 32, 33, 34], and NDE image fusion for determining defect location [12, 13]. The heart of the algorithm, in both these previously established methods is a geometric transformation technique that uses radial basis function neural networks as a “Universal Approximator” [35].

Most often NDE inspection signatures from different interrogation methods vary in dimensionality and information content making data fusion a challenging task. This is evident when combining heterogeneous datasets such as two-dimensional images containing information related to defect size and location (e.g. a UT signature), and one-dimensional vectors containing information regarding possible defect location (e.g. AE signal intensity “hits”). The approach taken in this thesis is to first ensure that the information obtained from these heterogeneous datasets possess the same dimensionality, thereby allowing the application of previously developed data fusion algorithms. It therefore becomes necessary to first transform the NDE datasets to be equivalent in dimension and information before a data fusion process can be applied.

This chapter outlines a generalized procedure for combining NDE signatures of varying dimensionalities. The two independent NDE signals are assumed to have originated from the same scene or test specimen and are combined through the data

fusion process outlined in Figure 3.1. The dimensionality transformation process will utilize the Parzen windows density estimation technique. Once each NDE dataset provides equivalent information and dimensionality, the data fusion process can be applied. This process consists of extraction of redundant and complementary information from the transformed NDE signatures of equal dimensionality and similar information attributes.

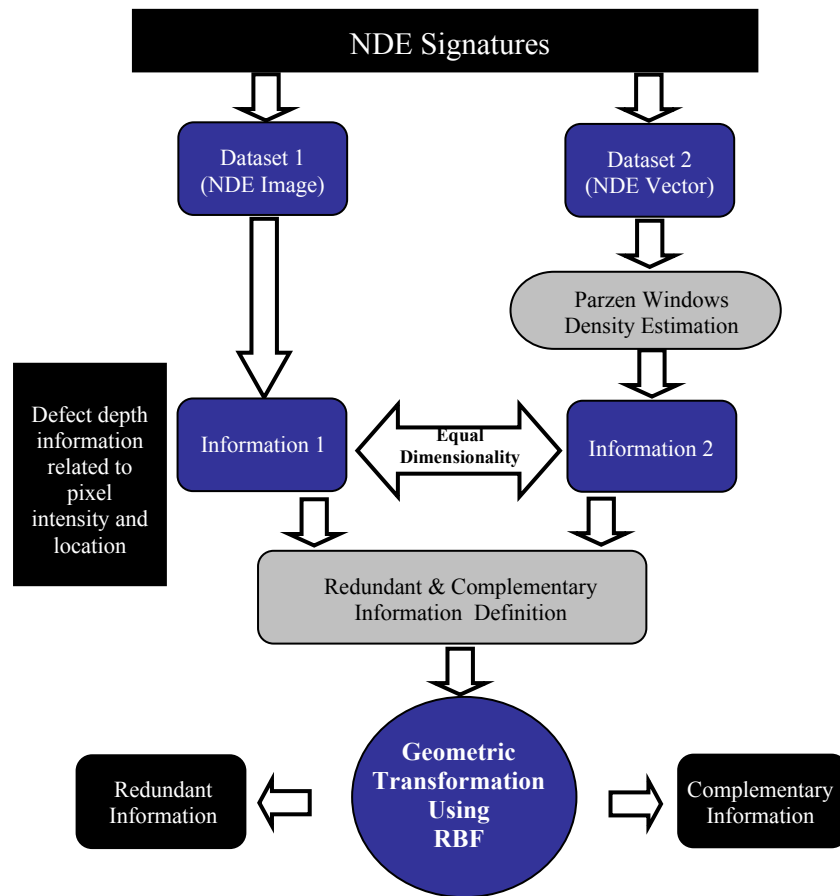


Figure 3.1: Generalized approach for multi-sensor data fusion.

3.1 Definition of Redundant and Complementary Information

The fused NDE data provides two main types of information: redundant and complementary information. Redundant information is the common information present among NDE signatures. Redundant information increases the confidence and reliability of the prediction by the combination of more than one signature. Complementary information is the novel information that is different between the NDE signatures obtained from each source. Complementary information reveals features that are unique to each source and can be used to further characterize a defect and improve accuracy [13]. Figure 1.4 illustrates the resulting redundant and complementary information from the data fusion process.

3.2 Dimensionality Transformation using Parzen Windows

This technique is designed to account for NDE signatures of different dimensionality and information content when performing data fusion. Many NDE inspection modalities, including ultrasound, MFL, X-ray, eddy-current, and thermal imaging, provide two-dimensional images. NDE images provide a matrix of numbers that represent the (x, y) position, along with the measurement data corresponding to that position. This measurement data can possibly represent the magnitude of the magnetic flux density or the C-scan amplitude providing a measure of defect location and size. Other NDE inspection techniques, such as acoustic emission, generate scatter plots of A-scan amplitudes at specific (x, y) positions that can be related to the location of the defect but provides no information related to defect size.

To perform data fusion with the measures defined in this approach, the NDE signatures must be equivalent in dimensionality and information type. The amplitude

scatter plots must be transformed to two-dimensional images with pixel gray level values indicative of defect size and location. As explained in Section 2.3.3, in acoustic emission NDE, multiple scatter plots can be used to triangulate the location (or presence) of the defect. Laboratory results (shown in Chapter 4) confirm that acoustic emission sources cluster around the defect. Separable clusters can be transformed into two-dimensional images using density estimation techniques. The Parzen windows density estimation technique fits a two-dimensional Gaussian distribution whose parameters are determined by the variance and amplitude of the AE data points. The possible location of the defect is determined by the areas where the Gaussian distributions from each cluster overlap. The overlapped region is depicted in a two-dimensional image whose pixel gray level values contain defect related information similar to other NDE inspection modalities.

In order to generate the equivalent two-dimensional NDE images from acoustic emission signatures, the Parzen windows density estimate is given by

$$\tilde{p}(x, y) = \frac{1}{n} \sum_{i=1}^n \frac{1}{V} z_i \frac{1}{\sqrt{2\pi}} e^{-\frac{1}{2} \left(\frac{x-x_i}{h_n} \right)^2 + \left(\frac{y-y_i}{h_n} \right)^2} \quad (3.1)$$

where x , y , and z represent the x position, y position, and amplitude of the AE source respectively, V is the volume encompassed by the region, and h represents the width of the window function.

3.3 Geometric Transformations

As previously stated, the redundant and complementary data fusion extraction process will be based on geometrical transformations. As detailed in the background chapter, geometric transformations are typically an image processing technique used to reverse distortion in images. Geometric transformations consist of two operations including

spatial transformations and gray-level interpolations. The goal of spatial transformations is to apply a set of equations to transform the distorted image pixels to the location of the corresponding correct image pixels. Gray-level interpolation ensures integer gray level values are assigned to the spatially transformed pixels. The entire process of geometric transformations can be thought of as morphing one image to resemble another by subjecting the initial image to a set of predetermined transformation equations. As long as transformation equations are known, the geometric transformation process can be applied and reversed with minimal loss of information. The correct geometric transformation may allow features of the original image to be enhanced and suppressed as desired. It is this feature that makes geometric transformations ideal for the extraction of desired information.

In this manner, geometric transformations are utilized to develop two separate data fusion techniques including a redundant data extraction method and a complementary data extraction method. In either data extraction method, geometric transformations are used to suppress one type of information while enhancing the other. In order to determine the appropriate geometric transformation equation to extract a single type of information, the universal approximator is utilized.

Under the correct circumstances, each data fusion method should provide results invariant to the other. Therefore the redundant information extraction should be invariant to the complementary information extraction and vice versa. Consider the results of two different inspection modalities performed on the same testing specimen yield $x_1(r, c_1)$ and $x_2(r, c_2)$. In this case, r would represent the redundant information found in the two data

sets since it is the same for both signals. Similarly, c_1 and c_2 vary between the signals representing the complementary information found in the data [32].

In order to perform data fusion on this level, explicit functions must be developed based on the specific signal features being analyzed. The function's designation will be given as h to parameterize the features r , c_1 , and c_2 . As stated earlier it is necessary to develop two separate data fusion algorithms one for the extraction of redundant information and the other for the extraction of complementary information. For demonstration purposes only the redundant extraction method will be outlined. In order to create the redundant data extraction technique, h will be a user defined function of the two input signals x_1 and x_2 that must be invariant to the complementary information of c_1 and c_2 . The described function is defined in Equation 3.2.

$$f\{x_1(r, c_1), x_2(r, c_2)\} = h_1(r) \quad (3.2)$$

The addition of two arbitrary functions g_1 and g_2 modify the existing equation, allowing for $h_1(r)$ to be determined by the following equation:

$$h_1(r) \diamond g_1(x_1) = g_2(x_2) \quad (3.3)$$

In this case \diamond represents a homomorphic operator (any operator for which an inverse exists). For this application, the addition operator (+) was chosen for the homomorphic operation, which yields the following result seen in Equation 3.4.

$$h_1(r) + g_1(x_1) = g_2(x_2) \quad (3.4)$$

To continue with this process the arbitrary functions of h , g_1 and g_2 must be defined. The function h is a user defined function that can be altered depending upon the needs of the user. In this situation g_2 is an application dependent conditioning function that can be altered to adjust the data to provide optimal results. For example, g_2 could be

chosen as a logarithmic function to adjust for a wide spread of values in x_2 [13]. Since h and g_2 are known, g_1 can be evaluated by using the universal approximation method to determine the function that equates g_1 to following expression in Equation 3.5 and thereby providing the function to extract the redundant information.

$$g_1(x_1) = g_2(x_2) - h_1(r) \quad (3.5)$$

In order to approximate the function g_1 , the radial basis function (RBF) neural network is used. Ideally, the RBF neural network will produce the best results if given the proper training data. The activation function for the RBF neural network that will be the model of g_1 can be viewed below in Equation 3.6

$$g_1 = \sum_{j=1}^m \lambda_j \phi(\|x_i - c_{ij}\|) \quad (3.6)$$

In this equation the variable λ_j represents the hidden layer node weight for the j th iteration. The window function or basis function of the neural network is denoted by ϕ , which was chosen as the Gaussian window function given in Equation 3.7. The Gaussian window function has a variance of σ and a mean of c_{ij} .

$$\phi_{ij}(\|x_i - c_{ij}\|) = e^{-\frac{\|x_i - c_{ij}\|^2}{2\sigma^2}} \quad (3.7)$$

Equation 3.8 displays the redundant data extraction process when the conditioning function g_2 is set to unity. In this equation, x_1 is the training data input to the RBF neural network while the expression $x_2 - h_1(r)$ represents the training data output. The RBF neural network training process can be viewed in Figure 3.2.

$$g_1(x_1) = x_2 - h_1(r) \quad (3.8)$$

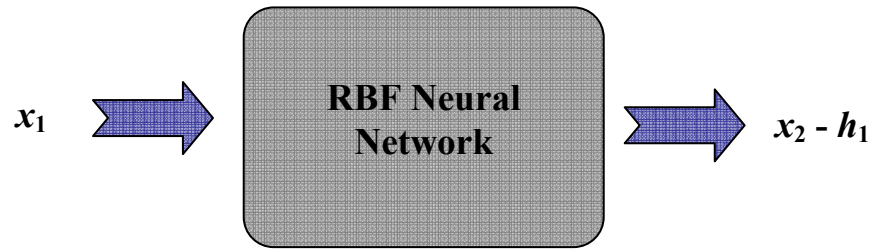


Figure 3.2: Block diagram of the redundant data extraction RBF training process [13].

Once the RBF neural network has been properly trained with the training data set, the network can be tested using the remaining data. Again the x_1 testing data set is fed into the system. In this case the redundant data is isolated from the rest of the equation by subtracting x_2 from the equation and inverting the output. This produces the effective extraction of the redundant information with a final output of $h_1(r)$. This is evident in Equation 3.9 and is displayed in Figure 3.3.

$$h_1(r) = x_2 - g_1(x_1) \quad (3.9)$$

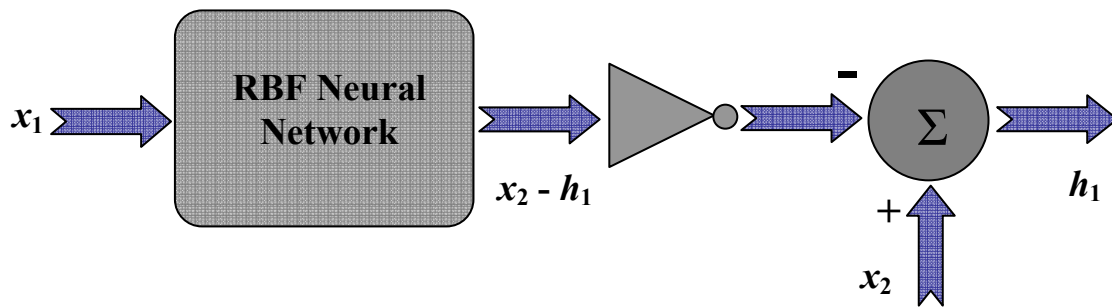


Figure 3.3: Block diagram of the redundant data extraction RBF testing process [13].

The complementary data extraction method follows the same procedure as the redundant method with the exception that h is now a function of x_1 and x_2 that is invariant to r . The resulting RBF neural network will now be trained and tested with complementary data thereby solving for $h_2(c_1, c_2)$ as seen in Equation 3.10.

$$f\{x_1(r, c_1), x_2(r, c_2)\} = h_2(c_1, c_2) \quad (3.10)$$

Results demonstrating the redundant and complementary data extraction processes performed on ultrasound, MFL, thermal imaging, and acoustic emission data are presented in Chapter 4.

CHAPTER 4: IMPLEMENTATION AND RESULTS

This chapter describes in detail the implementation of the algorithms and methods for performing multi-sensor NDE data fusion that are developed in this thesis. Experimental NDE data using the following inspection methods was collected in the laboratory: ultrasonic testing (UT), magnetic flux leakage (MFL), thermal imaging, and acoustic emission (AE). A comprehensive test specimen suite representative of actual pipe-wall anomalies was fabricated and subjected to the above-mentioned NDE methods. Details of the test setup and the NDE experiments are described first. Next, results demonstrating the identification of redundant and complementary in both homogeneous and heterogeneous data combinations are presented. Finally, results comparing the effectiveness of the algorithm for various NDE signature combinations are provided.

4.1 Experimental Setup

4.1.1 Test Specimen Suite

Two different sets of test specimens were needed to perform both the homogeneous and heterogeneous data fusion processes. The test specimen suite was designed to provide the diversity of NDE data when subjected to multi-sensor inspection. For the homogeneous case, the test specimens were developed to demonstrate pitting corrosion in the pipe wall. 6" x 4" test specimens were fabricated using ASTM 836 steel stock representing pipe-wall thicknesses of 5/16, 3/8, and 1/2 inch – these can be seen in Figure 4.1. Three specimens, one of each thickness, have been fabricated without any defect as shown in Figure 4.1(a), while Figure 4.1(b) displays one of the specimens that mimics pitting corrosion. A total of nine slotted defect specimens were fabricated using a milling machine to create test specimens with defect depths of 0.1, 0.2 and 0.3 inches for each of

the three specimen thicknesses. Table 4.1 describes test specimen suite 1 used for the combination of homogeneous NDE data.

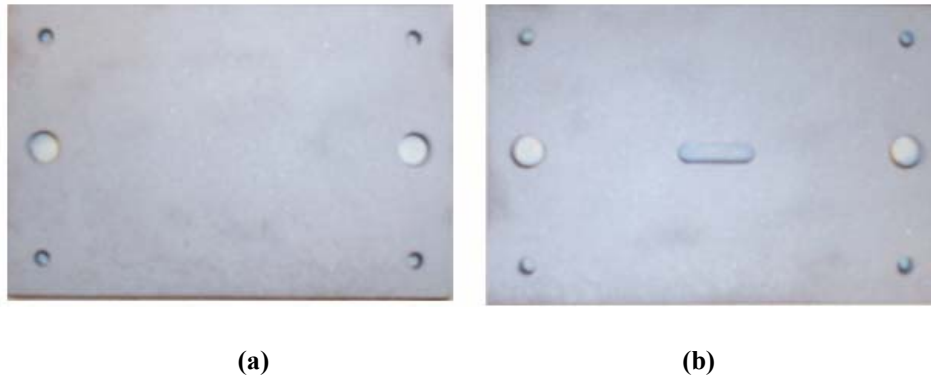


Figure 4.1: Homogeneous test specimen suite.

Table 4.1: Test specimen suite 1 used for homogeneous sensor data fusion [13].

Specimen #	Plate thickness (in)	Indication	Defect Depth (in)
00	0.5	None	N/A
01	0.5	Pitting	0.3005
02	0.5	Pitting	0.198
03	0.5	Pitting	0.0945
10	0.375	None	N/A
11	0.375	Pitting	0.298
12	0.375	Pitting	0.199
13	0.375	Pitting	0.1105
20	0.3125	None	N/A
21	0.3125	Pitting	0.303
22	0.3125	Pitting	0.1955
23	0.3125	Pitting	0.0995

A separate set of test specimens was needed to perform the heterogeneous data fusion. This was necessary to accommodate the testing needs of the acoustic emission system. As specified in the background chapter, acoustic emission testing requires a load or stimulus to be applied to the specimen (usually provided during normal operation) to generate the acoustic energy to be measured. For this reason six new specimens were fabricated that could be stressed on a loading test platform. Two types of specimens were

created to simulate the loading of a pressurized gas pipeline including a uniaxial loaded specimen, and biaxial loaded specimen. The premise behind the uniaxial specimen is to simulate the axial stress along the length of the pipe. The biaxial specimen also mimics the axial stress, but additionally simulates the hoop stress which is the loading around the circumference of the pressurized pipe. Using these guidelines, the uniaxial specimen was designed as length of metal 3 inches wide and 14 inches long. To account for the second loading axis the biaxial specimen was designed as a cross shaped specimen of the same dimension as two perpendicularly overlapping uniaxial specimens. The uniaxial and biaxial specimens can be viewed in Figure 4.2. The design of the AE specimens was based on the recommendations of the Petroleum Environmental Research Forum (PERF) 95-11 Steering Committee. Each specimen is made of ½ inch thick SA-516 grade 70 pipeline steel and has a saw cut ranging in depths of 0.08”, 0.16”, and 0.32” deep. The saw cut defect was chosen to simulate stress corrosion cracking (SCC) in an actual pressurized pipeline. Table 4.2 outlines test specimen suite 2 used for heterogeneous data fusion.



Figure 4.2: Test specimens for AE inspection with biaxial and uniaxial loading.

Table 4.2: Test specimen suite 2 used for heterogeneous sensor data fusion.

Specimen #	Type	Plate Thickness (in)	Indication	Crack Depth (in)
Uni08	Uniaxial	0.5	SCC	0.08
Uni16	Uniaxial	0.5	SCC	0.16
Uni32	Uniaxial	0.5	SCC	0.32
Bi08	Biaxial	0.5	SCC	0.08
Bi16	Biaxial	0.5	SCC	0.16
Bi32	Biaxial	0.5	SCC	0.32

4.1.2 Ultrasound Scanning Test Setup

The laboratory setup for the ultrasonic testing consists of an immersion ultrasound test station seen in Figure 4.3. A 10 MHz piezoelectric transducer was used to perform pulse-echo ultrasonic testing. Precision linear actuators and controlled stepper motors were interfaced via custom hardware to a PC providing real-time control and display of A-scan, B-scan, and C-scan data. Each specimen in the suite was scanned to produce a resultant time-of-flight (TOF), and amplitude ultrasound images to be utilized for defect characterization. Figure 4.4 and 4.5 contain two separate datasets of ultrasound TOF images obtained from the test specimen suite shown in Table 4.1. Figure 4.6 displays the resulting amplitude ultrasound images obtained from the test specimen suite shown in Table 4.2. All of the scanned images in the datasets below have been cropped and registered with a resolution of 100 pixels per inch.

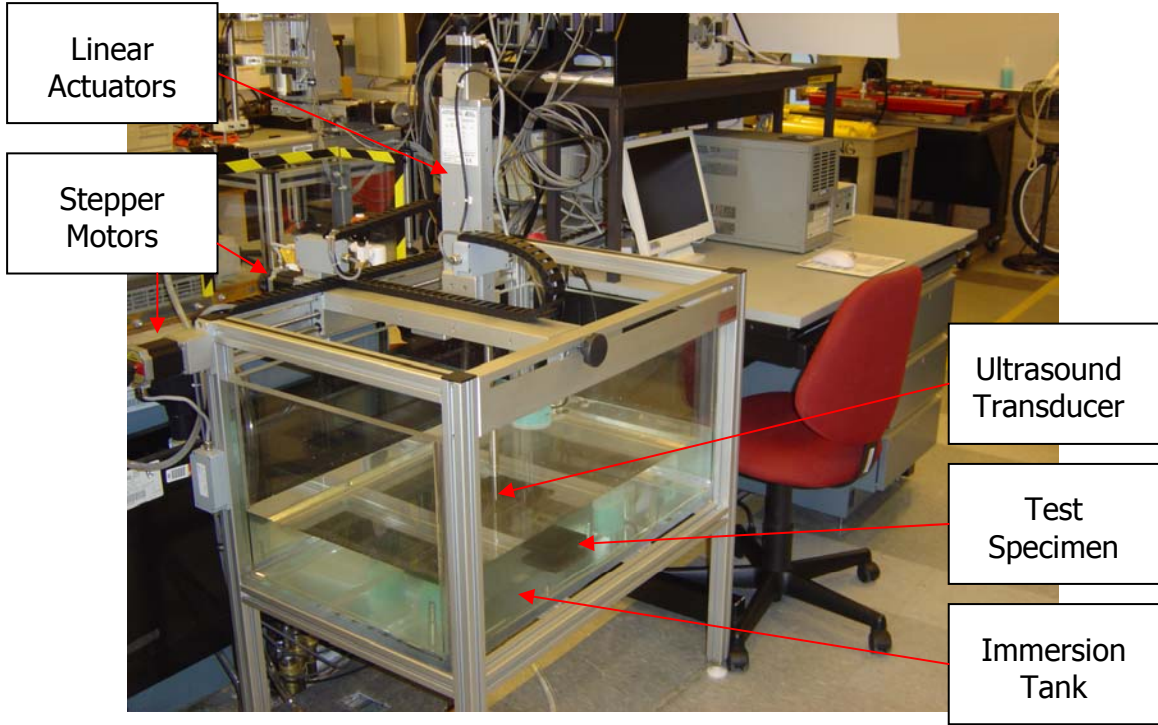


Figure 4.3: Ultrasonic testing station.

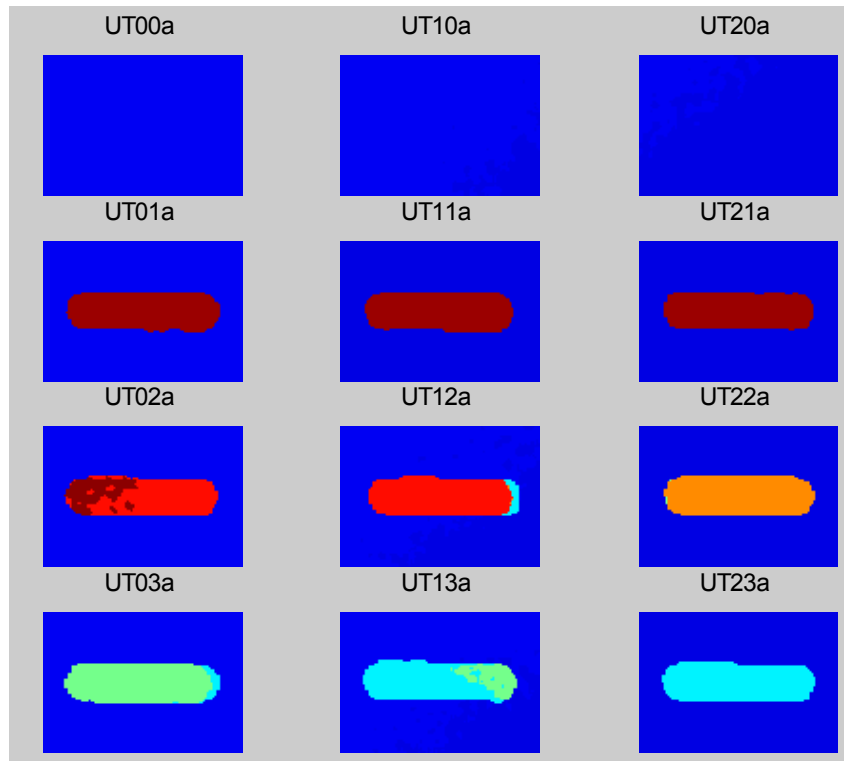


Figure 4.4: UT C-scan TOF NDE signatures from test specimen suite 1: Dataset 1.

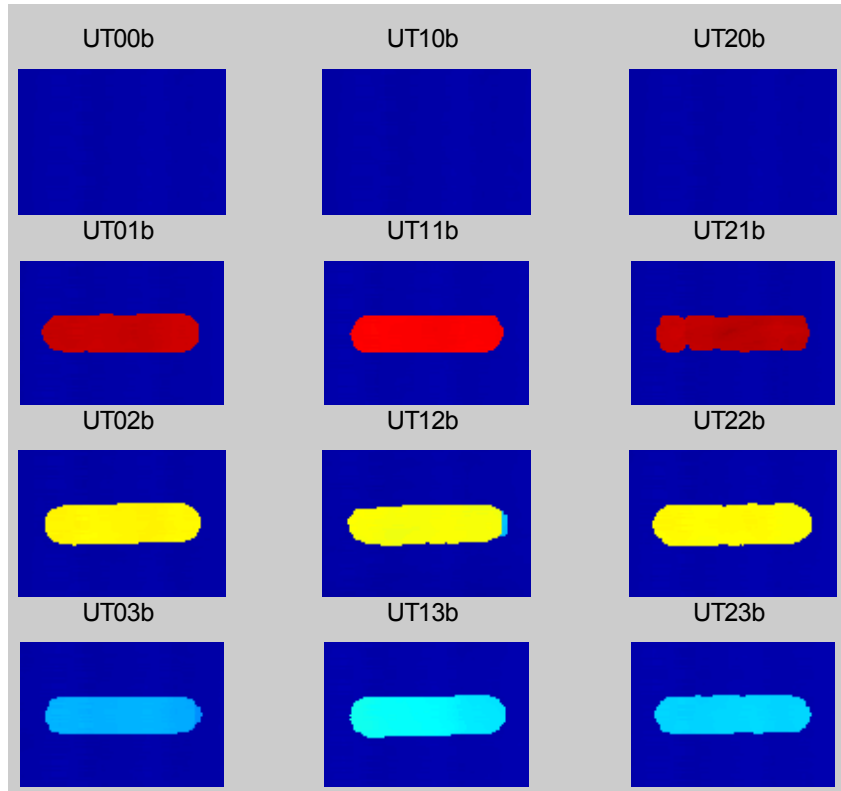


Figure 4.5: UT C-scan TOF NDE signatures from test specimen suite 1: Dataset 2.

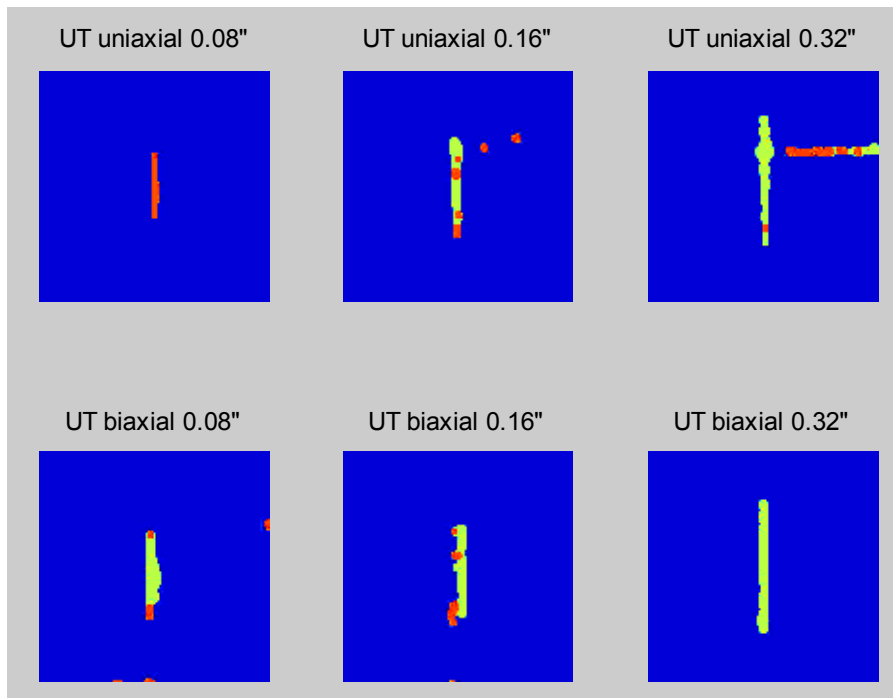


Figure 4.6: UT C-scan amplitude NDE signatures from test specimen suite 2.

4.1.3 Magnetic Flux Leakage Test Setup

The magnetic flux leakage testing platform seen in Figure 4.7 induces the required magnetic field by passing 200 amps through the specimen using a HP 6571A DC high output power supply. The high current generates the magnetic flux that flows through the specimen. An F. W. Bell 9900 Gaussmeter with Hall probe is used to measure the leakage magnetic flux density. The probe scans over the surface area of the specimen using a three directional linear actuator system. A computer and data acquisition software are used to collect the x, y, and z directional components of the magnetic flux density. Figures 4.8 and 4.9 contain two separate datasets of the tangential y component MFL scans of the homogeneous test specimen suite. Again the images seen below have been cropped and register to 100 pixels per inch.

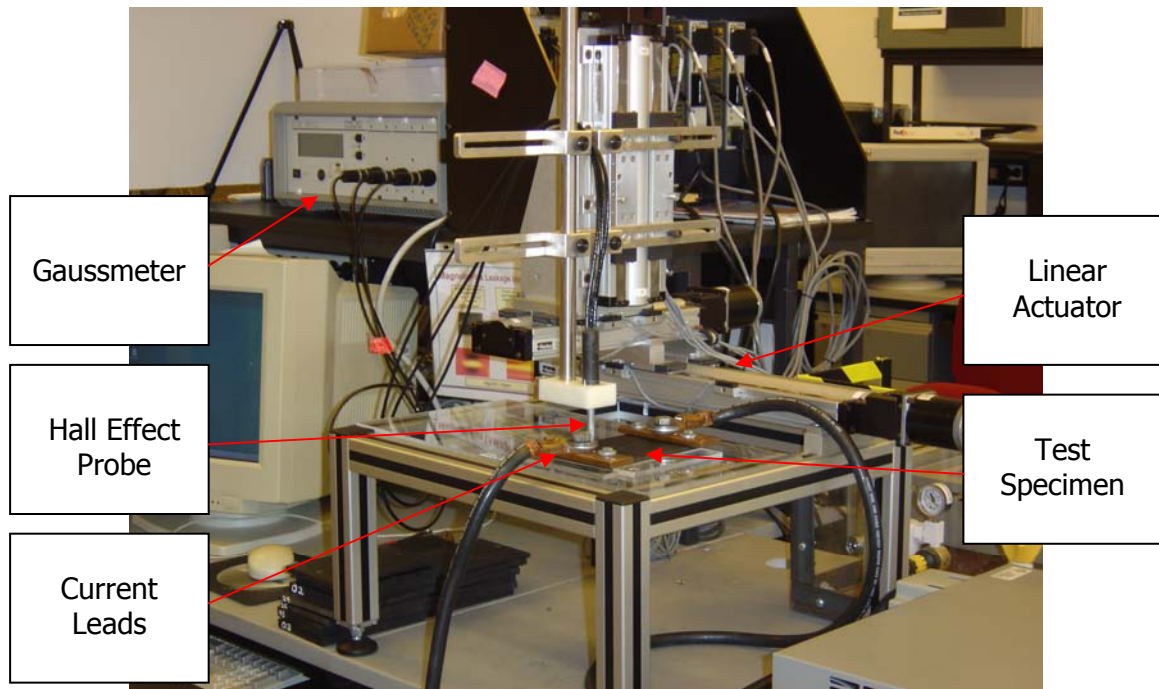


Figure 4.7: Magnetic flux leakage testing system.

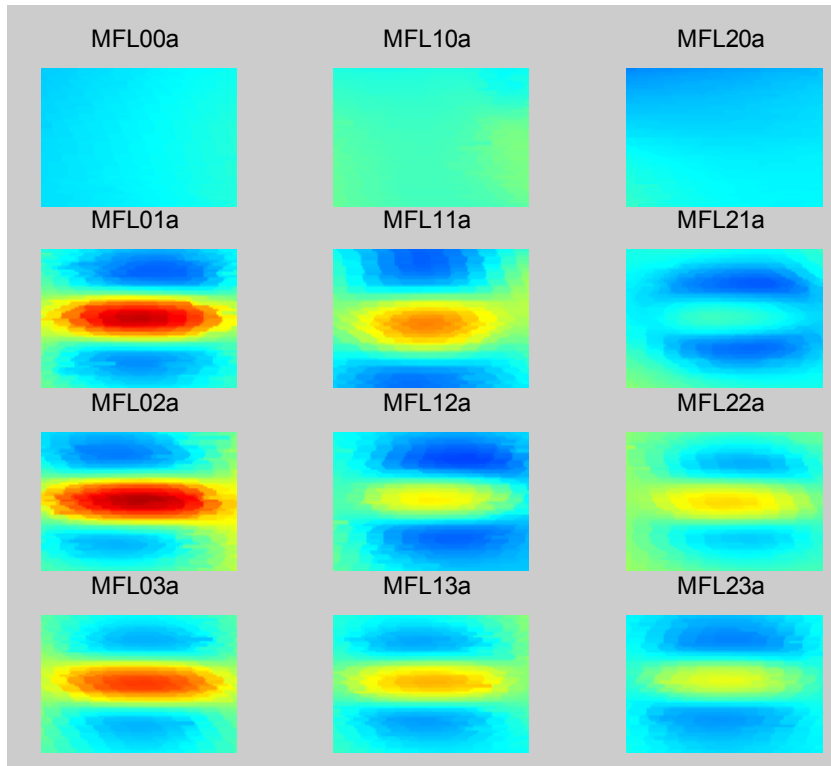


Figure 4.8: Y-component MFL NDE signature for test specimen suite 1: Dataset 1.

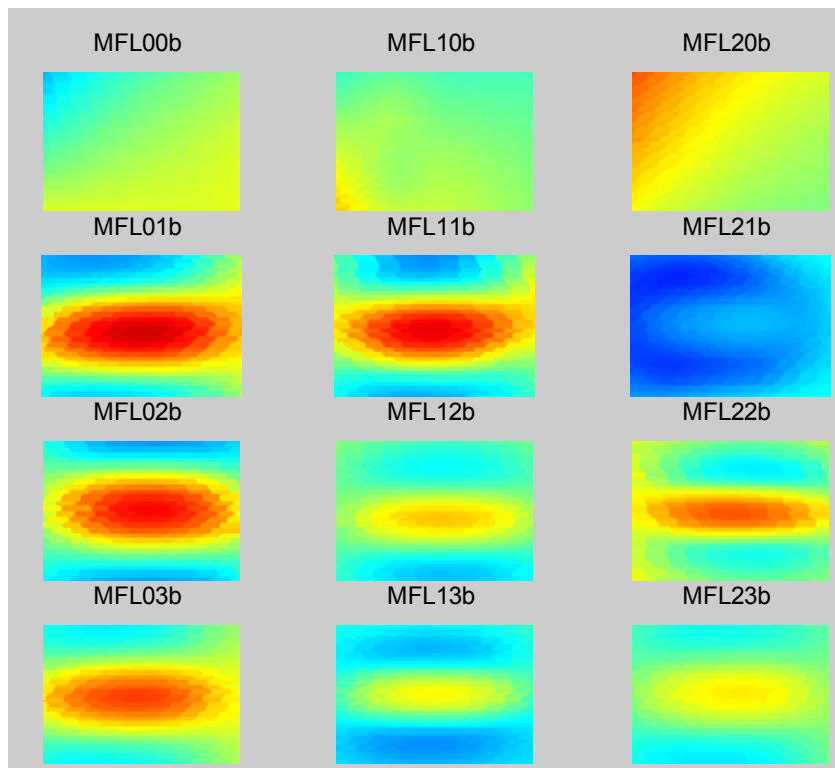


Figure 4.9: Y-component MFL NDE signature for test specimen suite 1: Dataset 2.

4.1.4 Thermal Imaging Test Setup

The thermal imaging test set up is shown in Figure 4.10. Each of the specimens is held upright on a thermally insulated test surface. Two high output 110 W Halogen lamps were directed at the side of the specimen containing the defect. The heat sources were applied for a period of 10 seconds while a highly sensitive FLIR Systems Microbolometer camera was used to capture a thermal image every second over a 20 second interval. The entire experiment is performed in complete darkness to prevent any residual light from interfering with the test. Each 20 second testing period produces 20 images that that can be used to monitor the heating and cooling cycle of test specimen. Depending on the specimen thickness and defect depth the defect is visible sometime during this testing period. The resulting thermal image datasets performed on test specimen suites 1 and 2 can be seen in Figures 4.11 and 4.12 respectively.

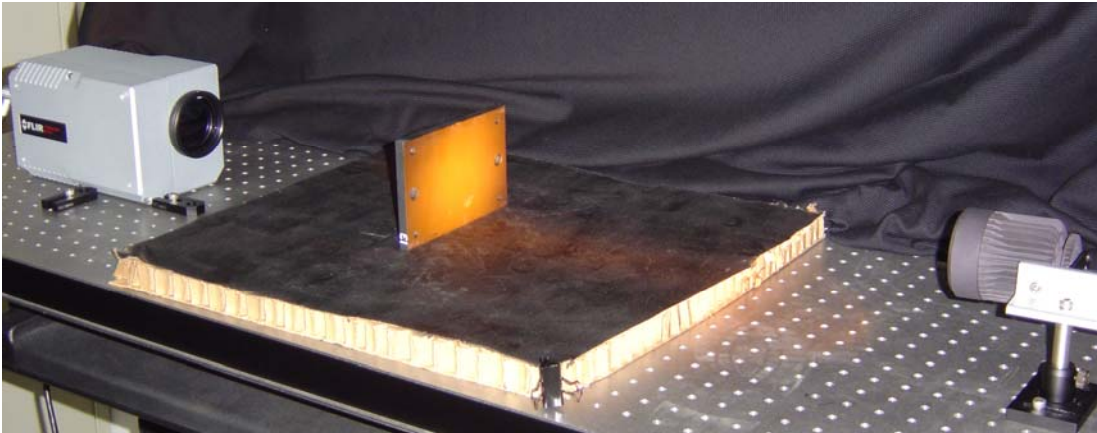


Figure 4.10: Thermal imaging test setup.

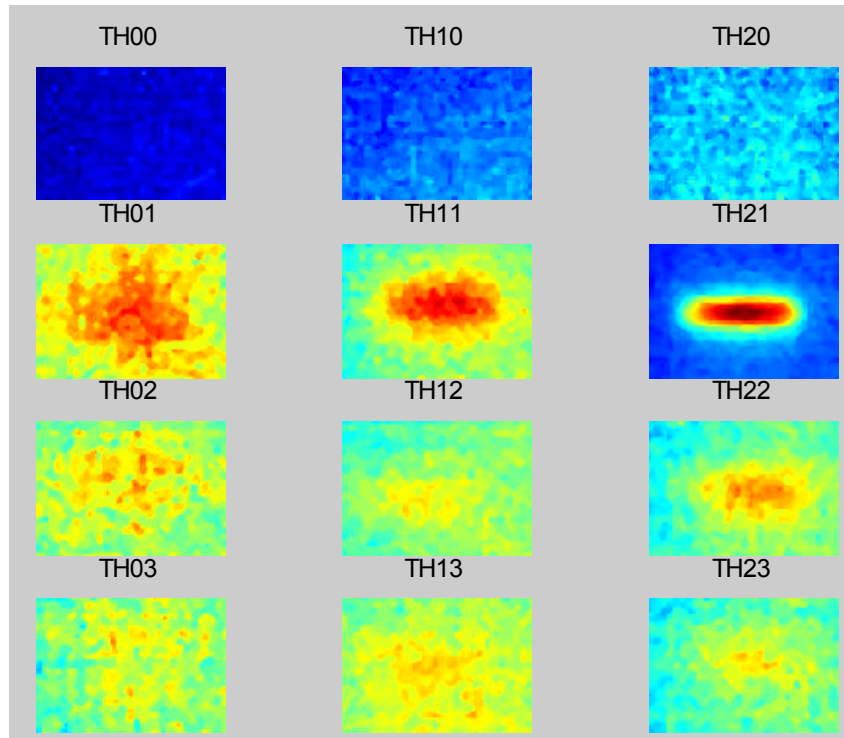


Figure 4.11: Thermal images from test specimen suite 1: dataset 1.

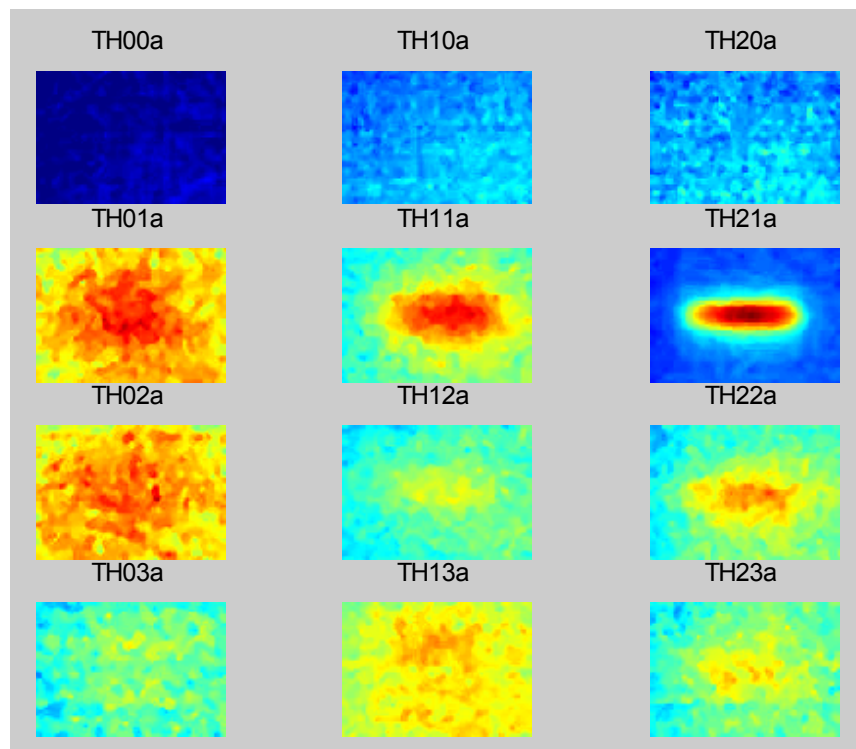


Figure 4.12: Thermal images from test specimen suite 1: dataset 2.

4.1.5 Acoustic Emission Test Setup

The acoustic emission experimental data is collected using a dual axis loading test platform that can be seen in Figure 4.13. The loading platform is designed to reproduce the loading stresses of a pressurized pipeline on the specimens outlined earlier in the heterogeneous test specimen suite. The testing platform utilizes hydraulic rams to apply a maximum of 50,000 lbs along the first loading axis and 25,000 lbs along the second loading axis to simulate the axial and hoop stress of a pressurize gas transmission pipeline. Load cells are used to continually monitor the stress being applied to the test specimen.



Figure 4.13: Acoustic emission loading platform.

A series of nine acoustic piezoelectric sensors interfaced with a computer are monitoring any acoustic emission activity that may occur. The use of multiple sensors allows for triangulation of the acoustic emission source. Figure 4.14 shows the acoustic

emission sensor placement on both the uniaxial and biaxial specimens. Sensors 6, 7, 8, and 9 are configured in an array to detect extraneous noise created by the testing platform from corrupting the acoustic activity generated by the specimen.

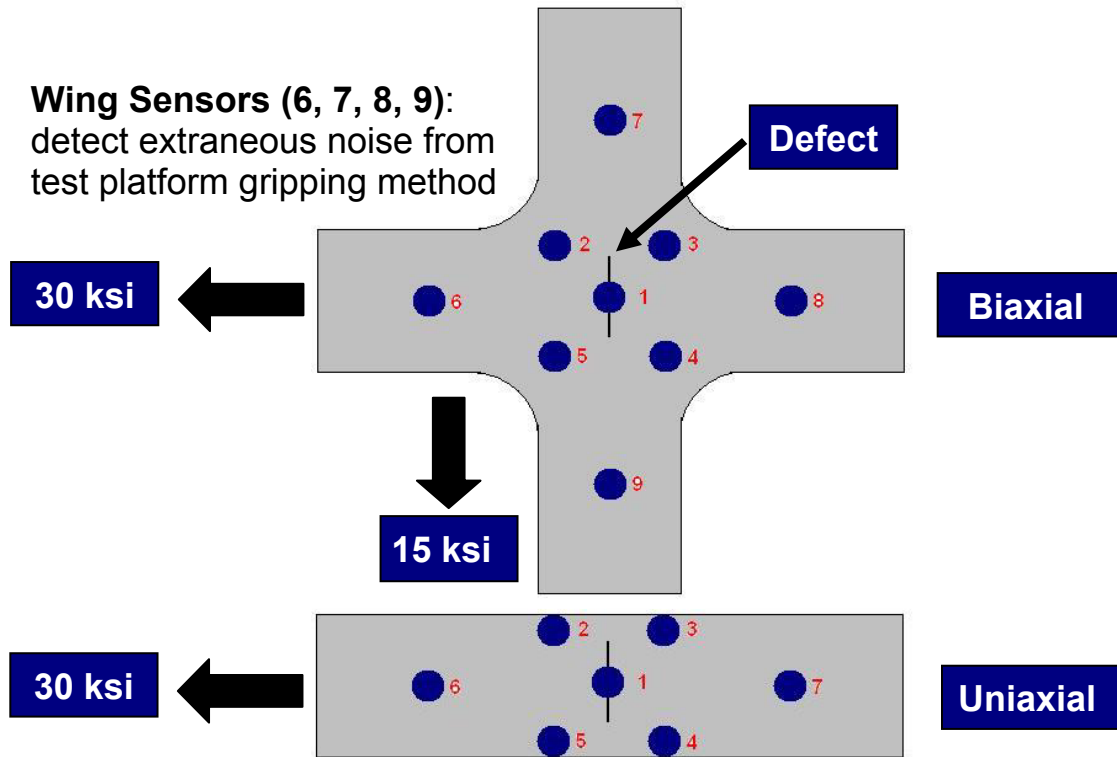
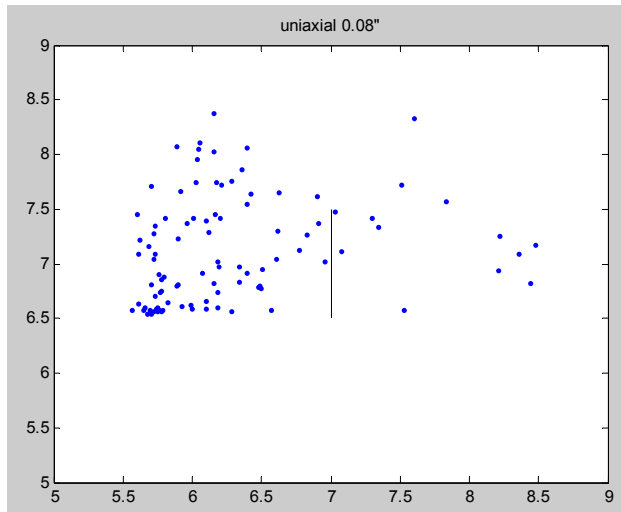
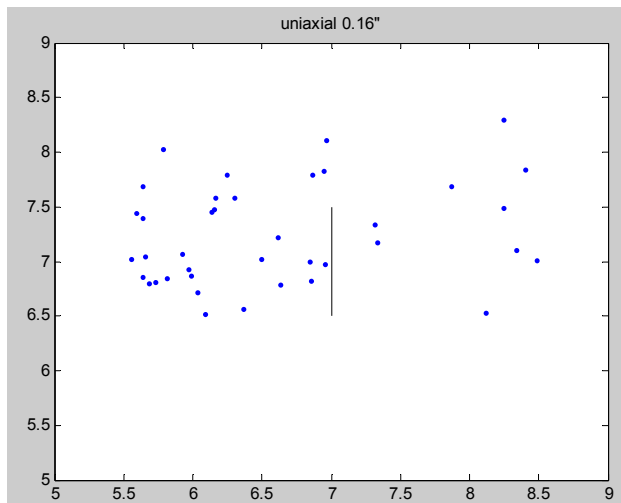


Figure 4.14: Acoustic emission sensor placement.

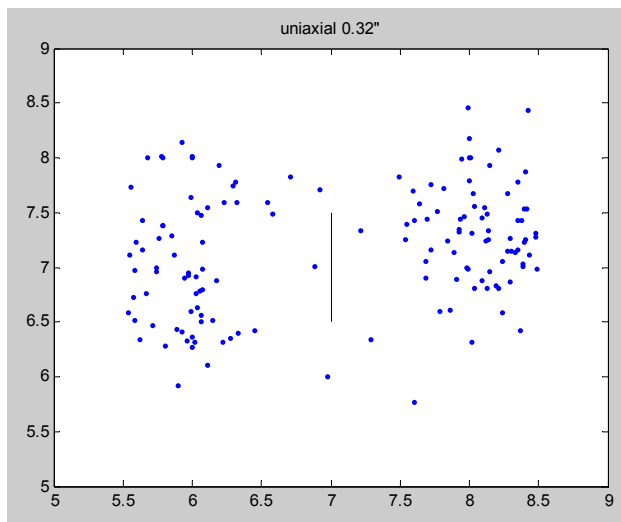
All six specimens in test specimen suite 2 were loaded to 30 ksi in the primary axis and 15 ksi in the secondary axis. The specimens were loaded in steps of 2500 lbs until the desired load was achieved. Acoustic emission sensors 1 through 5 were arranged around the defect to listen for any acoustic activity caused by crack growth during the loading process. The resulting acoustic emission data can be viewed in Figure 4.15(a) through (f). The scatter points represent the acoustic emission sources that could be triangulated with the sensor array. The vertical black line represents the location of the defect.



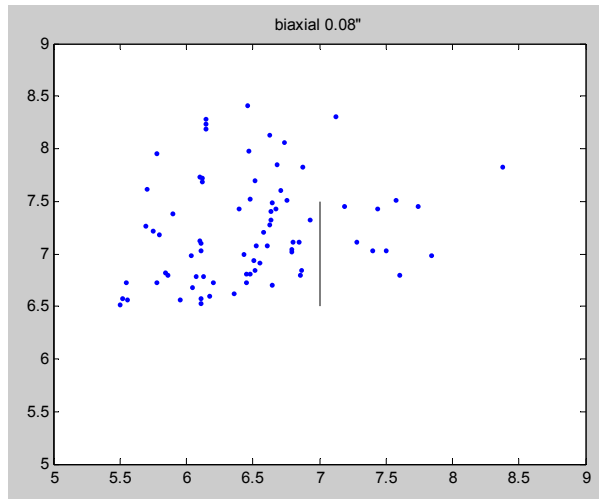
(a) AE data from uniaxial specimen with 0.08" deep defect



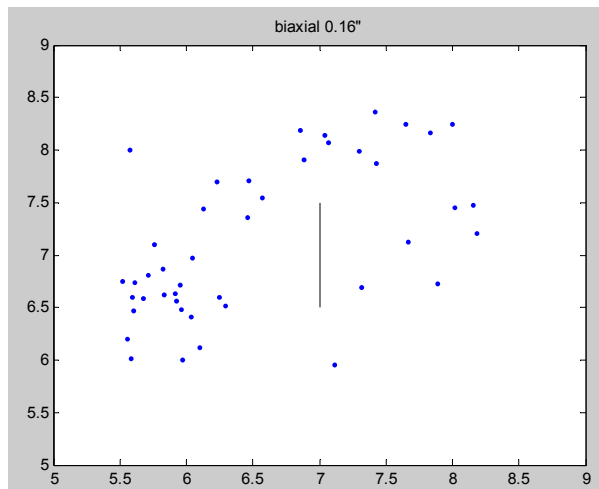
(b) AE data from uniaxial specimen with 0.16" deep defect



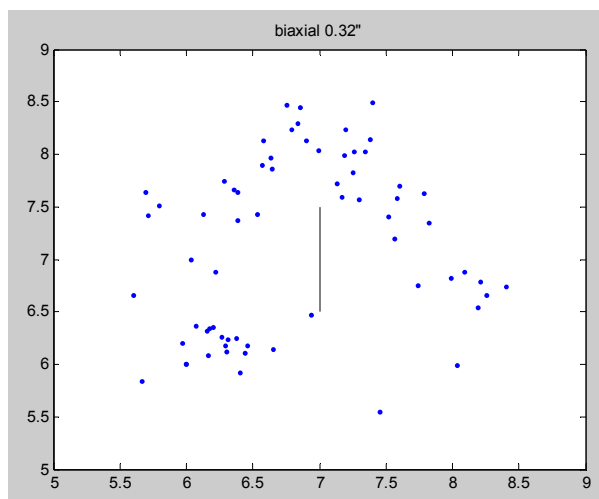
(c) AE data from uniaxial specimen with 0.32" deep defect



(d) AE data from biaxial specimen with 0.08” deep defect



(e) AE data from biaxial specimen with 0.16” deep defect



(f) AE data from biaxial specimen with 0.32” deep defect

Figure 4.15: Acoustic emission dataset.

4.2 Results

The results section will be segmented into the homogeneous data fusion section and the heterogeneous data fusion section. Each section will discuss the details behind the data fusion process and how the redundant and complementary information was extracted from the NDE inspection data. Training and testing sets will also be defined for each section followed by the resulting fused data with redundant and complementary information.

4.2.1 Definition of Redundant and Complementary Information

It is the goal of the RBF neural network to interpolate the redundant and complementary information as well as the intensity of the defect region. To perform this operation the neural network must be trained in the difference between redundant and complementary information. Therefore it is necessary to develop a definition that defines redundant and complementary information for multi-sensor NDE data in terms of the defect geometry. Figure 4.16 illustrates the definition of redundant and complementary information used in the exercise of the data fusion algorithms.

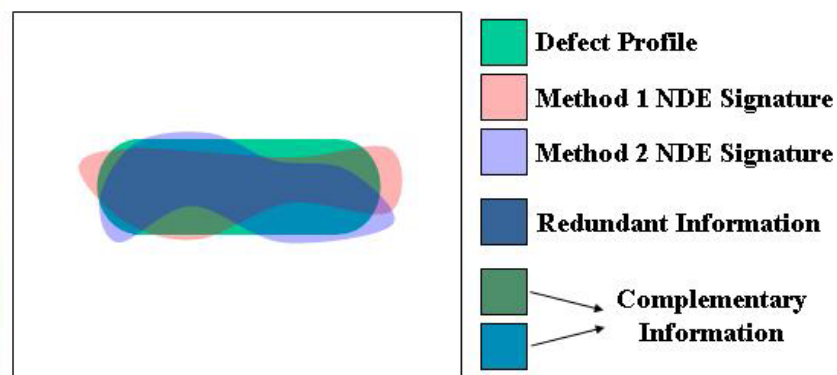


Figure 4.16: Redundant and complementary data definitions between two NDE signatures [13].

Pixel gray values are assigned corresponding to the depth of the defect at that location. Complementary information in two NDE images are defined as those distinct pixels in each of the NDE signatures that are present in the defect region, but are not shared between them. Redundant information in two NDE images are defined as those common pixels that are present in both NDE signatures and are also present in the defect region. During the implementation of the data fusion approach, discrete Cosine transforms (DCTs) of the gray level images have been obtained and the 80 highest spectral coefficients have been used as feature vectors that are input to the RBF neural network.

4.2.2 Homogeneous Training and Test Datasets

The homogeneous data fusion is performed on the NDE inspection data collected from the ultrasound, MFL, and thermal imaging systems. In each test platform the twelve specimens have been scanned twice on two separate instances to provide additional data for training and testing the neural network. The data fusion technique is performed on three different instances between: UT & MFL, Thermal & UT, and MFL & Thermal. Each test sequence includes three separate trials that vary the training and test data inputted into the network. The training and test data segmentation for each trial is listed below in Tables 4.3 through 4.5.

Table 4.3: Trial 1 training and test dataset.

Specimen #	Plate thickness (in)	Indication	Defect Depth (in)
00a	0.5	None	N/A
03a	0.5	Pitting	0.0945
02a	0.5	Pitting	0.198
01a	0.5	Pitting	0.3005
10a	0.375	None	N/A
13a	0.375	Pitting	0.1105
12a	0.375	Pitting	0.199
11a	0.375	Pitting	0.298
20a	0.3125	None	N/A

23a	0.3125	Pitting	0.0995
22a	0.3125	Pitting	0.1955
21a	0.3125	Pitting	0.303
00b	0.5	None	N/A
03b	0.5	Pitting	0.0945
02b	0.5	Pitting	0.198
01b	0.5	Pitting	0.3005
10b	0.375	None	N/A
13b	0.375	Pitting	0.1105
12b	0.375	Pitting	0.199
11b	0.375	Pitting	0.298
20b	0.3125	None	N/A
23b	0.3125	Pitting	0.0995
22b	0.3125	Pitting	0.1955
21b	0.3125	Pitting	0.303

 Training data  Test data

Table 4.4: Trial 2 training and test dataset

Specimen #	Plate thickness (in)	Indication	Defect Depth (in)
00a	0.5	None	N/A
03a	0.5	Pitting	0.0945
02a	0.5	Pitting	0.198
01a	0.5	Pitting	0.3005
10a	0.375	None	N/A
13a	0.375	Pitting	0.1105
12a	0.375	Pitting	0.199
11a	0.375	Pitting	0.298
20a	0.3125	None	N/A
23a	0.3125	Pitting	0.0995
22a	0.3125	Pitting	0.1955
21a	0.3125	Pitting	0.303
00b	0.5	None	N/A
03b	0.5	Pitting	0.0945
02b	0.5	Pitting	0.198
01b	0.5	Pitting	0.3005
10b	0.375	None	N/A
13b	0.375	Pitting	0.1105
12b	0.375	Pitting	0.199
11b	0.375	Pitting	0.298
20b	0.3125	None	N/A
23b	0.3125	Pitting	0.0995
22b	0.3125	Pitting	0.1955
21b	0.3125	Pitting	0.303

 Training data  Test data

Table 4.5: Trial 3 training and test dataset

Specimen #	Plate thickness (in)	Indication	Defect Depth (in)
00a	0.5	None	N/A
03a	0.5	Pitting	0.0945
02a	0.5	Pitting	0.198
01a	0.5	Pitting	0.3005
10a	0.375	None	N/A
13a	0.375	Pitting	0.1105
12a	0.375	Pitting	0.199
11a	0.375	Pitting	0.298
20a	0.3125	None	N/A
23a	0.3125	Pitting	0.0995
22a	0.3125	Pitting	0.1955
21a	0.3125	Pitting	0.303
00b	0.5	None	N/A
03b	0.5	Pitting	0.0945
02b	0.5	Pitting	0.198
01b	0.5	Pitting	0.3005
10b	0.375	None	N/A
13b	0.375	Pitting	0.1105
12b	0.375	Pitting	0.199
11b	0.375	Pitting	0.298
20b	0.3125	None	N/A
23b	0.3125	Pitting	0.0995
22b	0.3125	Pitting	0.1955
21b	0.3125	Pitting	0.303

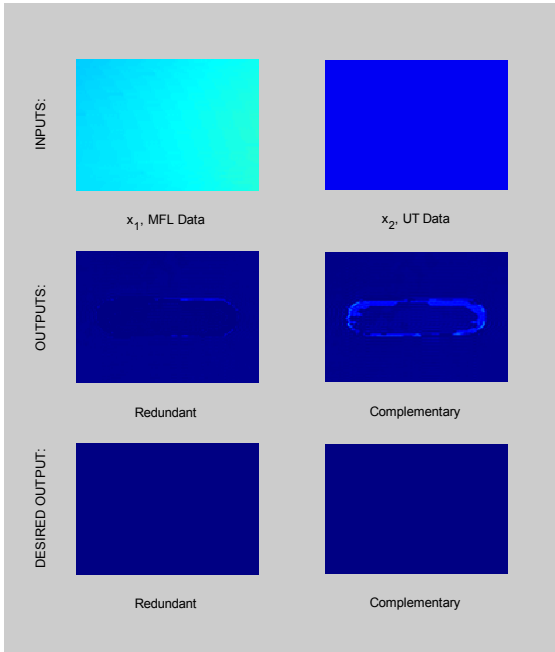
 Training data
  Test data

The results in Figures 4.17 through 4.25 represent the three trials for each of the three combinations of NDE data. Included in each trial are the training and test data outputs of the neural network seen in the subplots (a) through (x). A border surrounding the subplot figure designates the test data outputs. The subplots (a) through (x) represent the output for the specimens listed in the order of the trial tables, with the specimens designated for testing shown last. For example subplot (a) represents the output from Specimen 00a, while subplot (b) represents Specimen 03a, and so on. In certain

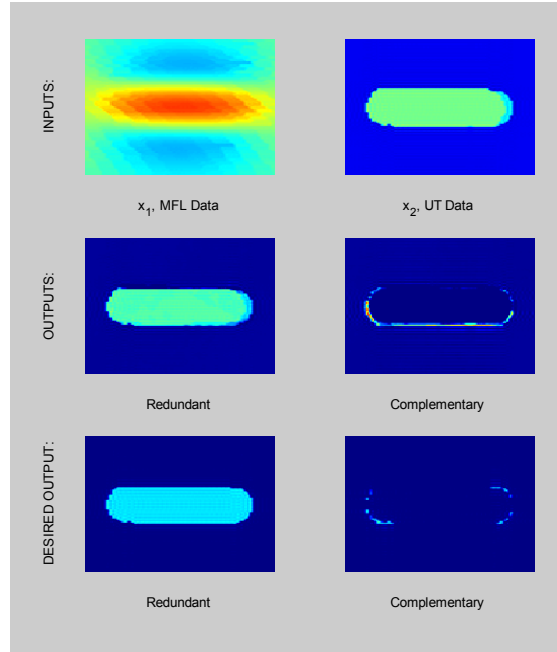
combinations, outlying training data instance were excluded from training and testing causing there to be fewer subplots in those cases. Each subplot figure is segmented into six images. The first row includes the input data from each of the NDE testing modalities. The second row represents the redundant and complimentary output predicted by the algorithm while the third row shows the desired redundant the complementary output.

4.2.2.1 Ultrasound & MFL Data Fusion Results

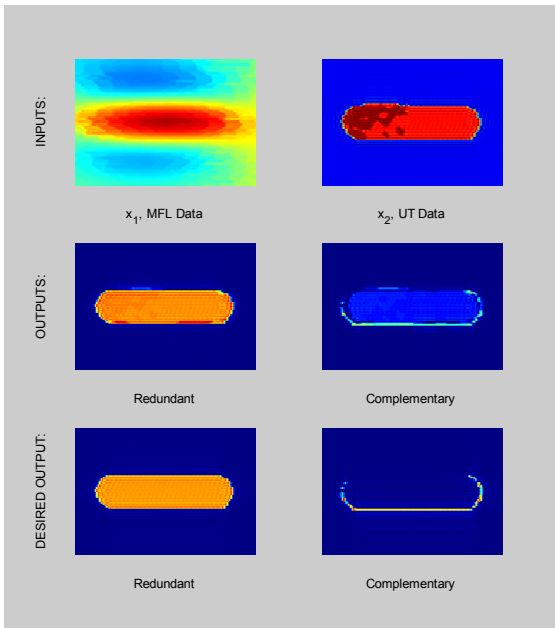
Trial 1: UT & MFL Results



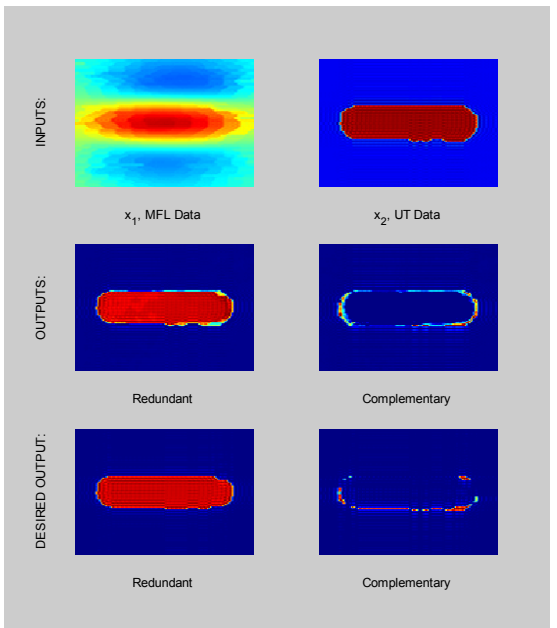
(a) Specimen 00a



(b) Specimen 03a

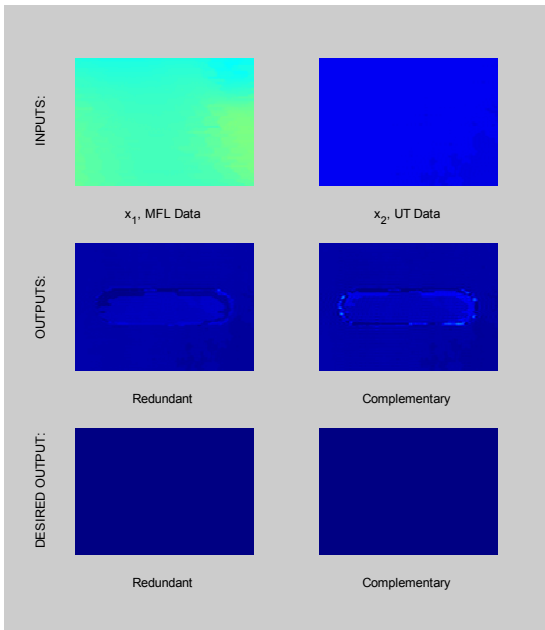


(c) Specimen 02a

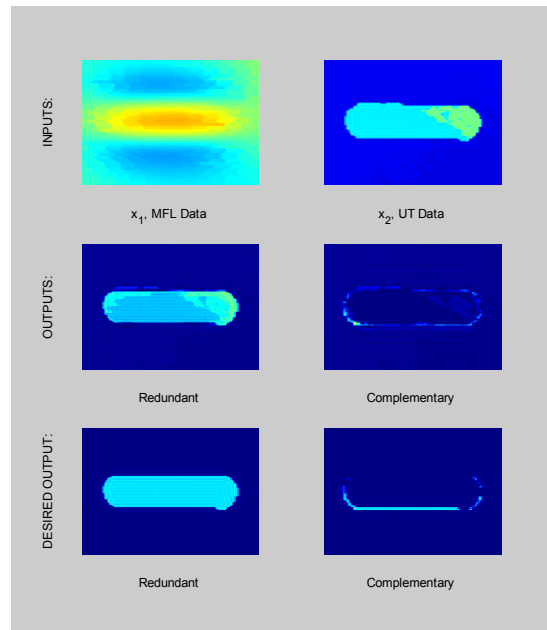


(d) Specimen 01a

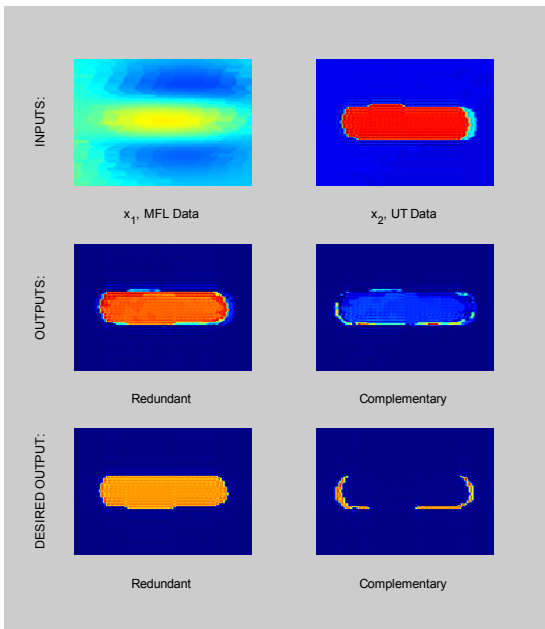
Trial 1: UT & MFL Results (cont.)



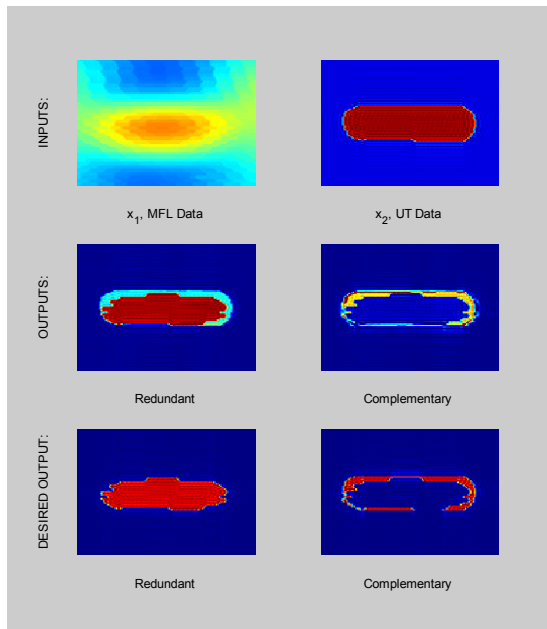
(e) Specimen 10a



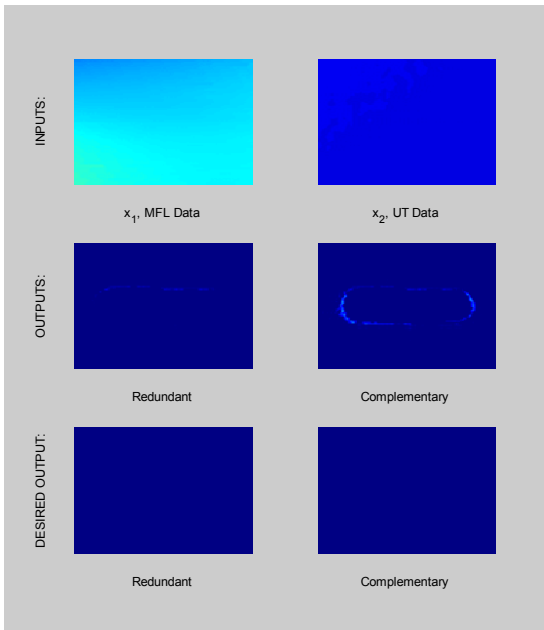
(f) Specimen 13a



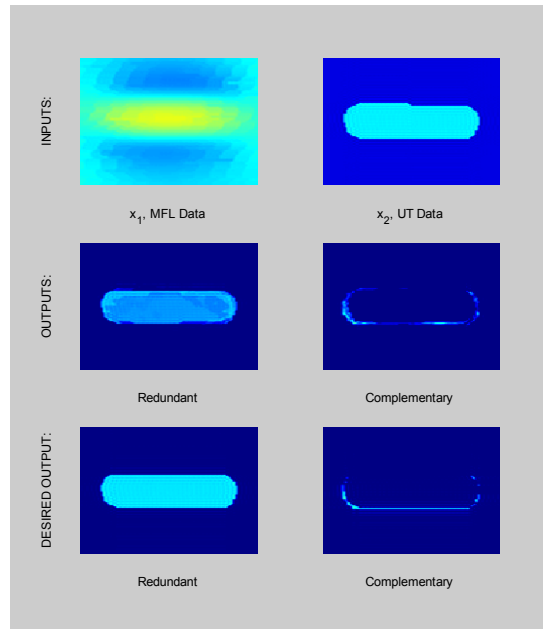
(g) Specimen 12a



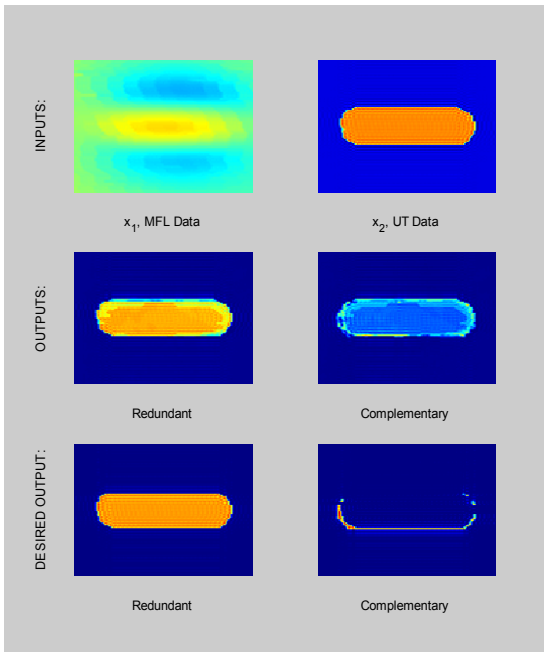
(h) Specimen 11a



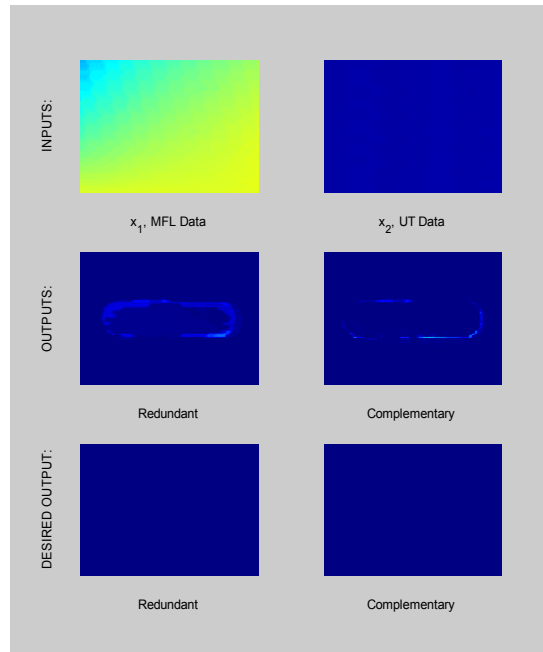
(i) Specimen 20a



(j) Specimen 23a

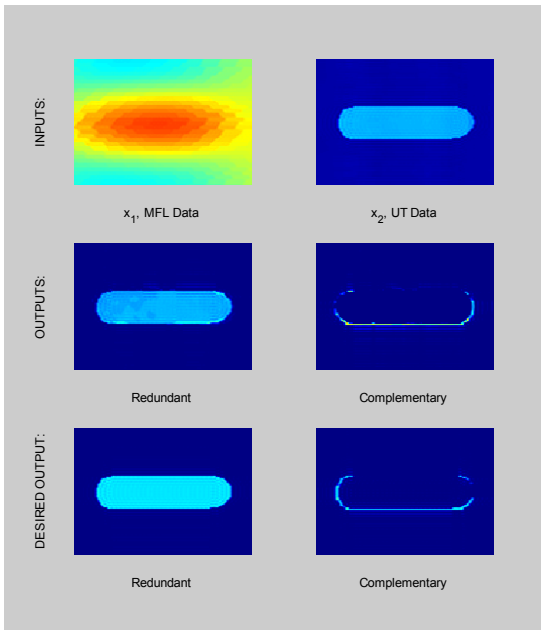


(k) Specimen 22a

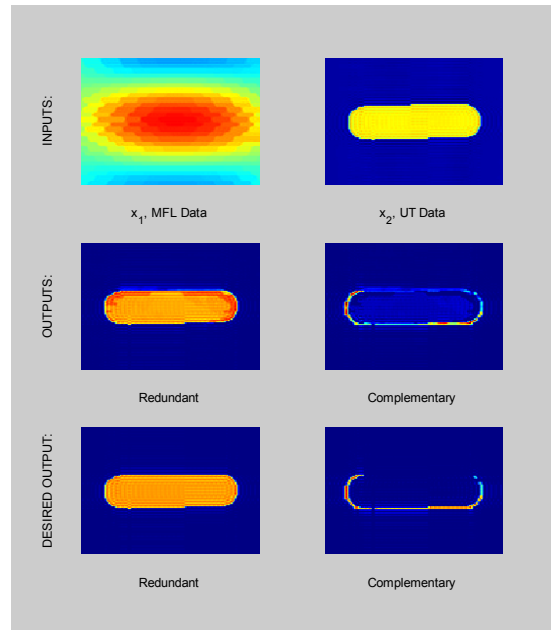


(l) Specimen 00b

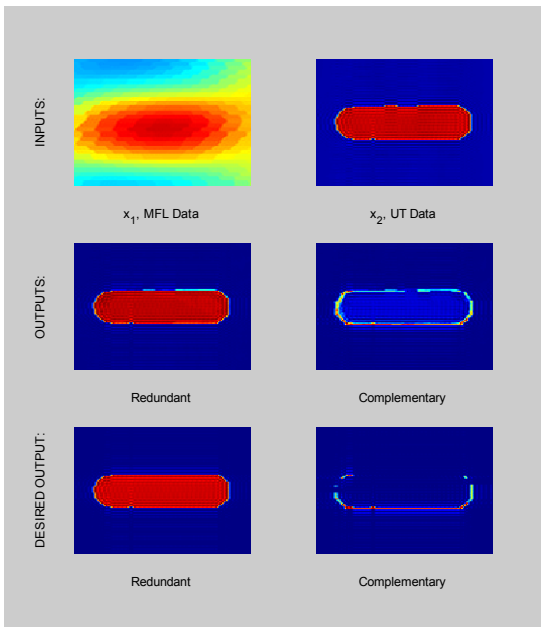
Trial 1: UT & MFL Results (cont.)



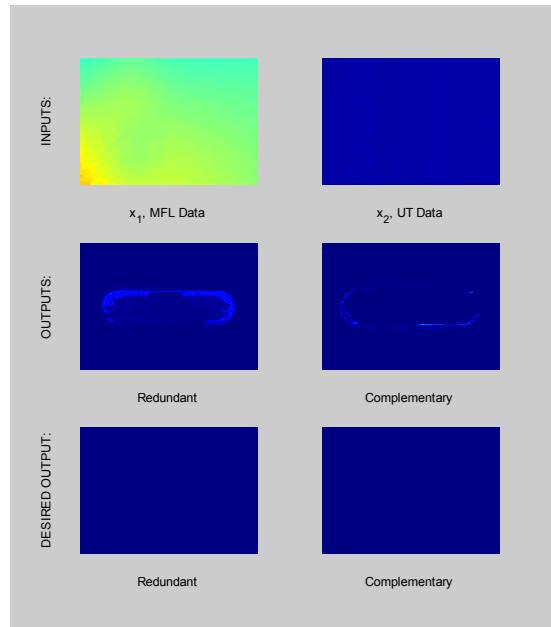
(m) Specimen 03b



(n) Specimen 02b

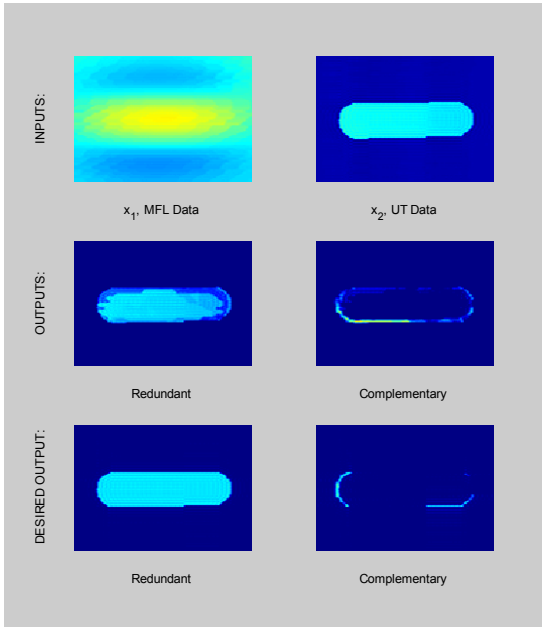


(o) Specimen 01b

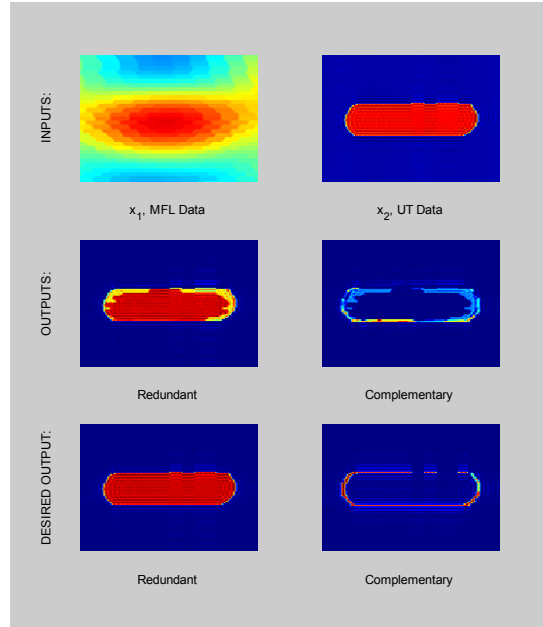


(p) Specimen 10b

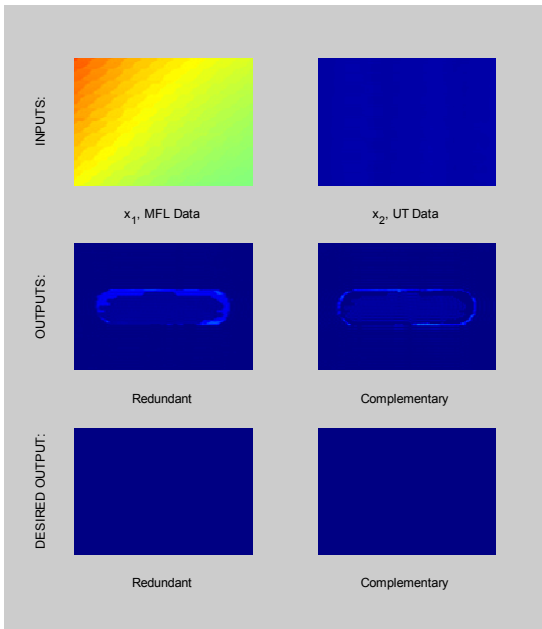
Trial 1: UT & MFL Results (cont.)



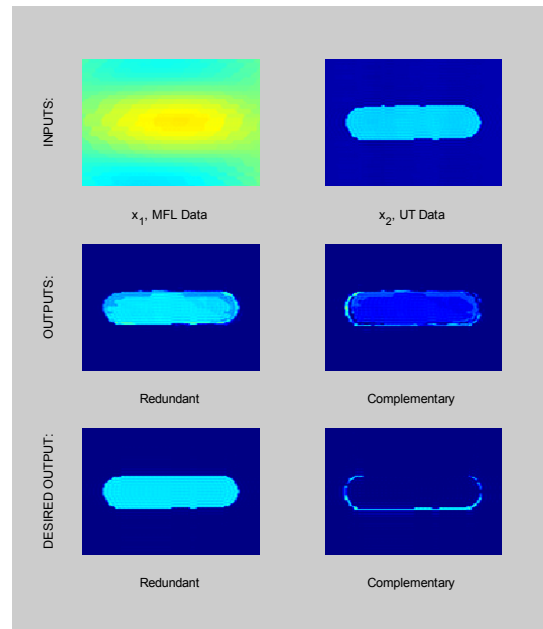
(q) Specimen 13b



(r) Specimen 11b

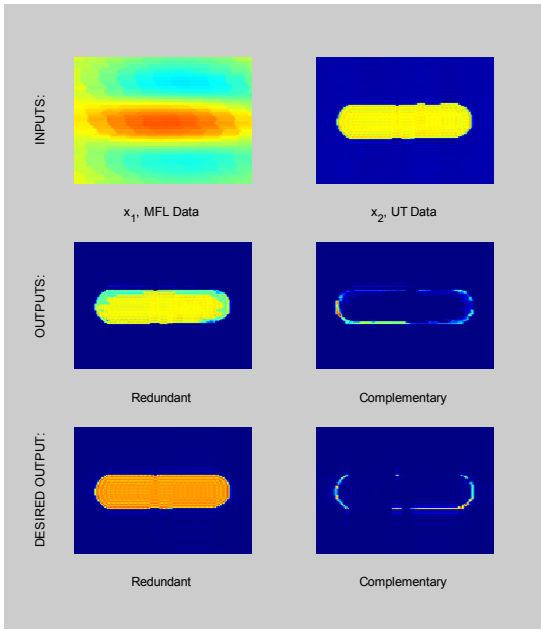


(s) Specimen 20b

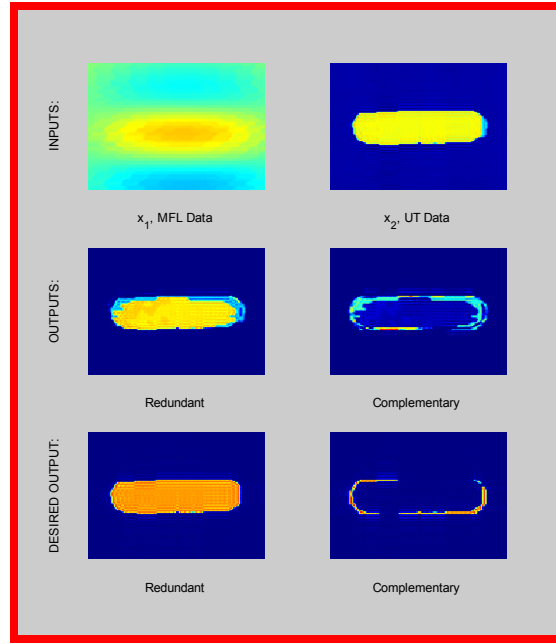


(t) Specimen 23b

Trial 1: UT & MFL Results (cont.)



(u) Specimen 22b

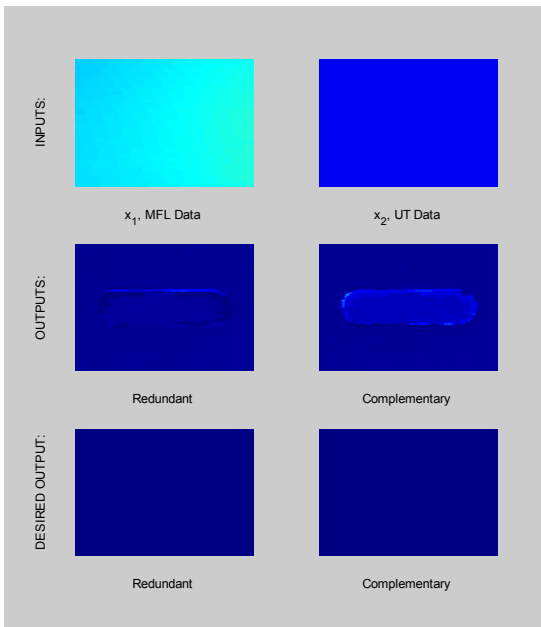


(v) Specimen 01a

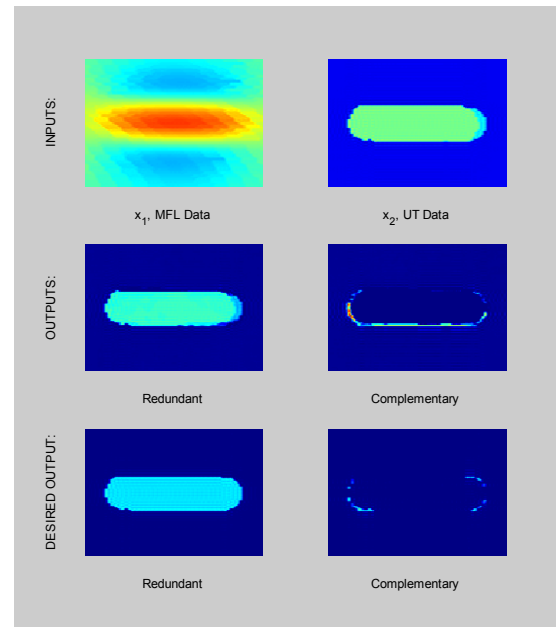
Figure 4.17: UT & MFL Combination Trial 1

Training Data: (a) – (u); Test Data: (v)

Trial 2: UT & MFL Results

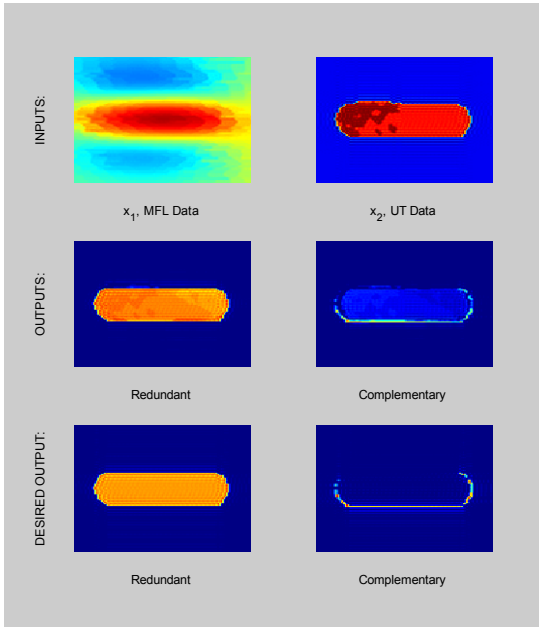


(a) Specimen 00a

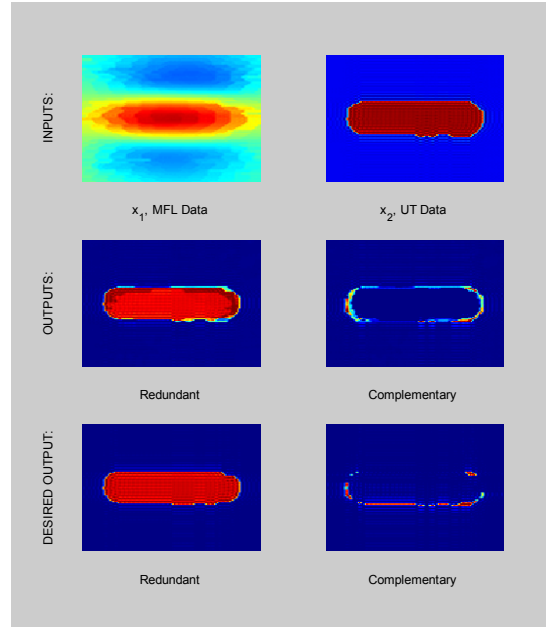


(b) Specimen 03a

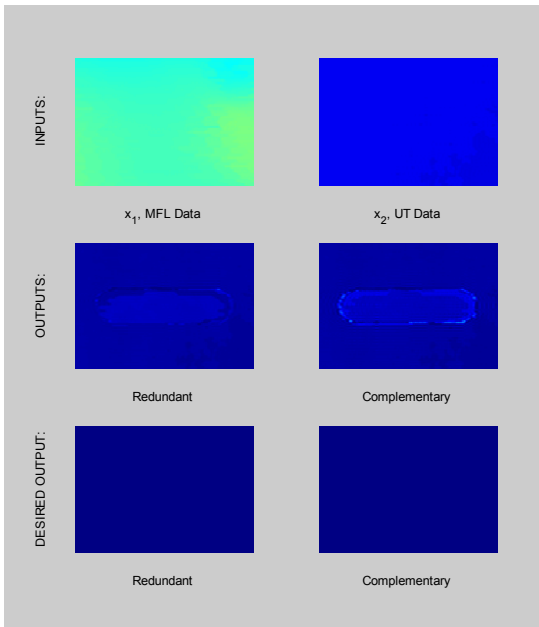
Trial 2: UT & MFL Results (cont.)



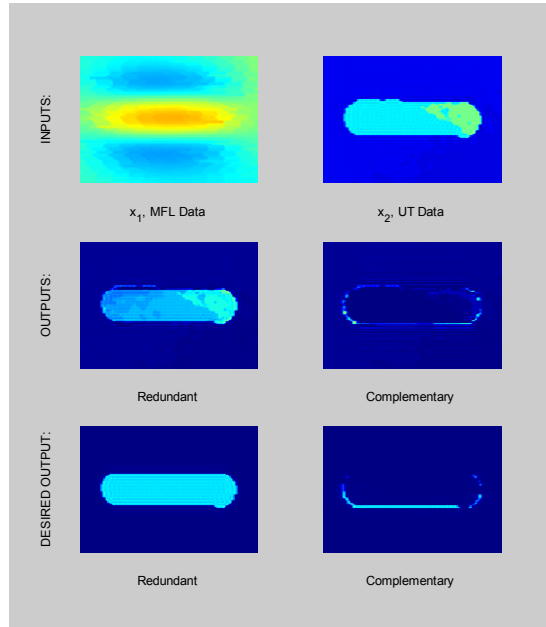
(c) Specimen 02a



(d) Specimen 01a

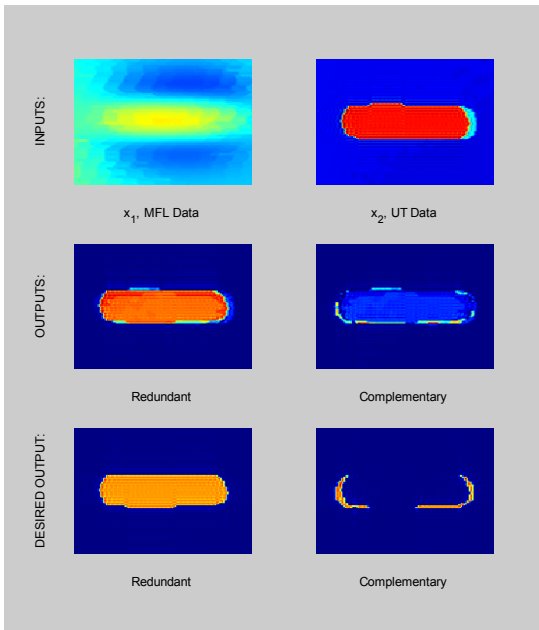


(e) Specimen 10a

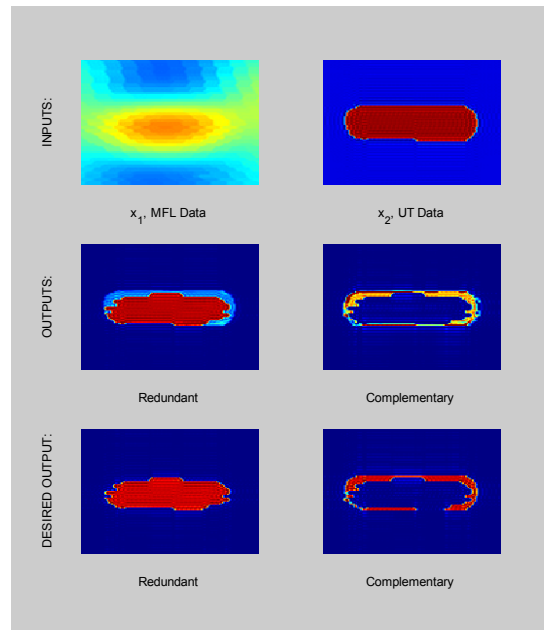


(f) Specimen 13a

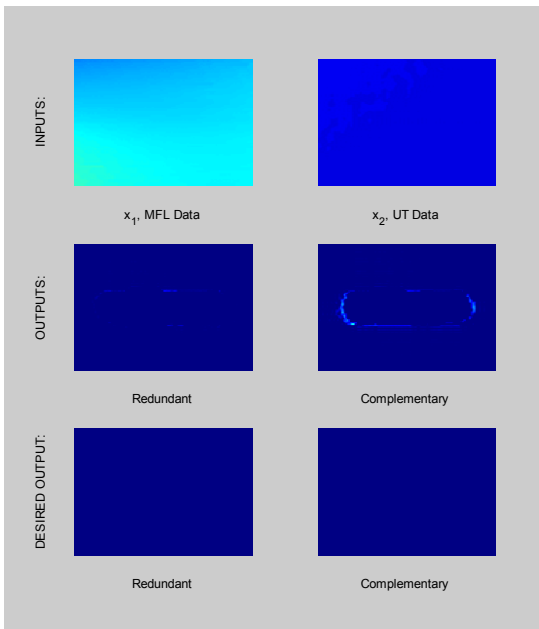
Trial 2: UT & MFL Results (cont.)



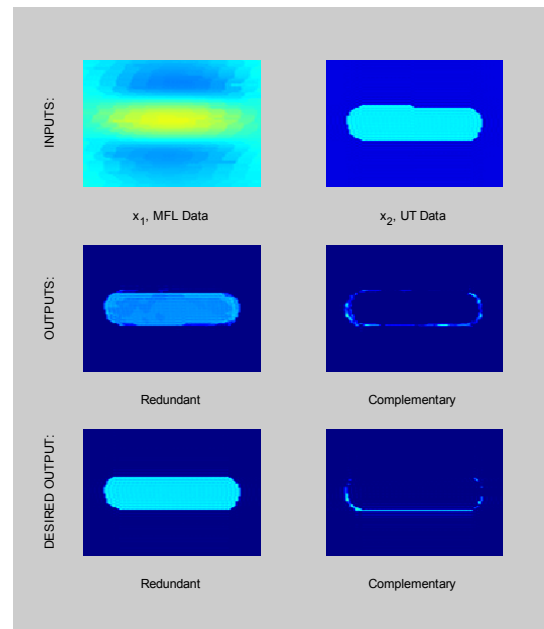
(g) Specimen 12a



(h) Specimen 11a

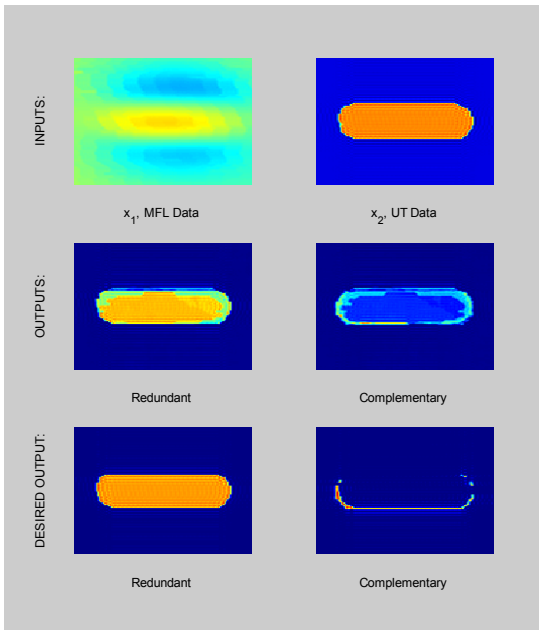


(i) Specimen 20a

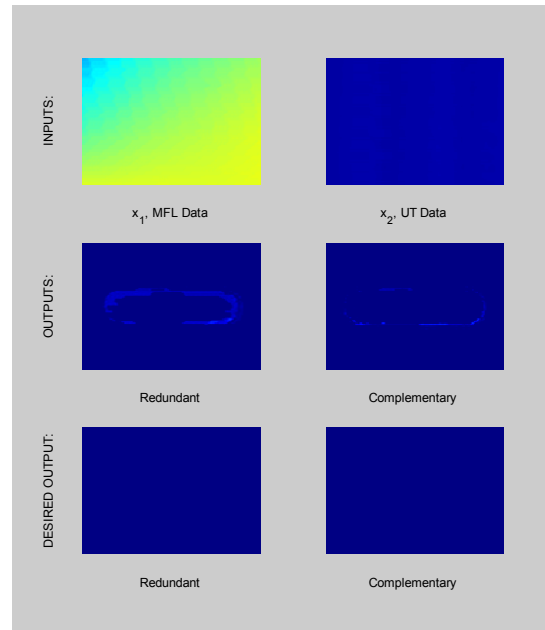


(j) Specimen 23a

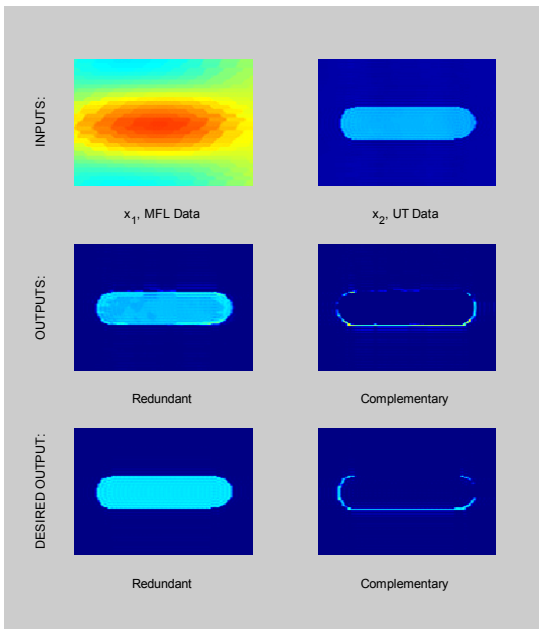
Trial 2: UT & MFL Results (cont.)



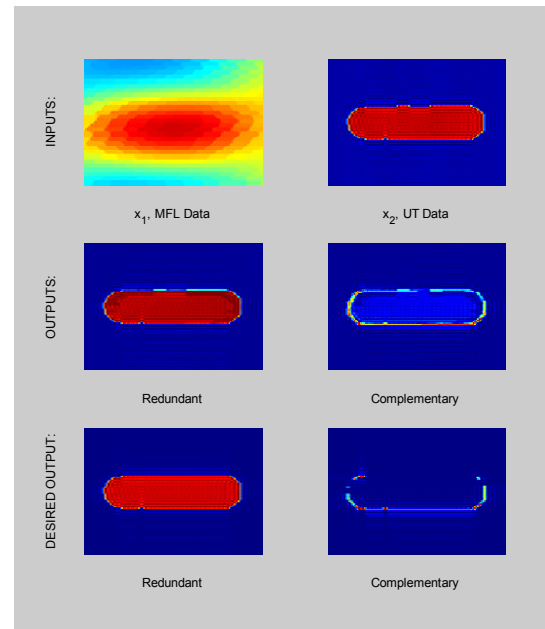
(k) Specimen 22a



(l) Specimen 00b

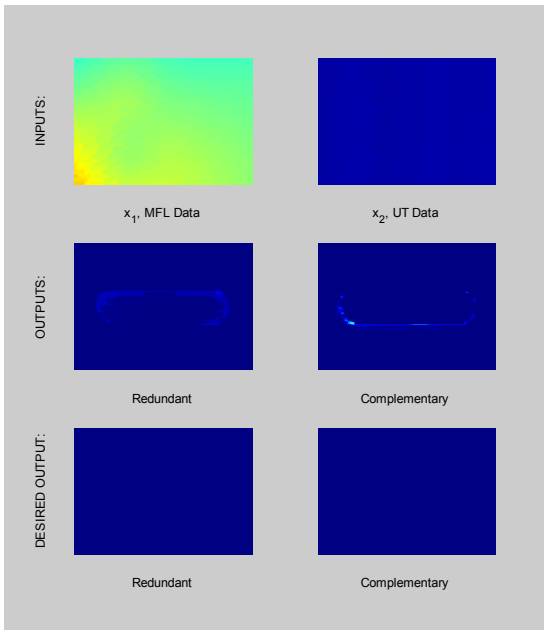


(m) Specimen 03b

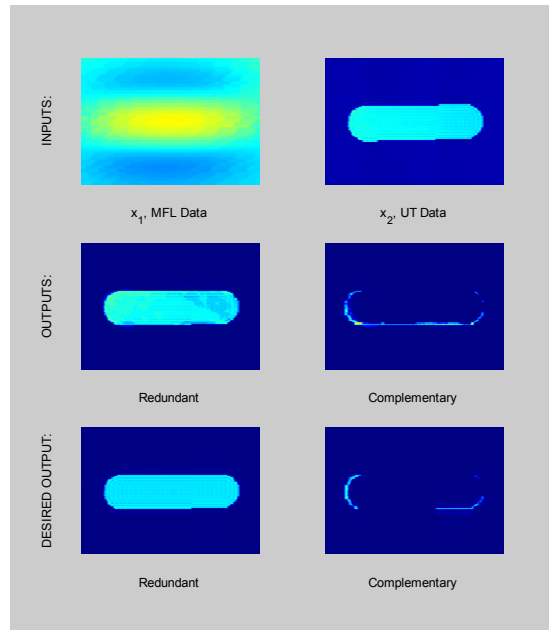


(n) Specimen 01b

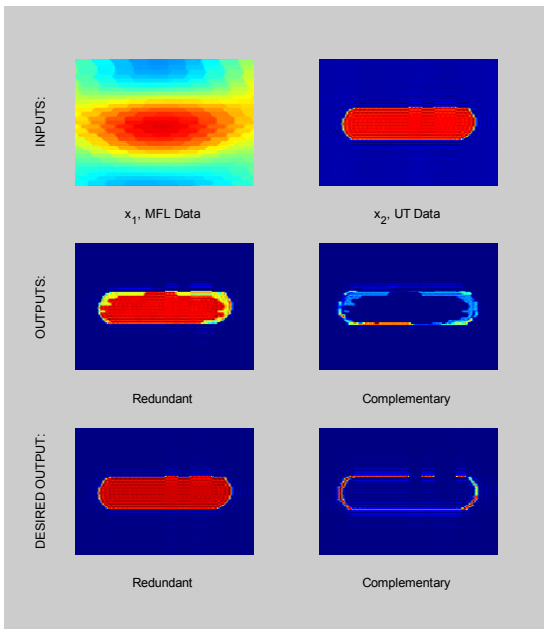
Trial 2: UT & MFL Results (cont.)



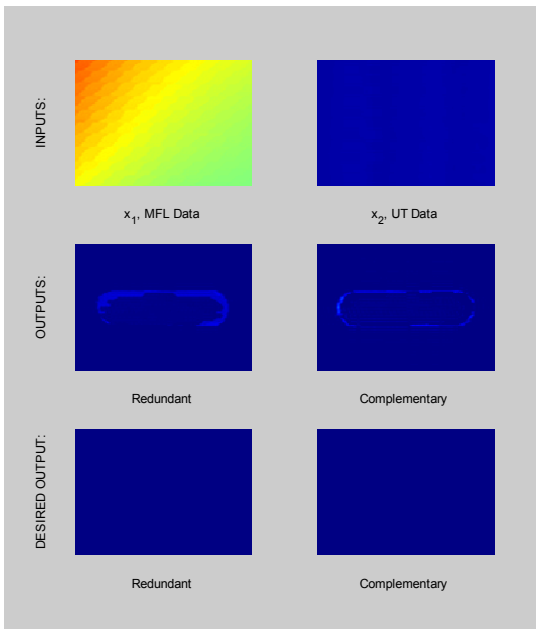
(o) Specimen 10b



(p) Specimen 13b

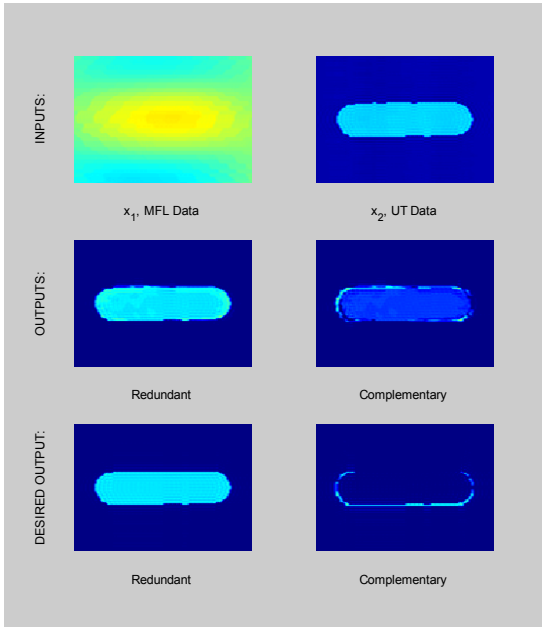


(q) Specimen 11b

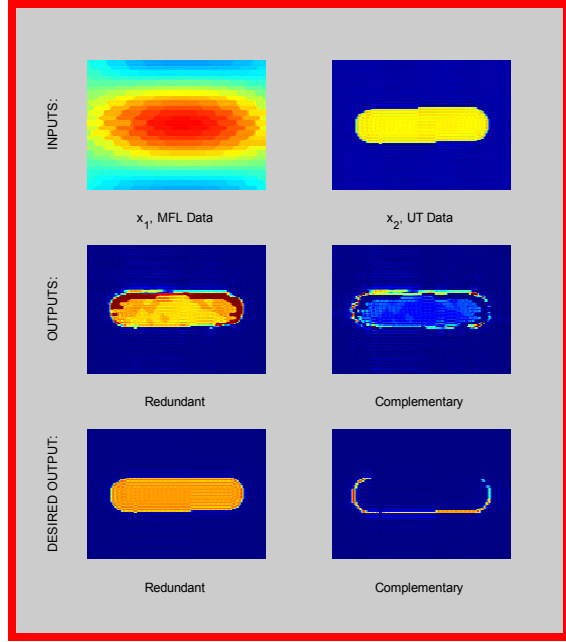


(r) Specimen 20b

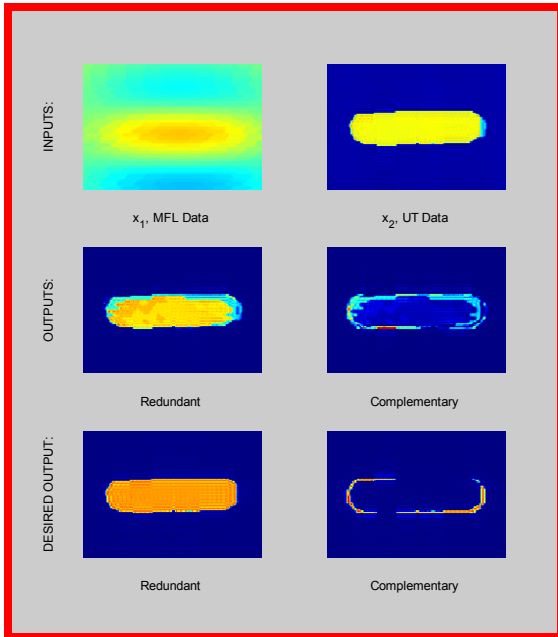
Trial 2: UT & MFL Results (cont.)



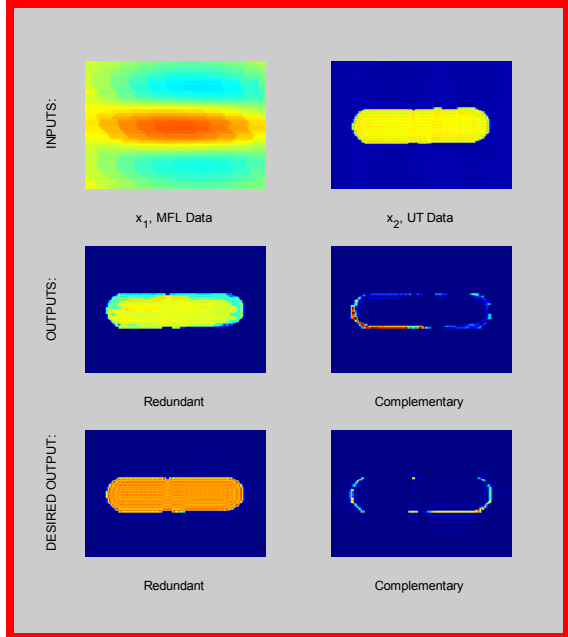
(s) Specimen 23b



(t) Specimen 02b



(u) Specimen 12b

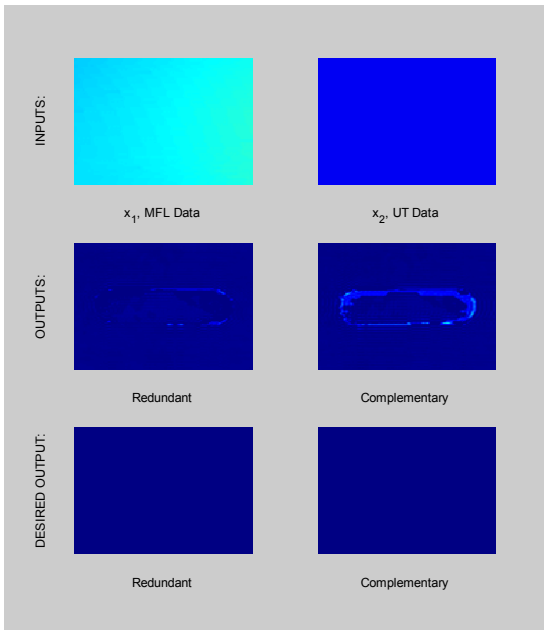


(v) Specimen 22b

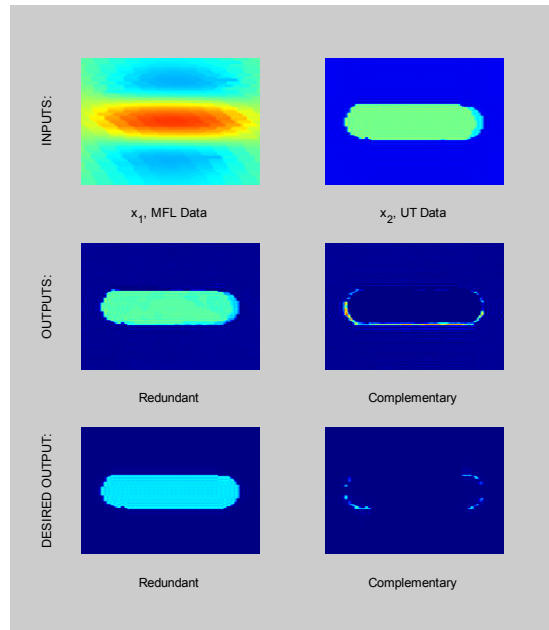
Figure 4.18: UT & MFL combination Trial 2.

Training Data: (a) – (s); Test Data: (t), (u), (v)

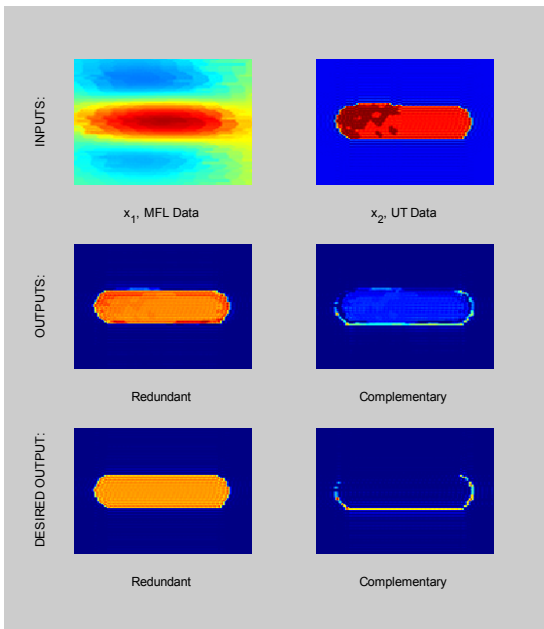
Trial 3: UT & MFL Results



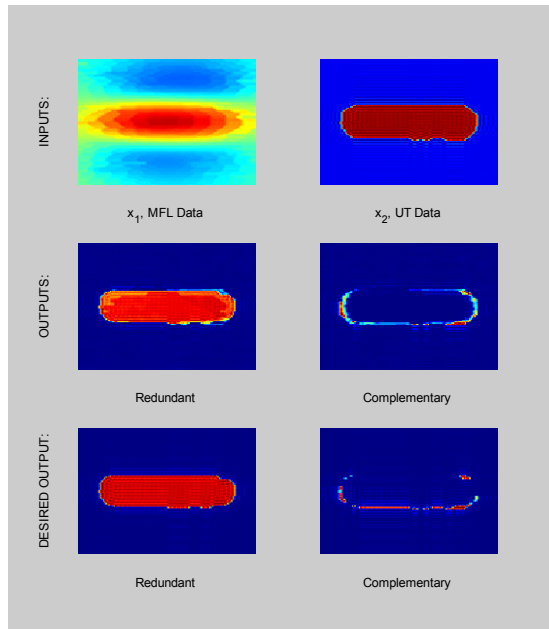
(a) Specimen 00a



(b) Specimen 03a

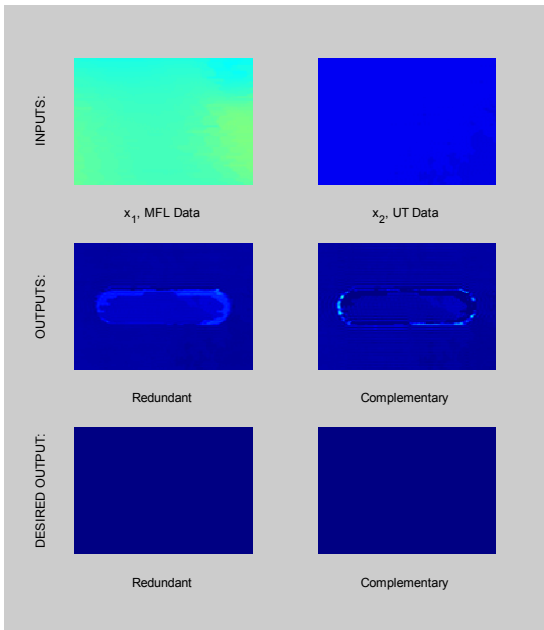


(c) Specimen 02a

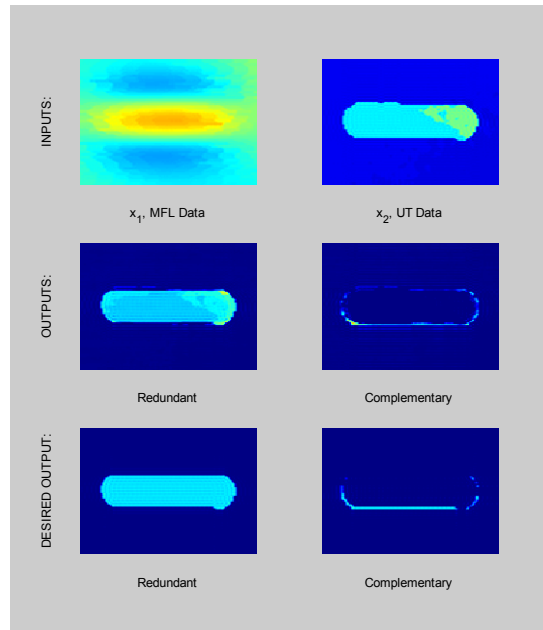


(d) Specimen 01a

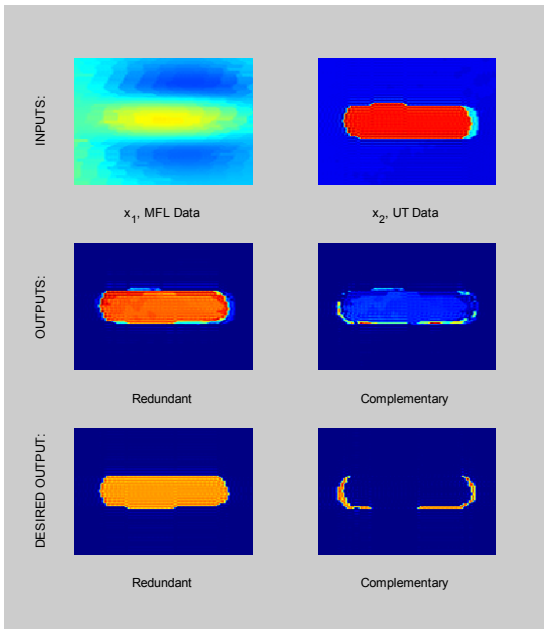
Trial 3: UT & MFL Results (cont.)



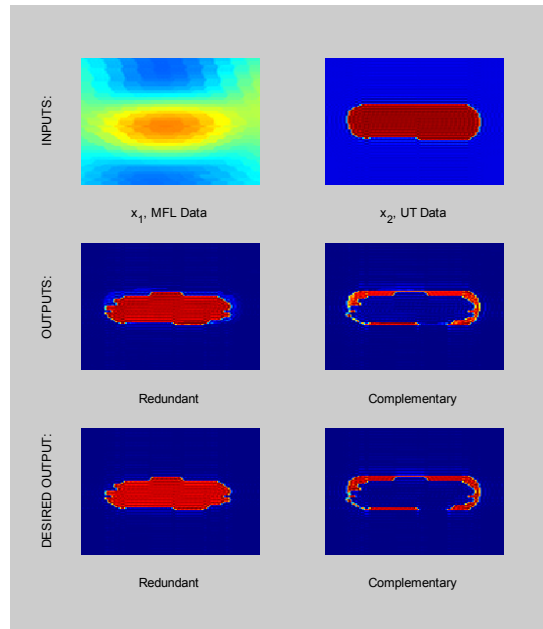
(e) Specimen 10a



(f) Specimen 13a

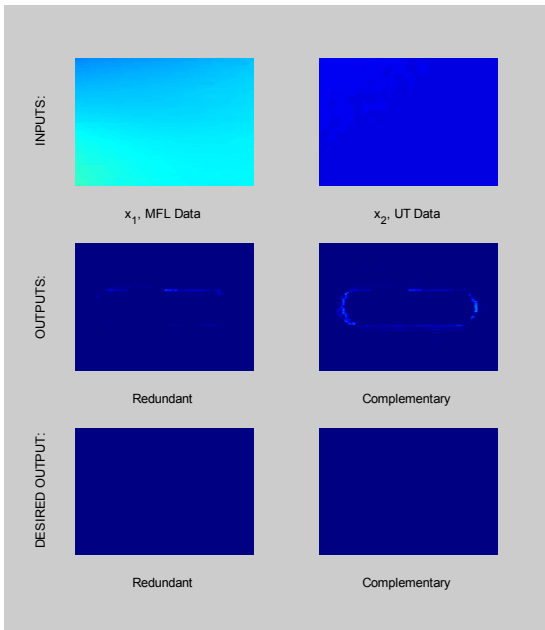


(g) Specimen 12a

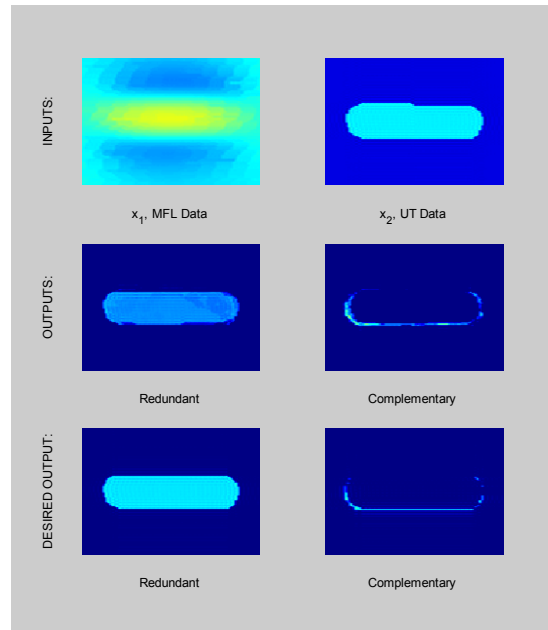


(h) Specimen 11a

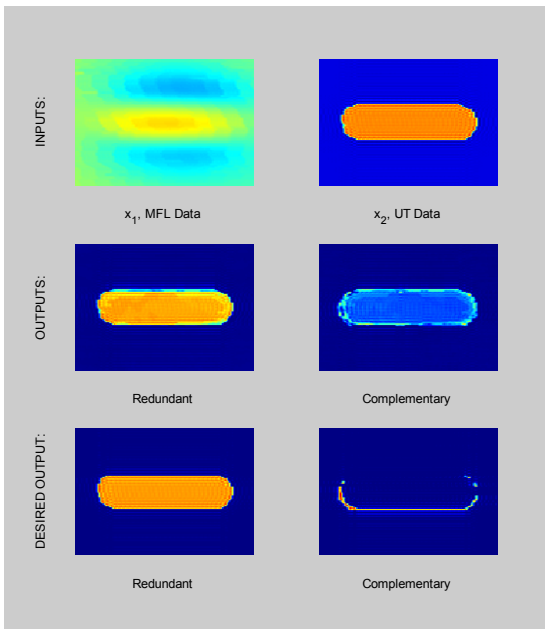
Trial 3: UT & MFL Results (cont.)



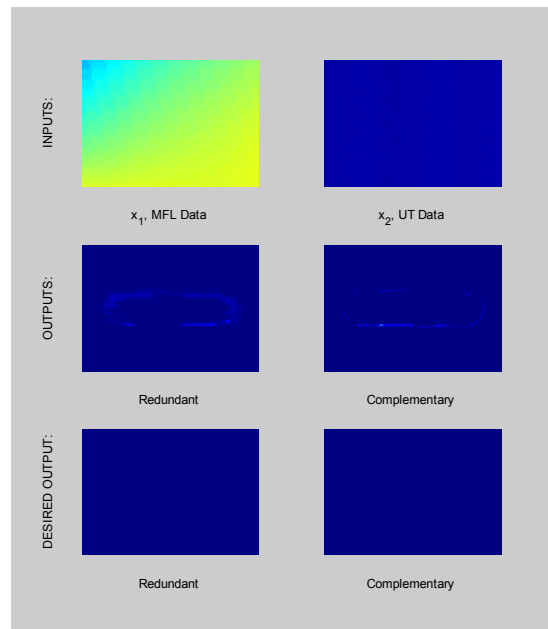
(i) Specimen 20a



(j) Specimen 23a

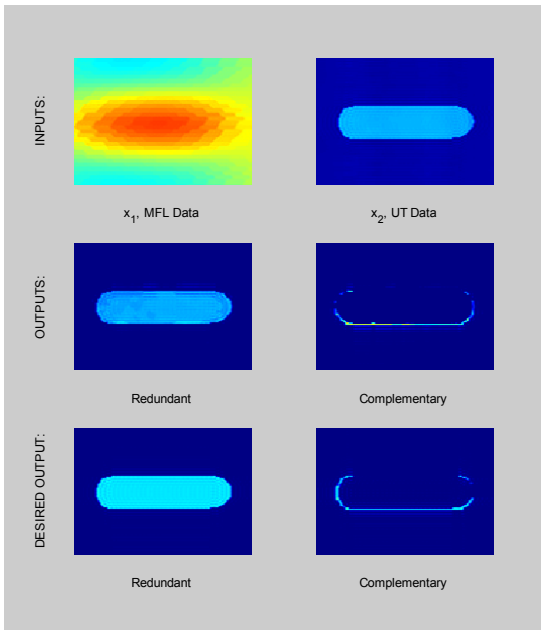


(k) Specimen 22a

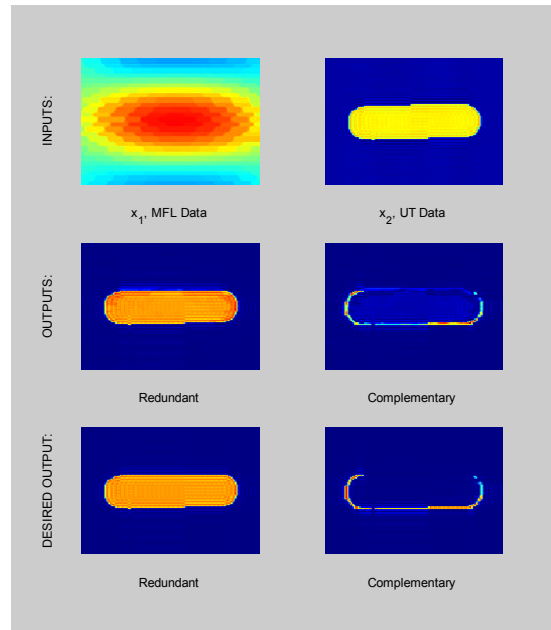


(l) Specimen 00b

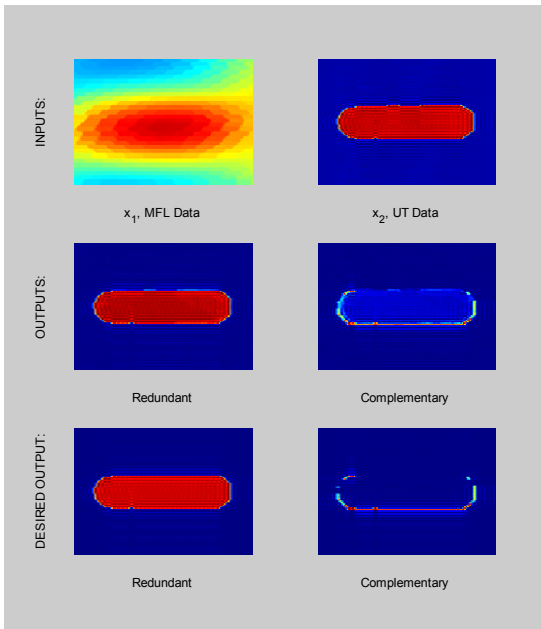
Trial 3: UT & MFL Results (cont.)



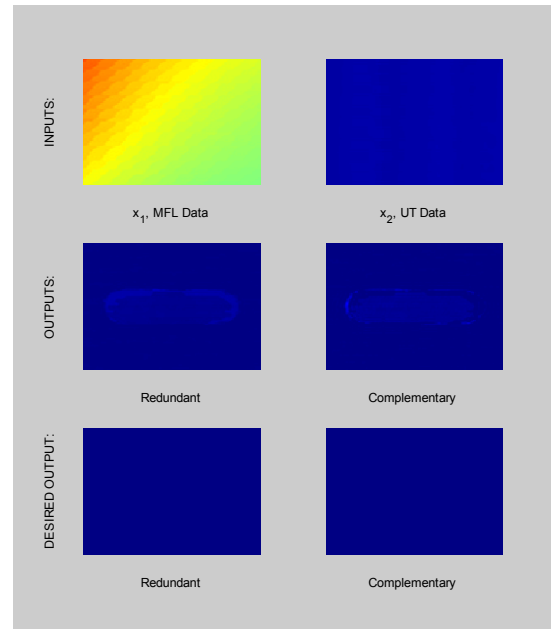
(m) Specimen 03b



(n) Specimen 02b

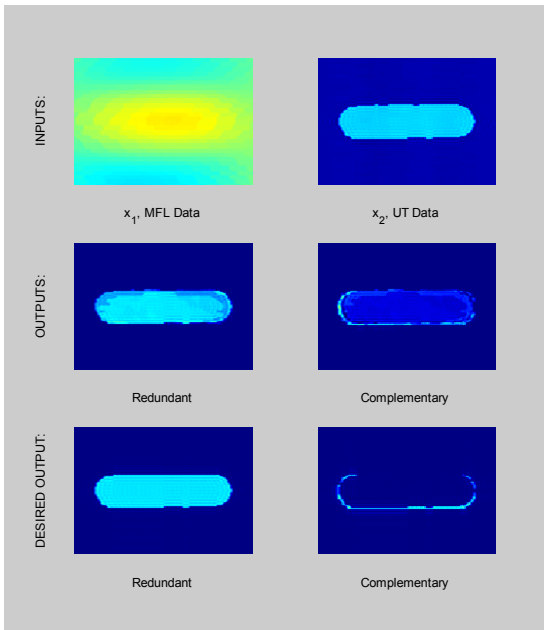


(o) Specimen 01b

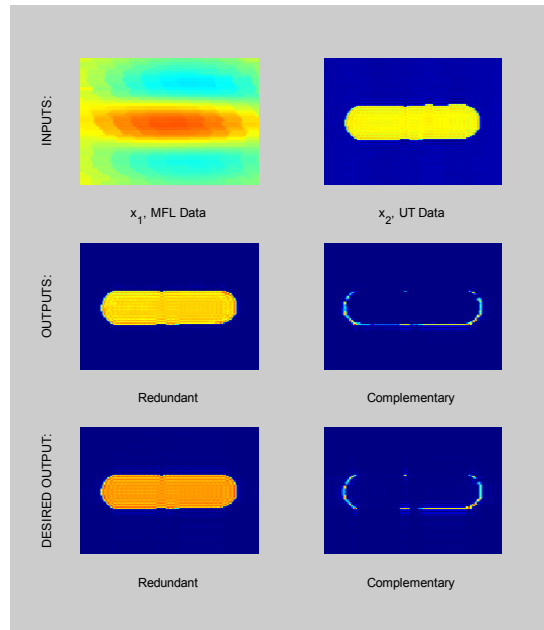


(p) Specimen 20b

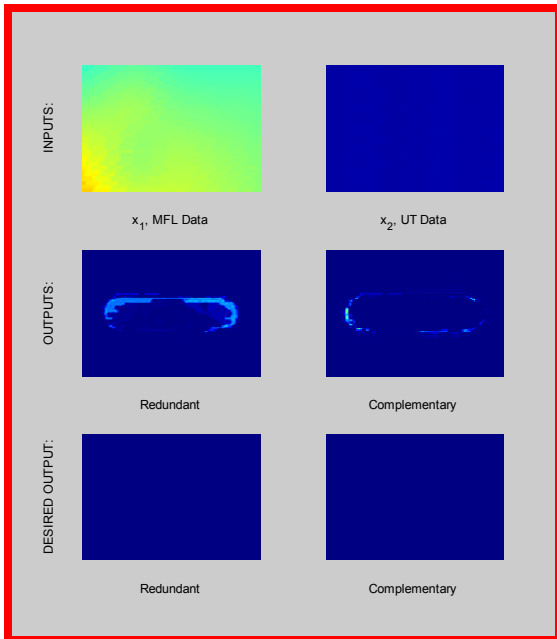
Trial 3: UT & MFL Results (cont.)



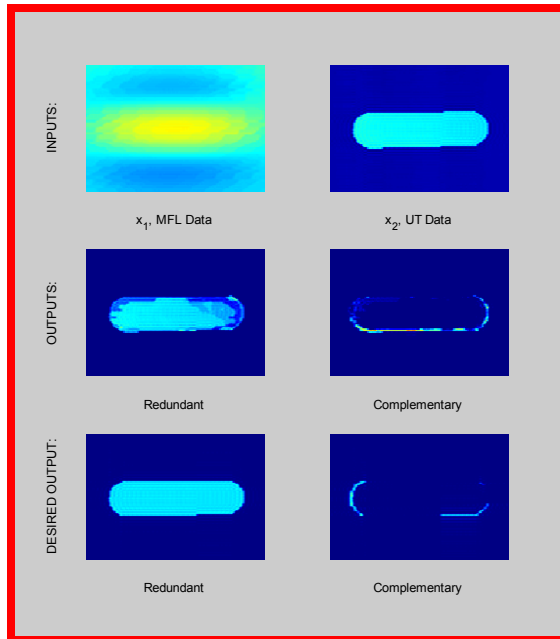
(q) Specimen 23b



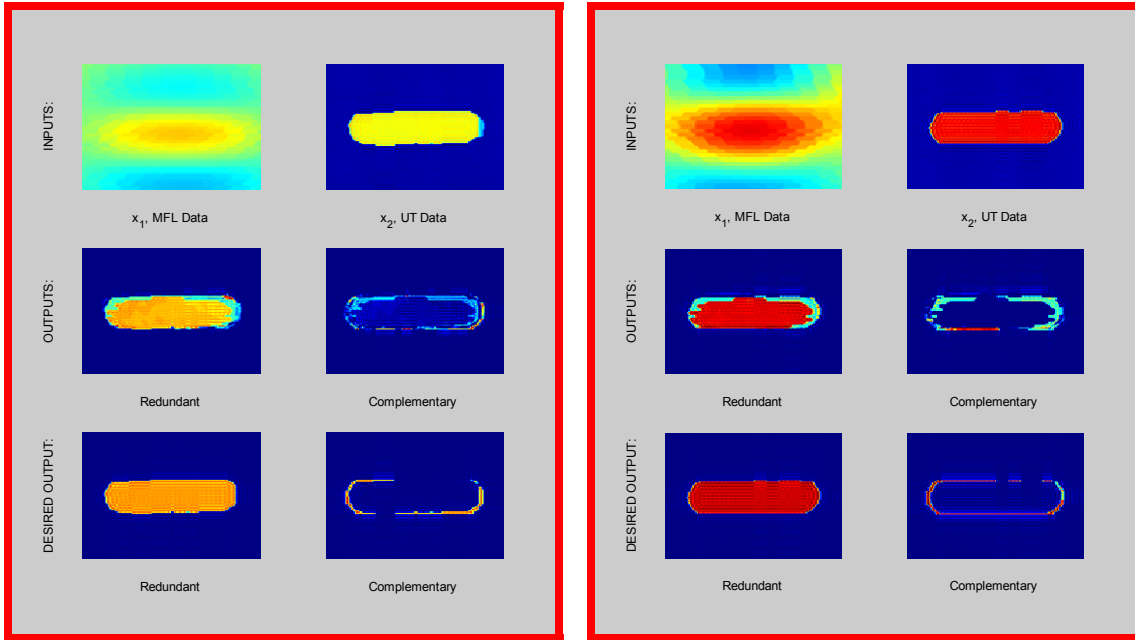
(r) Specimen 22b



(s) Specimen 10b



(t) Specimen 13b



(u) Specimen 12b

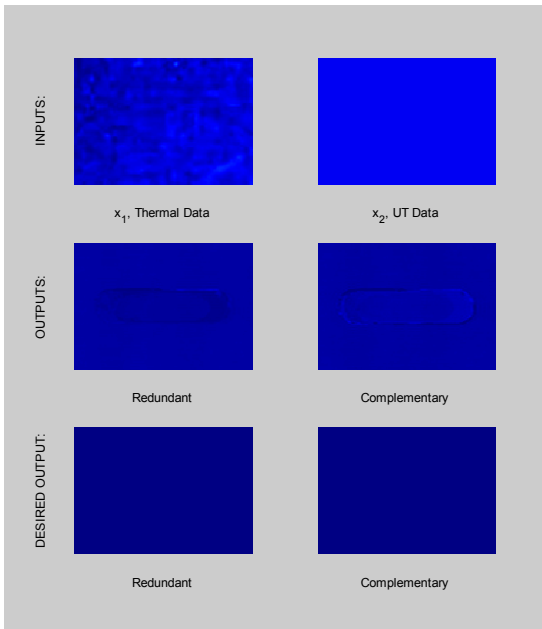
(v) Specimen 11b

Figure 4.19: UT & MFL combination Trial 3.

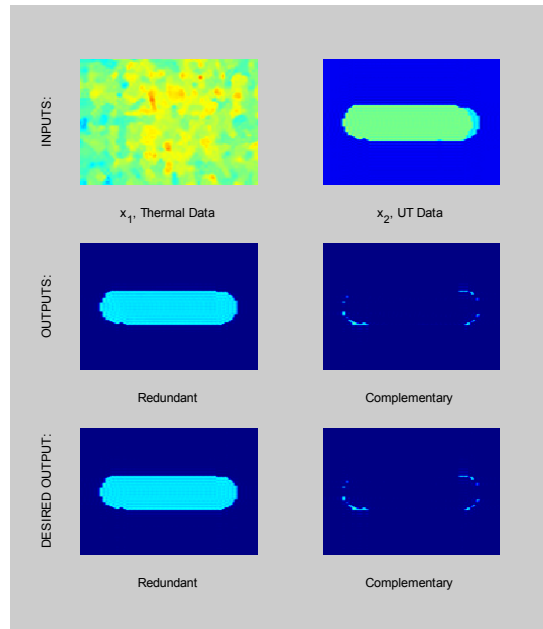
Training Data: (a) – (r); Test Data: (s), (t), (u), (v)

4.2.2.2 Thermal & UT Data Fusion Results

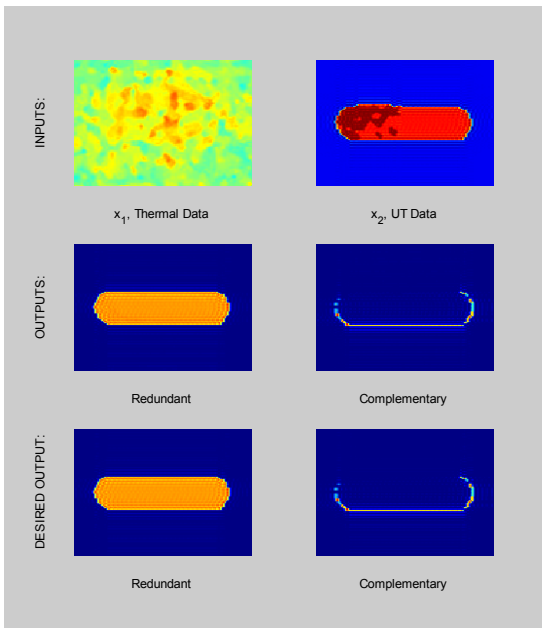
Trial 1: Thermal & UT Results



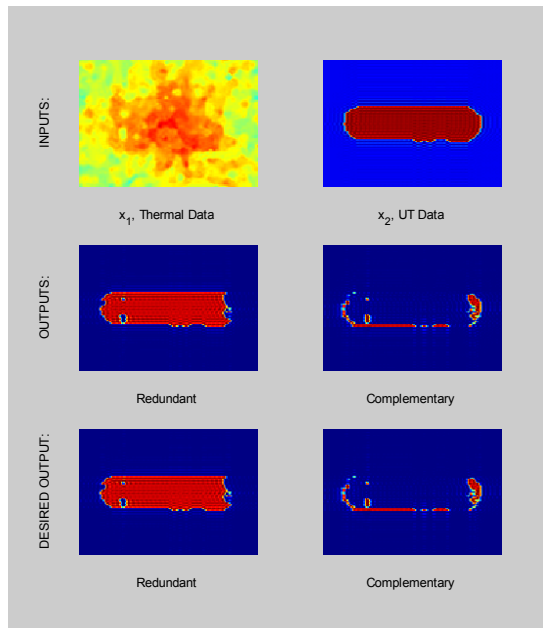
(a) Specimen 00a



(b) Specimen 03a

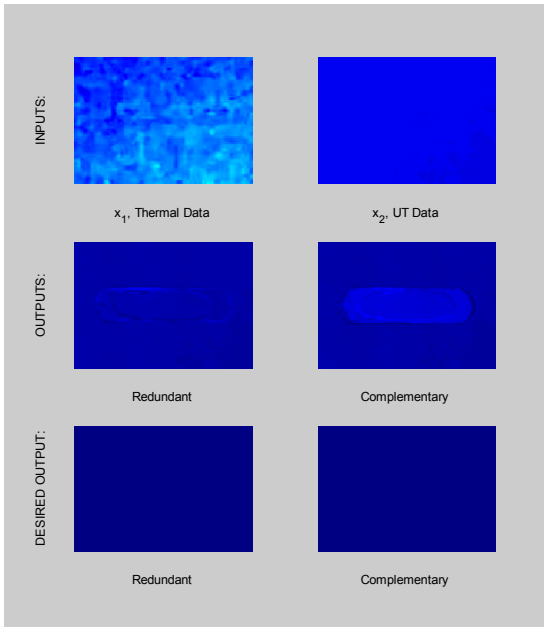


(c) Specimen 02a

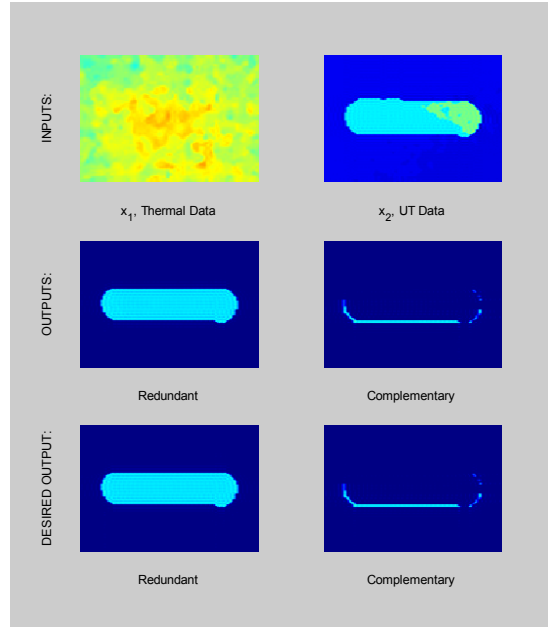


(d) Specimen 01a

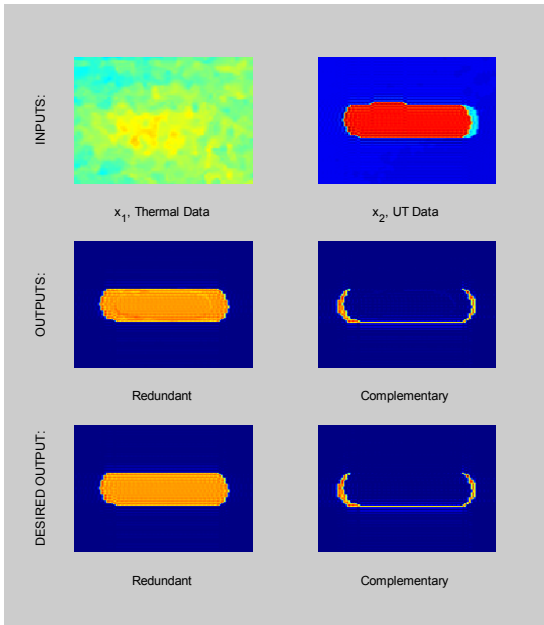
Trial 1: Thermal & UT Results (cont.)



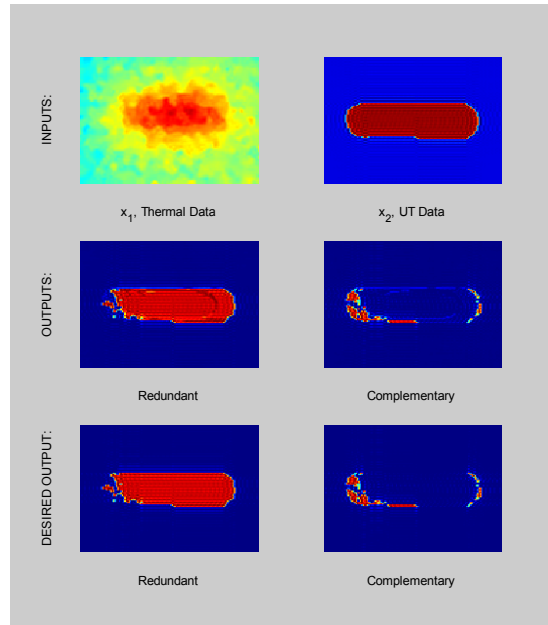
(e) Specimen 10a



(f) Specimen 13a

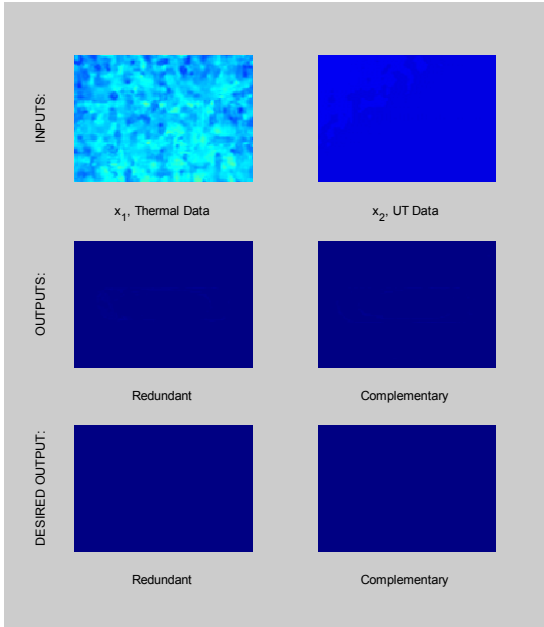


(g) Specimen 12a

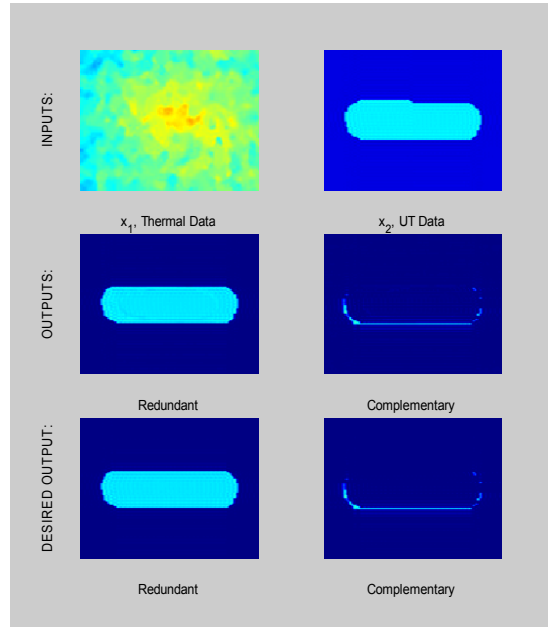


(h) Specimen 11a

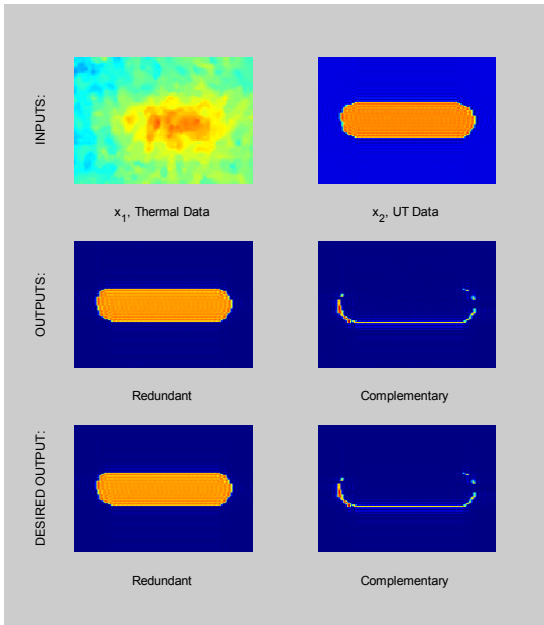
Trial 1: Thermal & UT Results (cont.)



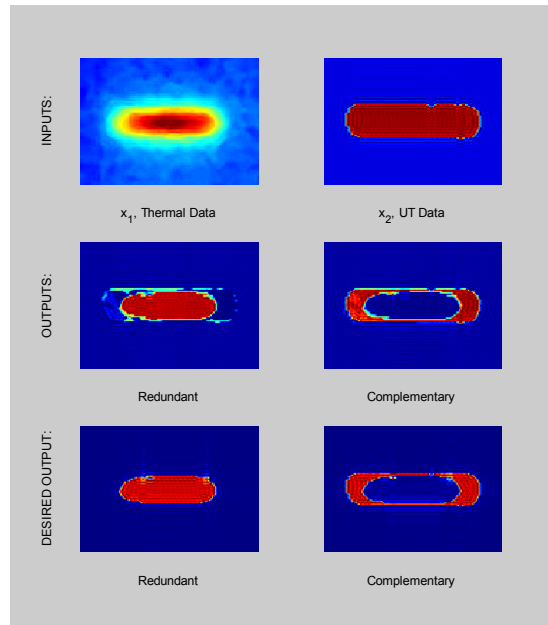
(i) Specimen 20a



(j) Specimen 23a

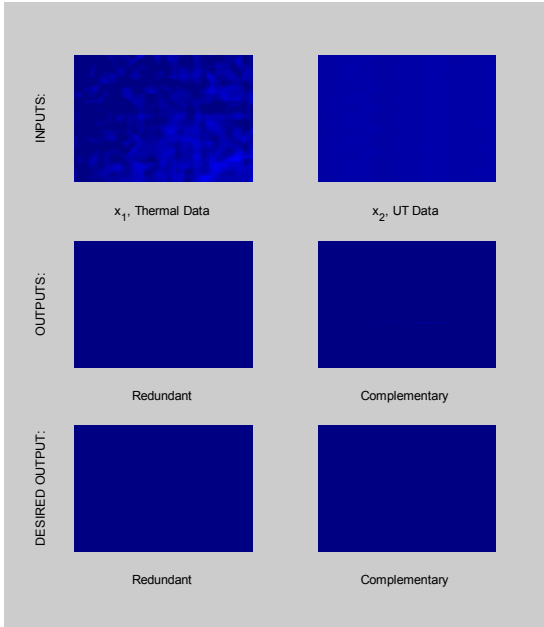


(k) Specimen 22a

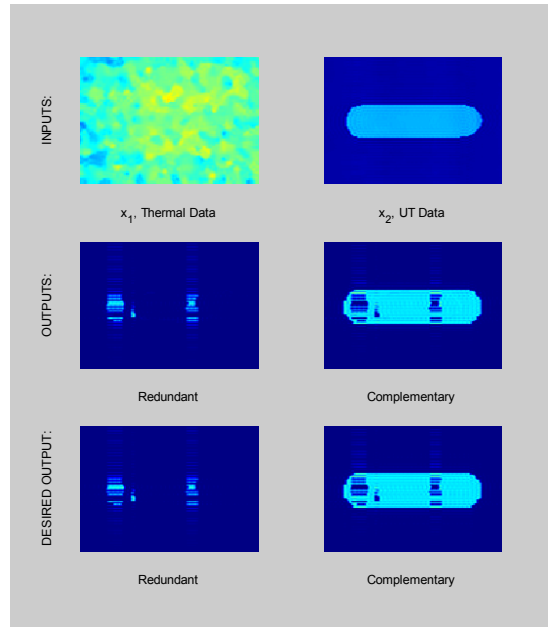


(l) Specimen 21a

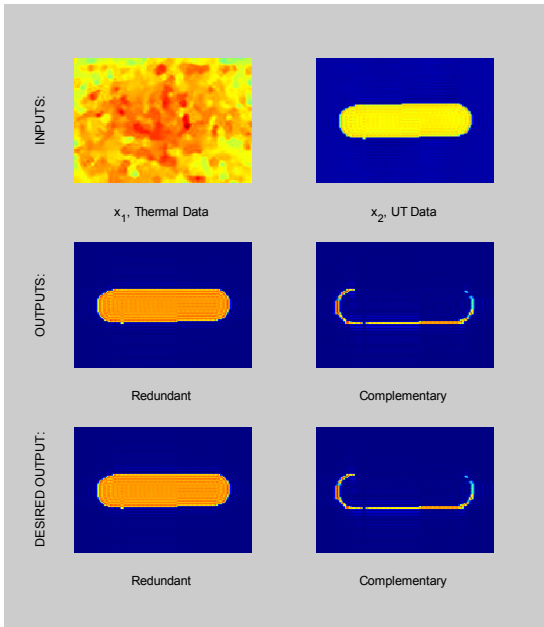
Trial 1: Thermal & UT Results (cont.)



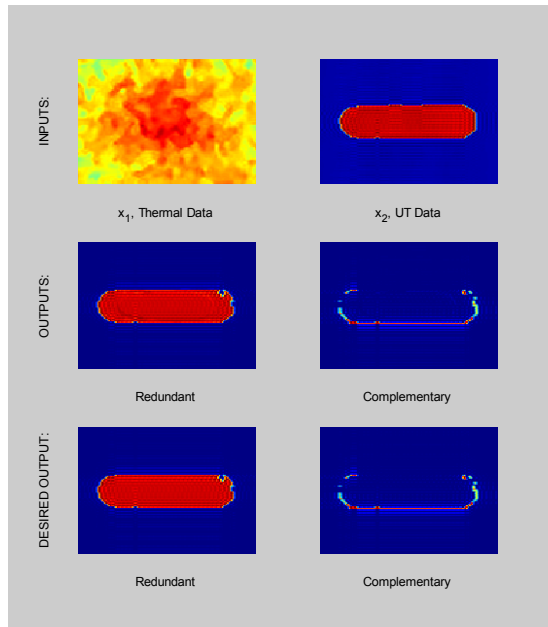
(m) Specimen 00b



(n) Specimen 03b

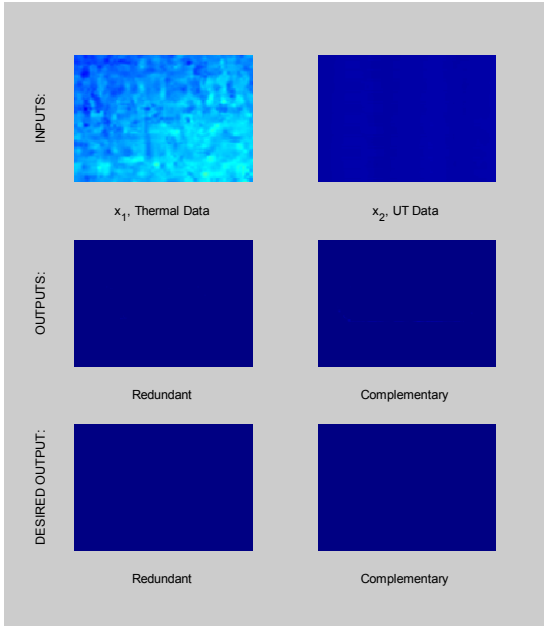


(o) Specimen 02b

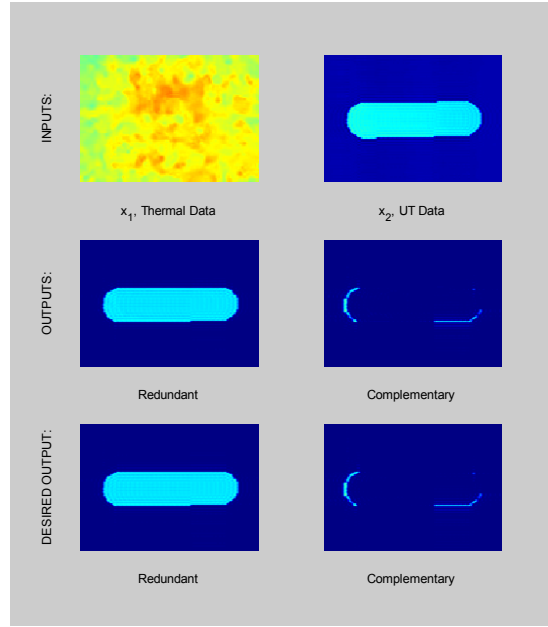


(p) Specimen 01b

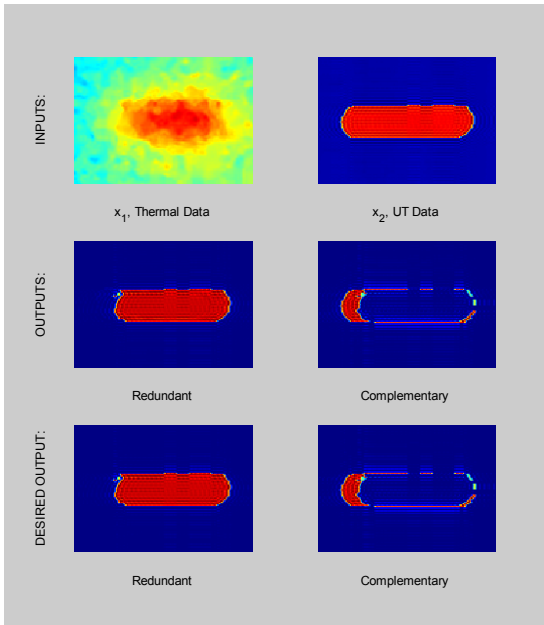
Trial 1: Thermal & UT Results (cont.)



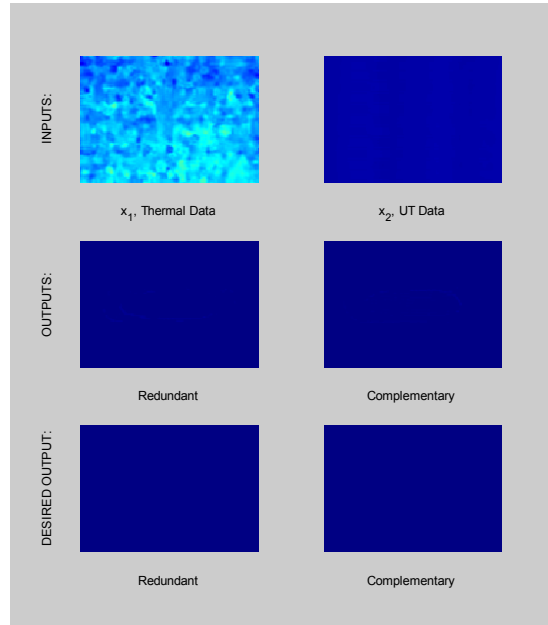
(q) Specimen 10b



(r) Specimen 13b

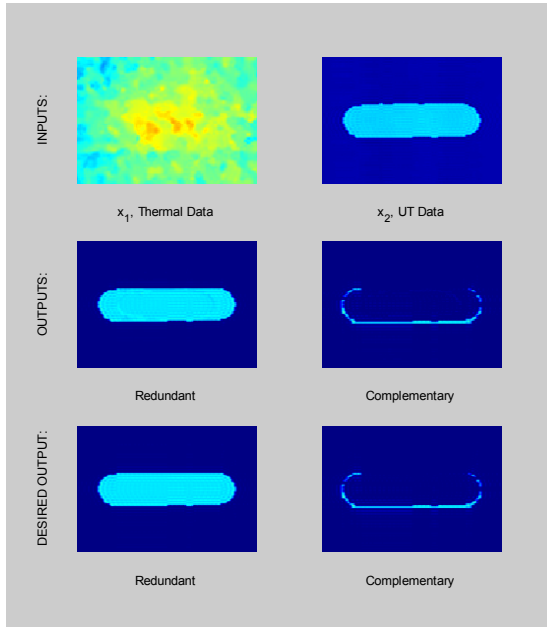


(s) Specimen 11b

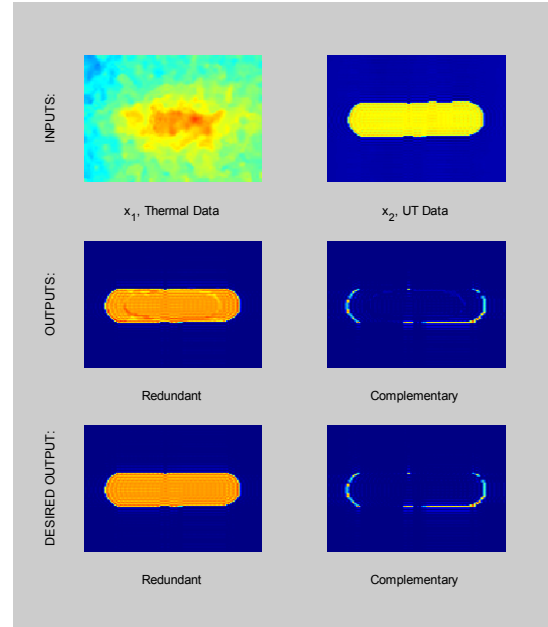


(t) Specimen 20b

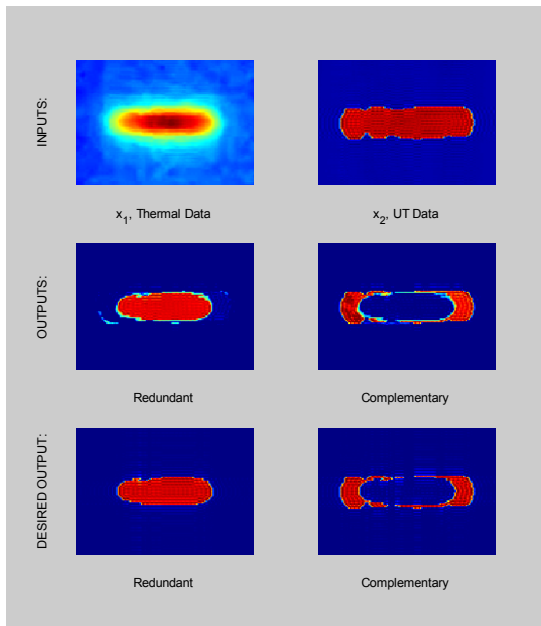
Trial 1: Thermal & UT Results (cont.)



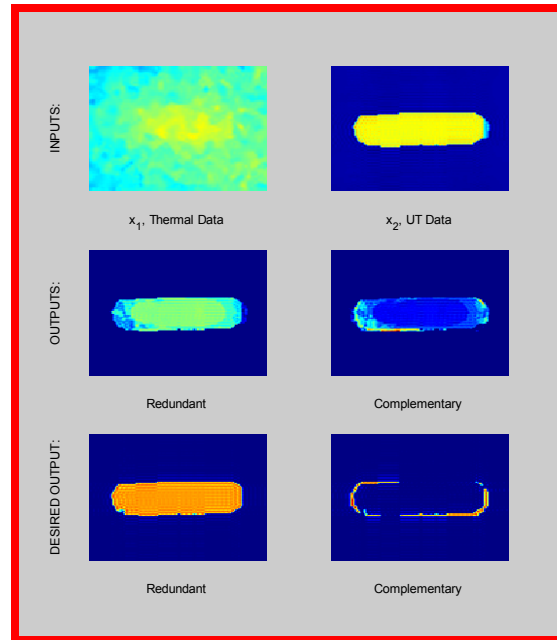
(u) Specimen 23b



(v) Specimen 22b



(w) Specimen 21b

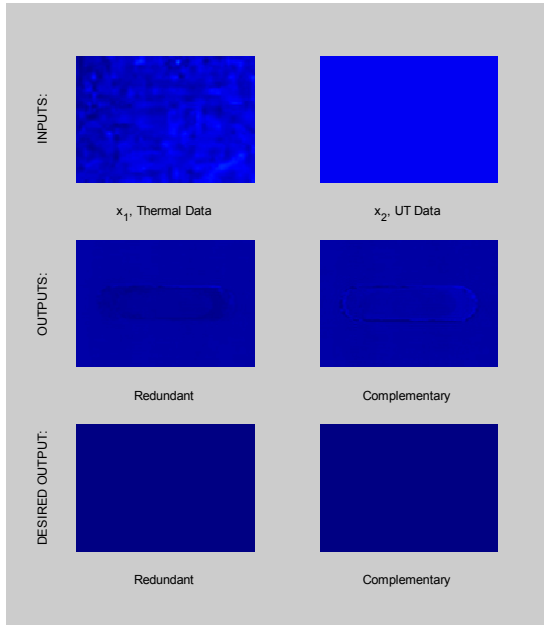


(x) Specimen 12b

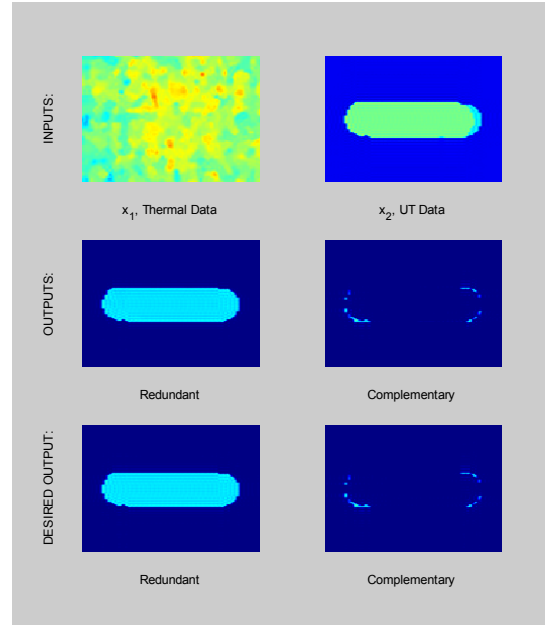
Figure 4.20: Thermal & UT combination Trial 1.

Training Data: (a) – (w); Test Data: (x)

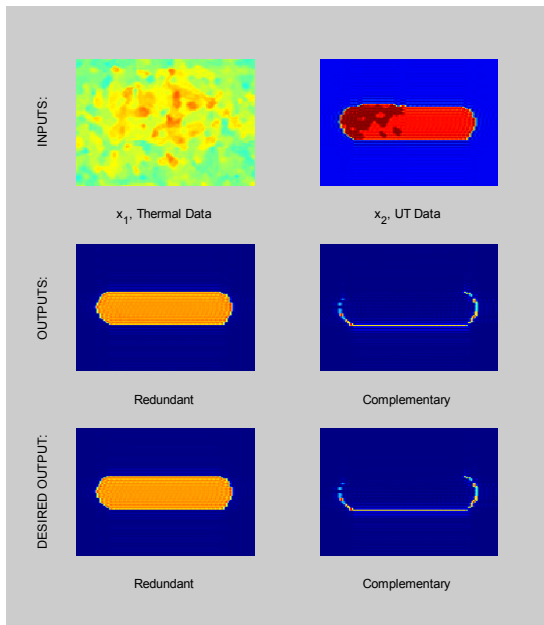
Trial 2: Thermal & UT Results



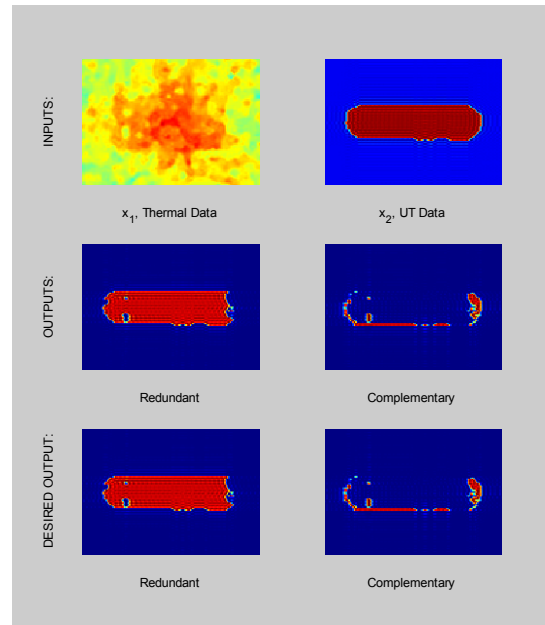
(a) Specimen 00a



(b) Specimen 03a

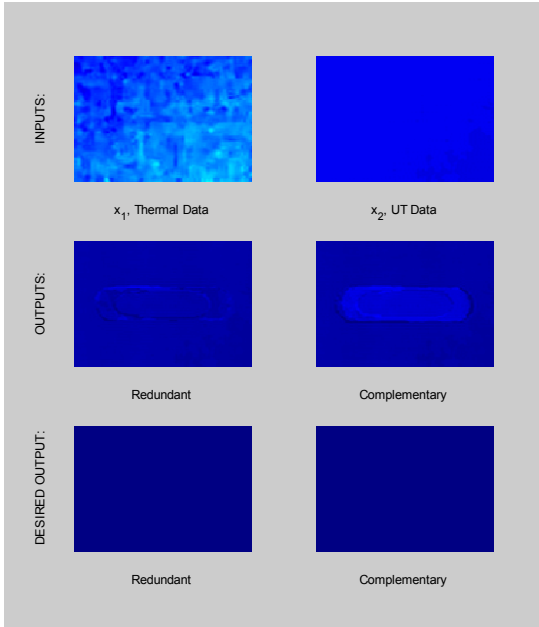


(c) Specimen 02a

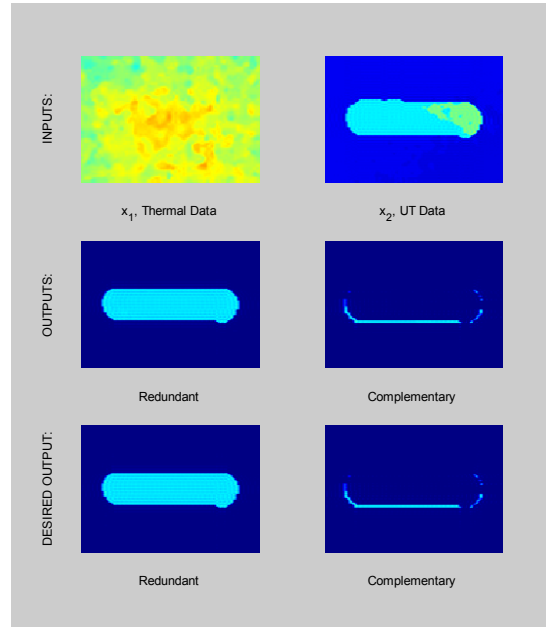


(d) Specimen 01a

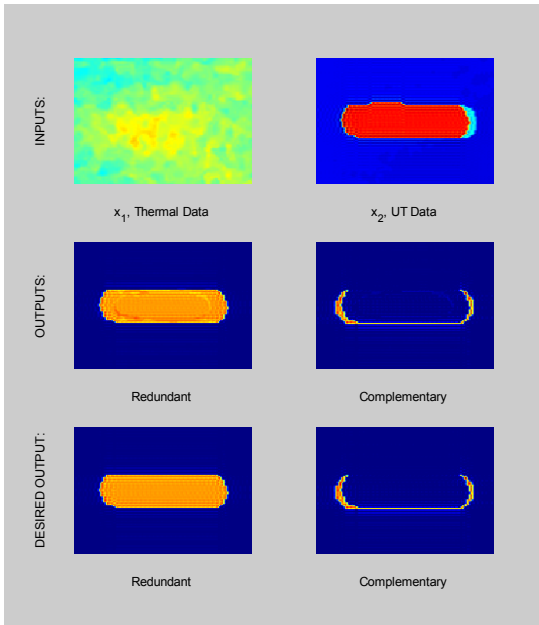
Trial 2: Thermal & UT Results (cont.)



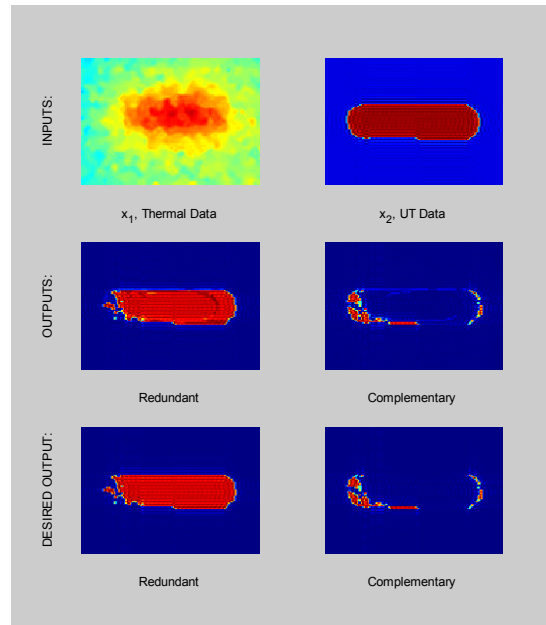
(e) Specimen 10a



(f) Specimen 13a

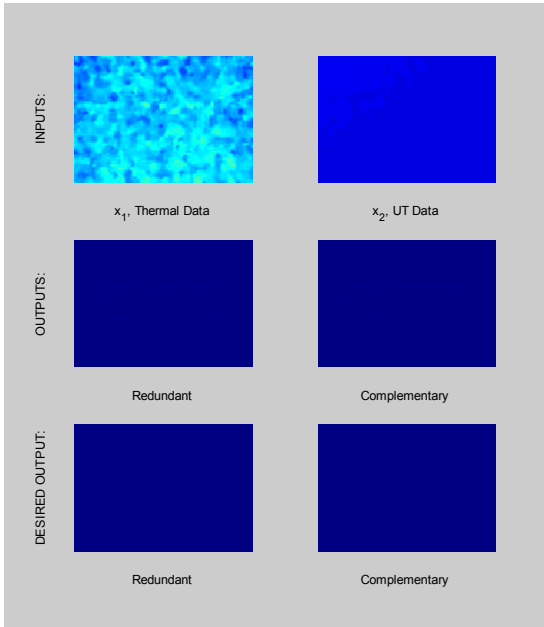


(g) Specimen 12a

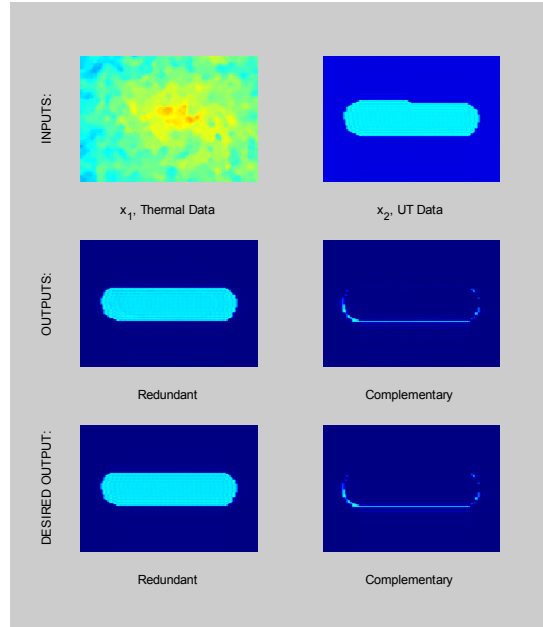


(h) Specimen 11a

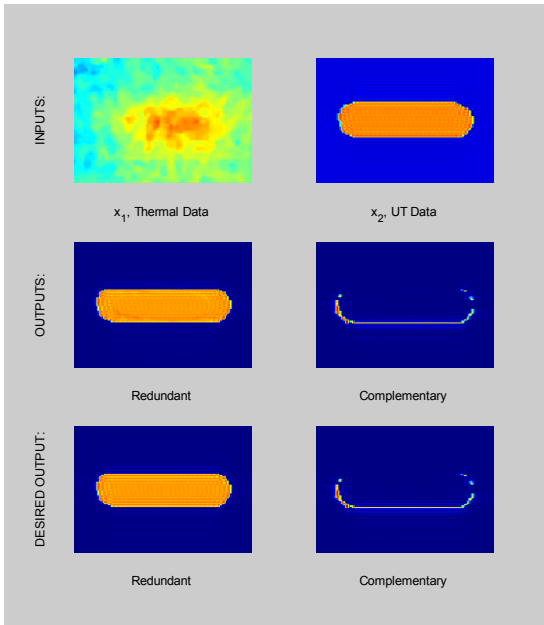
Trial 2: Thermal & UT Results (cont.)



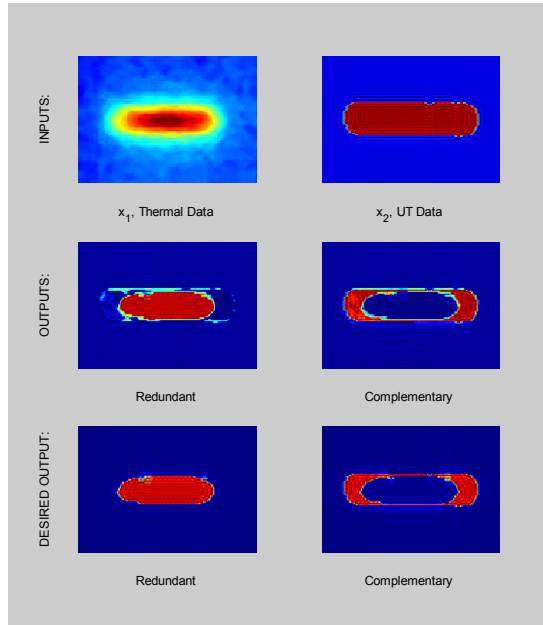
(i) Specimen 20a



(j) Specimen 23a

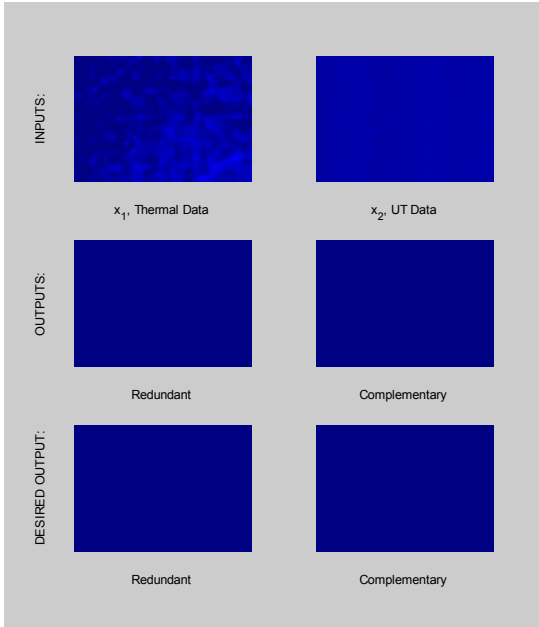


(k) Specimen 22a

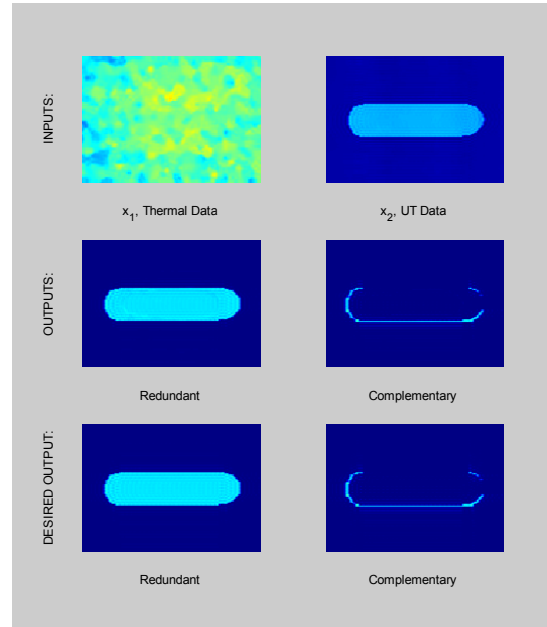


(l) Specimen 21a

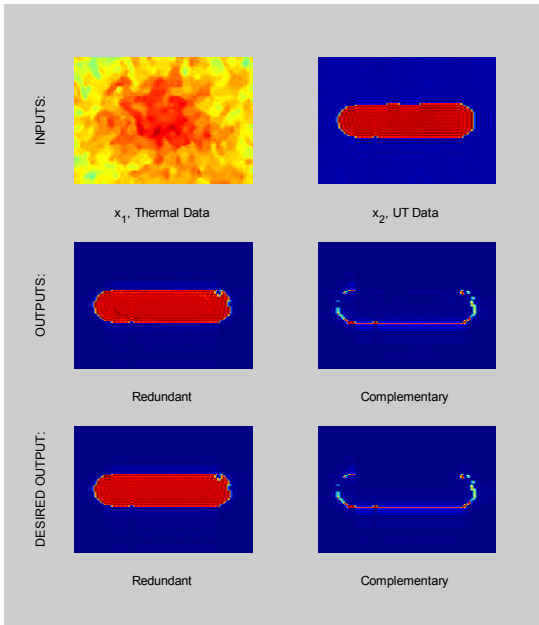
Trial 2: Thermal & UT Results (cont.)



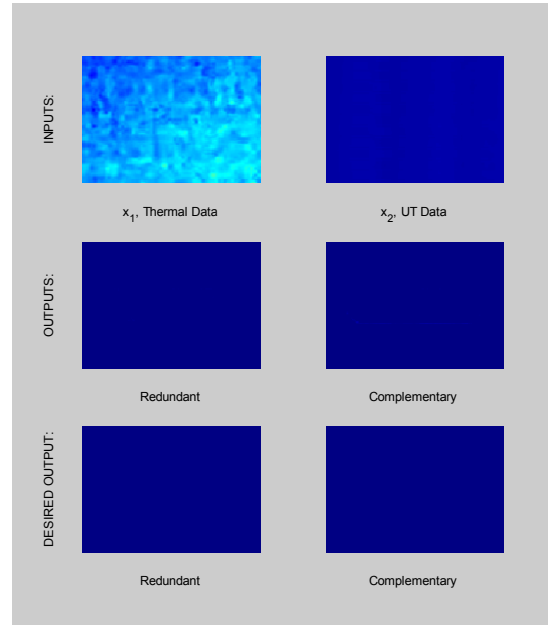
(m) Specimen 00b



(n) Specimen 03b

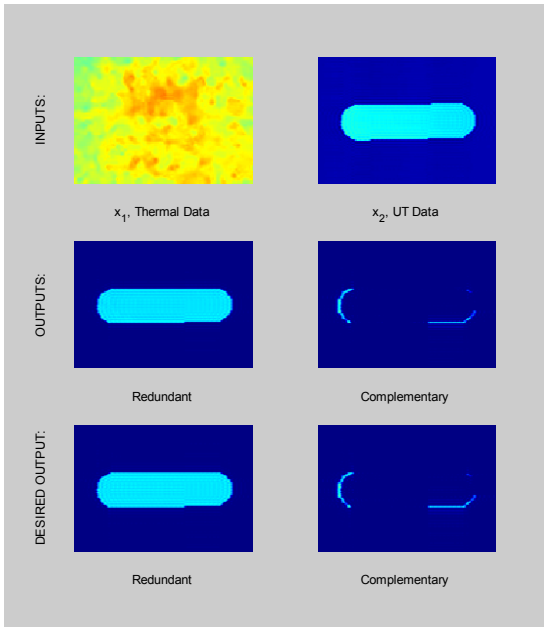


(o) Specimen 01b

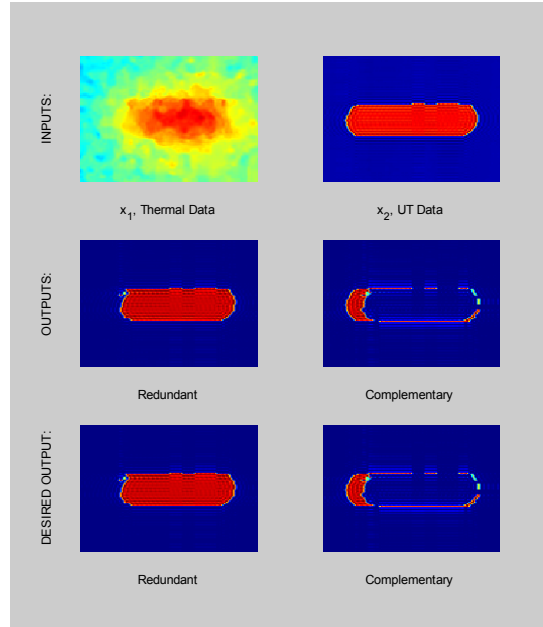


(p) Specimen 10b

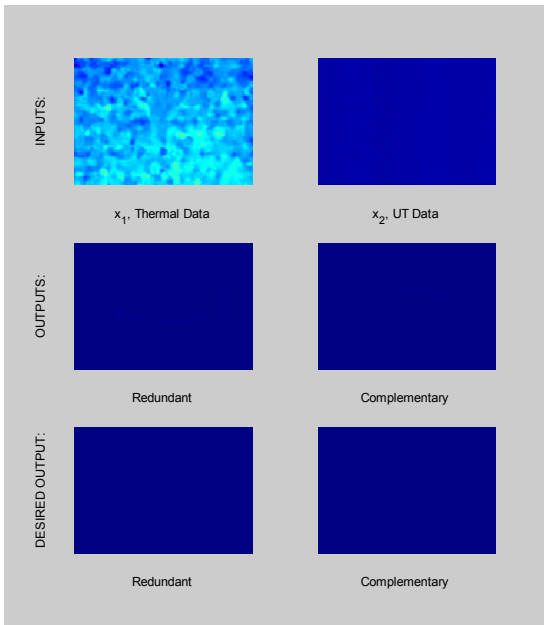
Trial 2: Thermal & UT Results (cont.)



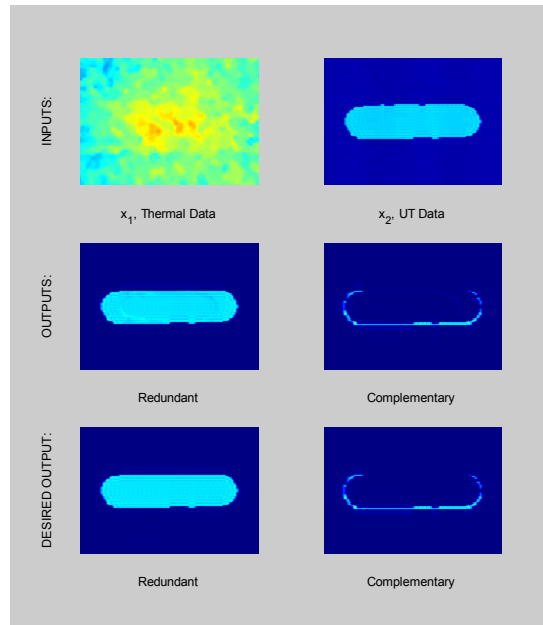
(q) Specimen 13b



(r) Specimen 11b

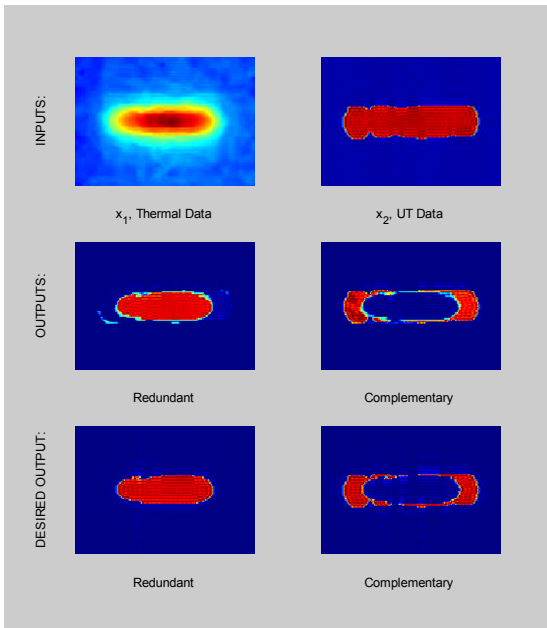


(s) Specimen 20b

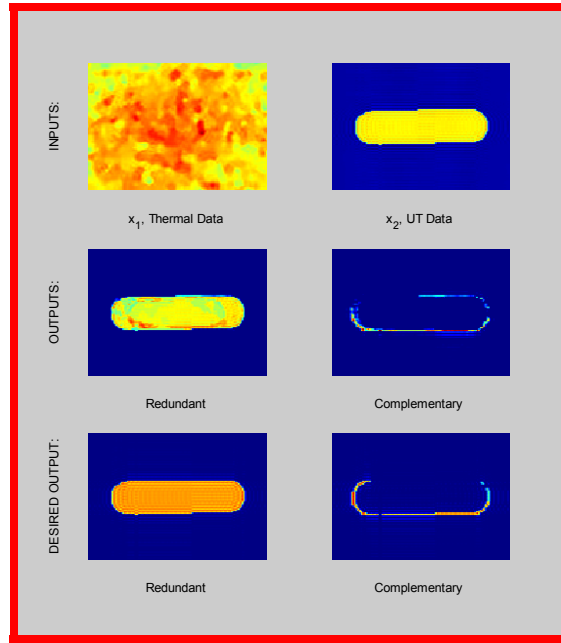


(t) Specimen 23b

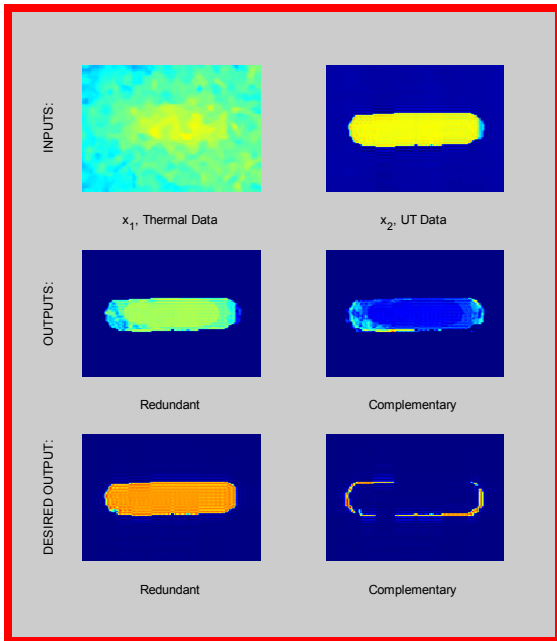
Trial 2: Thermal & UT Results (cont.)



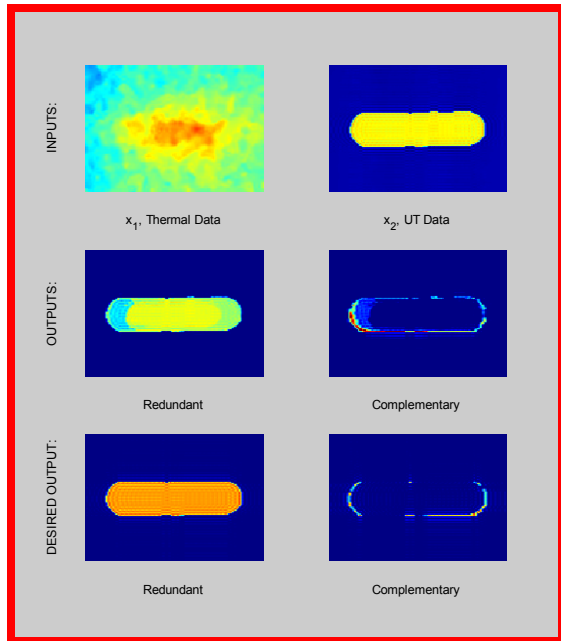
(u) Specimen 21b



(v) Specimen 02b



(w) Specimen 12b

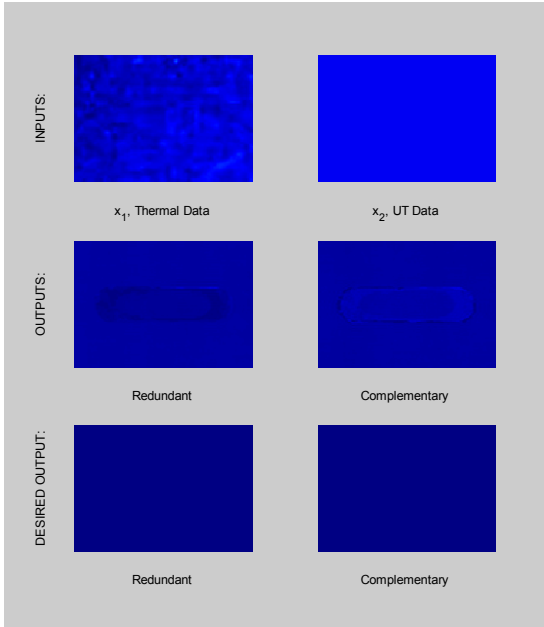


(x) Specimen 22b

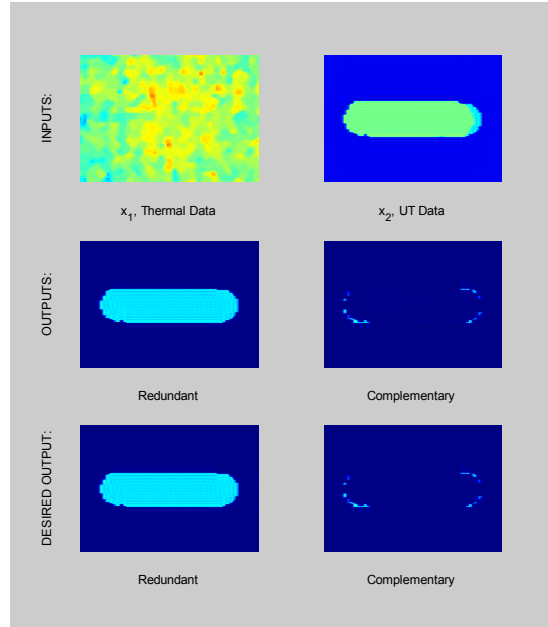
Figure 4.21: Thermal & UT combination Trial 2.

Training Data: (a) – (u); Test Data: (v), (w), (x)

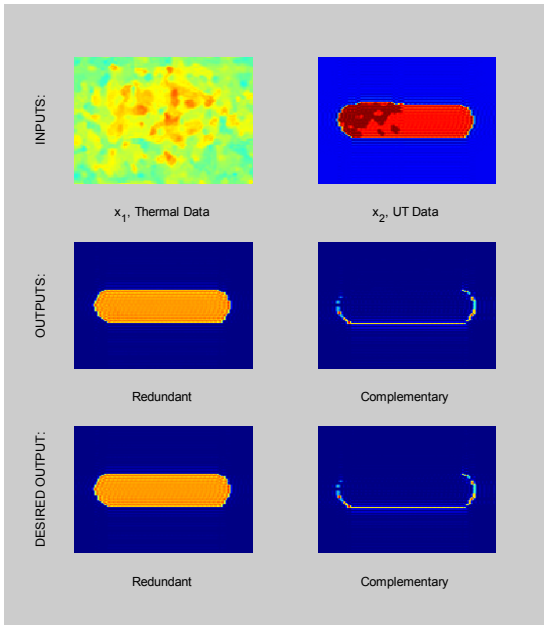
Trial 3: Thermal & UT Results



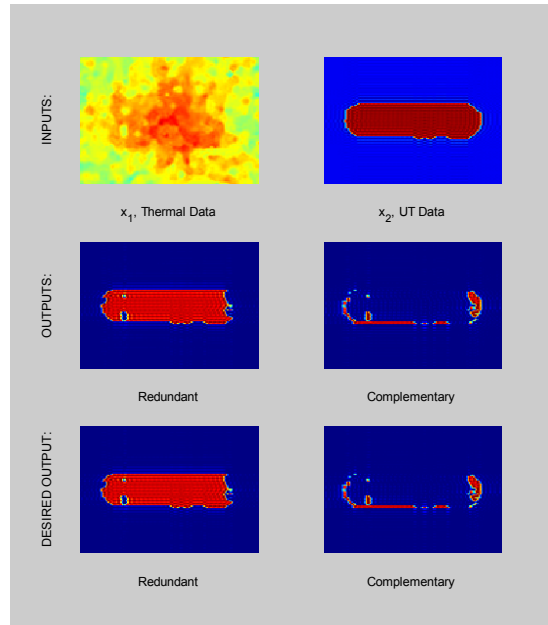
(a) Specimen 00a



(b) Specimen 03a

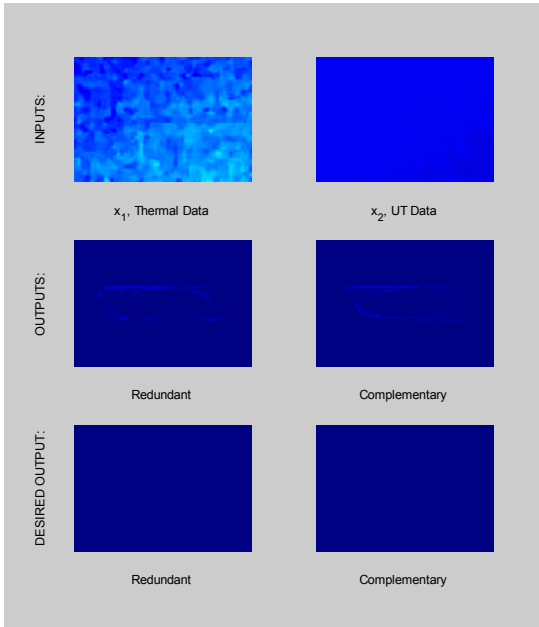


(c) Specimen 02a

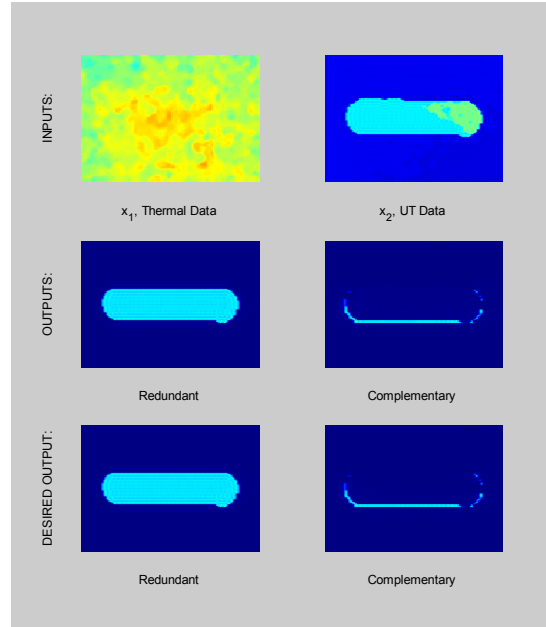


(d) Specimen 01a

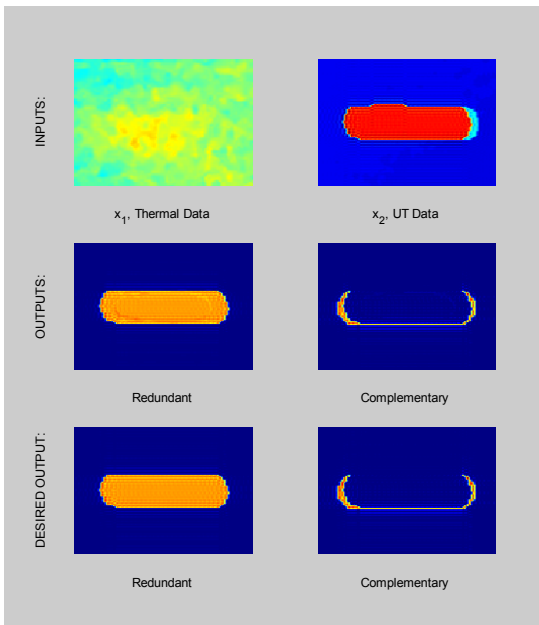
Trial 3: Thermal & UT Results (cont.)



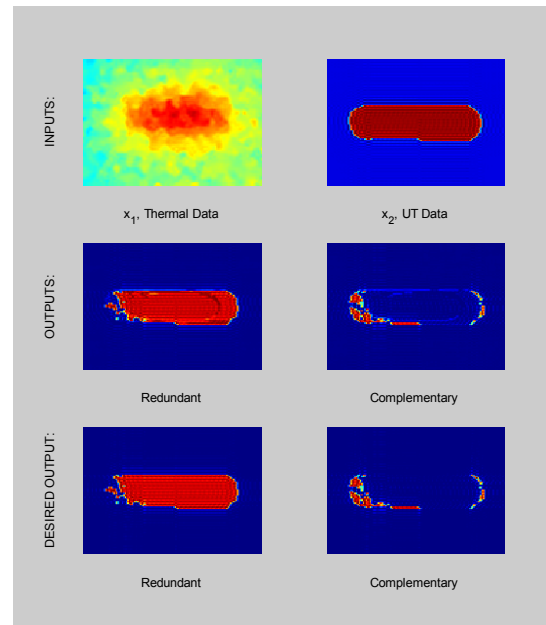
(e) Specimen 10a



(f) Specimen 13a

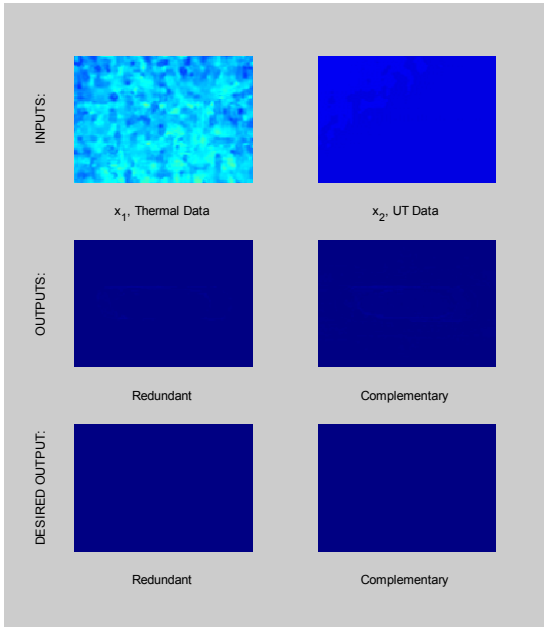


(g) Specimen 12a

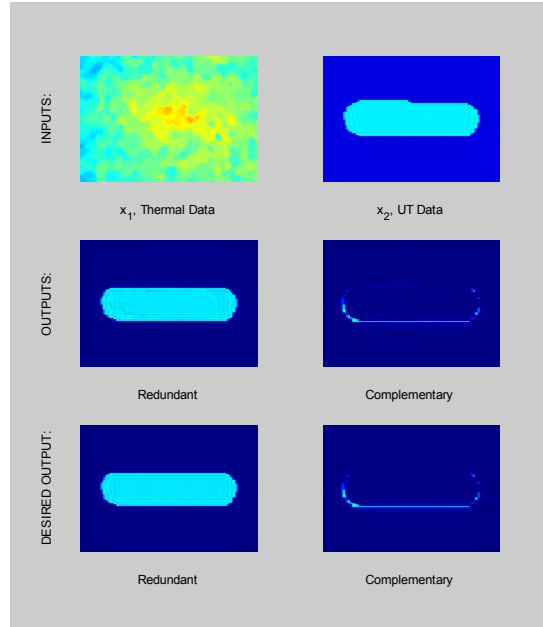


(h) Specimen 11a

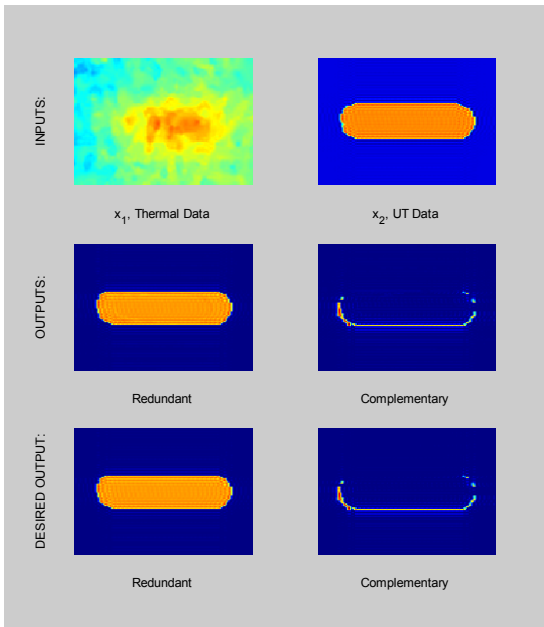
Trial 3: Thermal & UT Results (cont.)



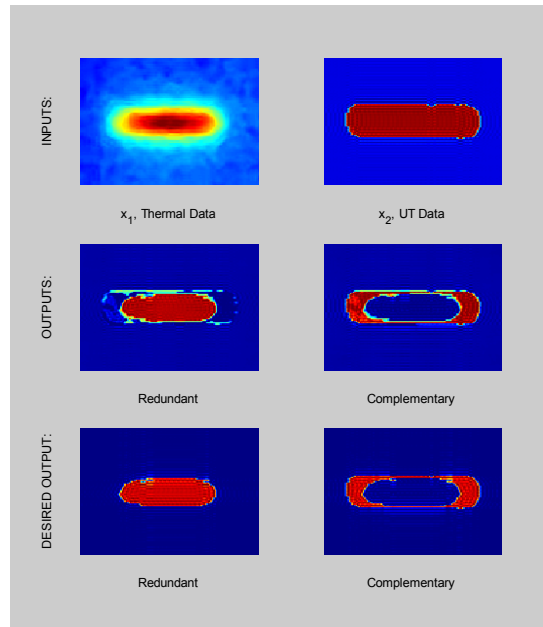
(i) Specimen 20a



(j) Specimen 23a

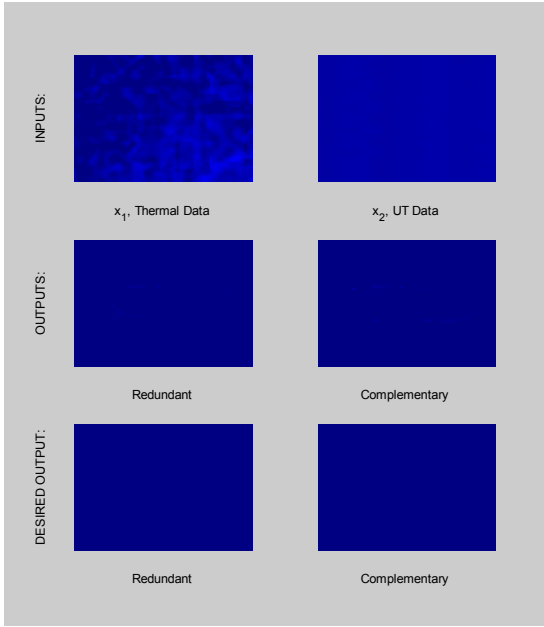


(k) Specimen 22a

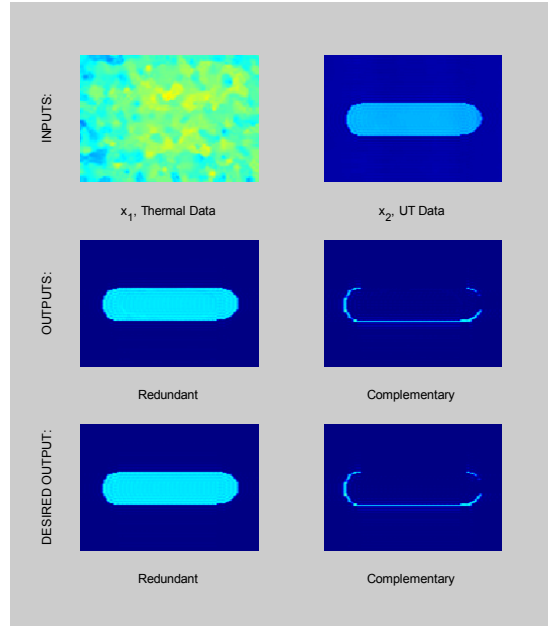


(l) Specimen 21a

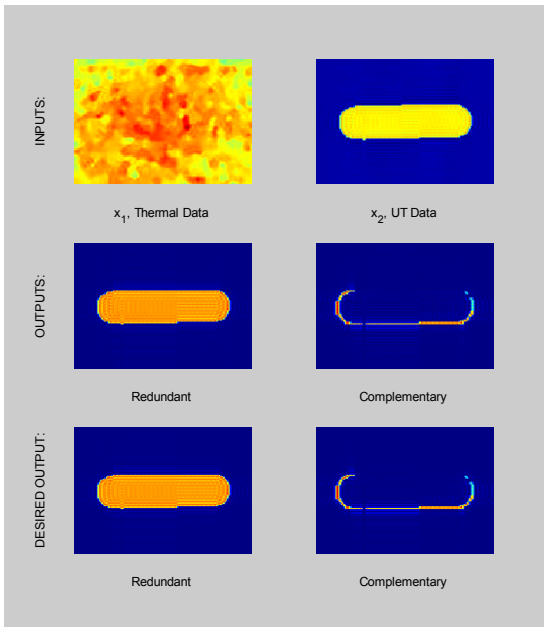
Trial 3: Thermal & UT Results (cont.)



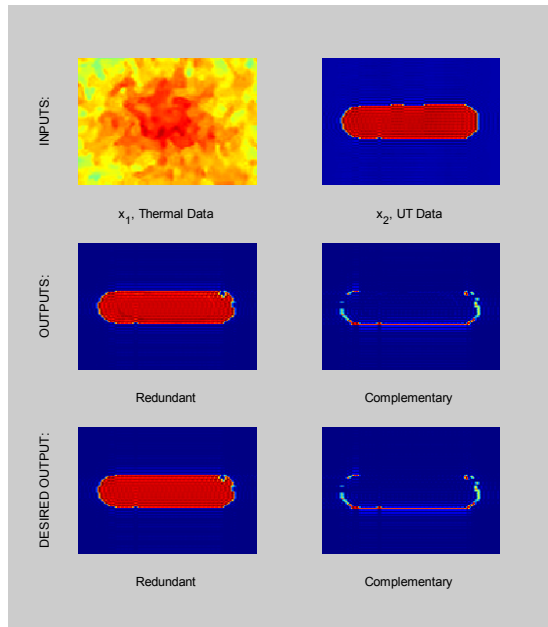
(m) Specimen 00b



(n) Specimen 03b

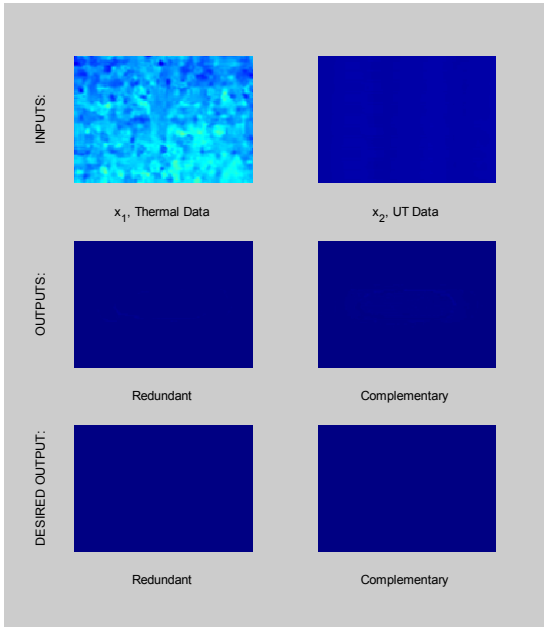


(o) Specimen 02b

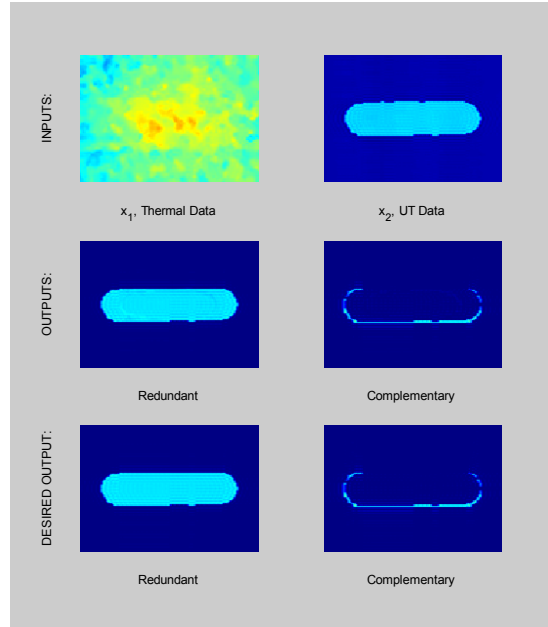


(p) Specimen 01b

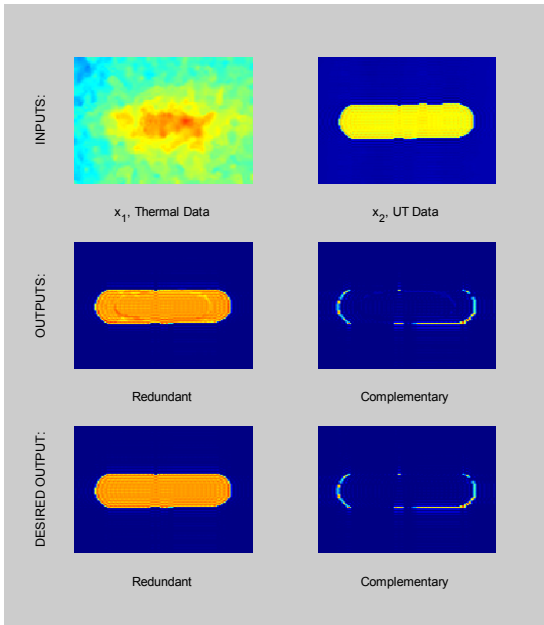
Trial 3: Thermal & UT Results (cont.)



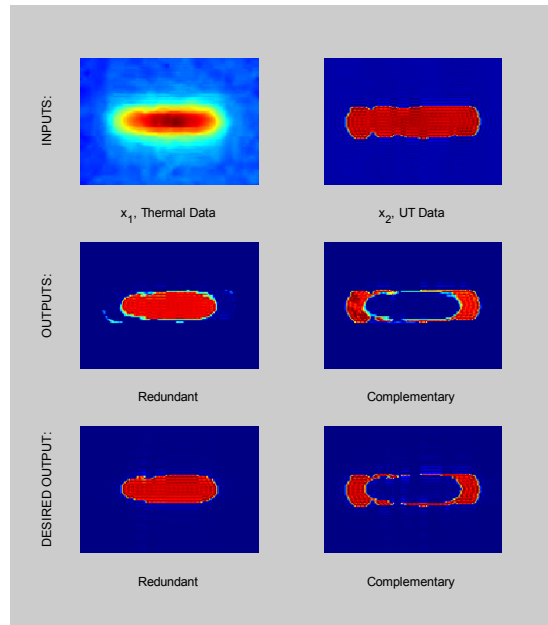
(q) Specimen 20b



(r) Specimen 23b

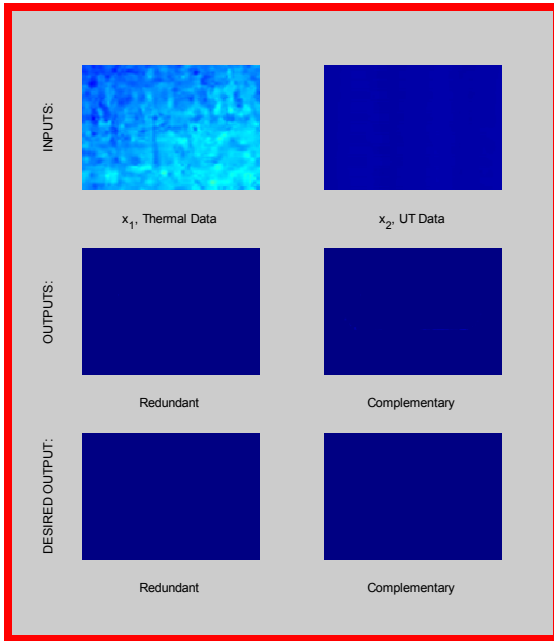


(s) Specimen 22b

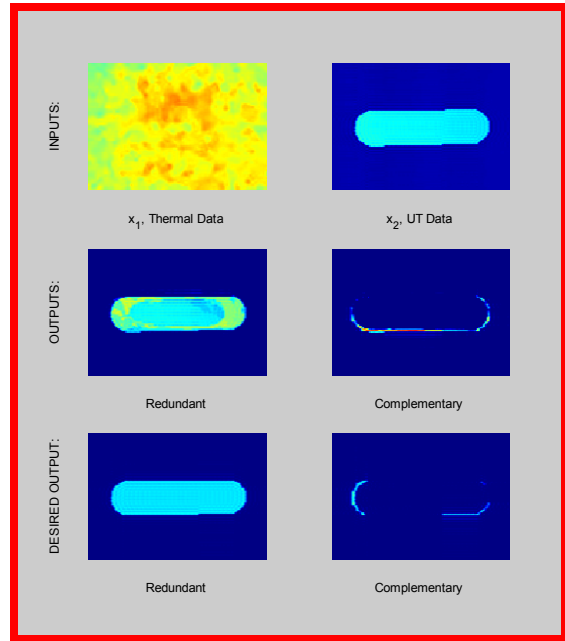


(t) Specimen 21b

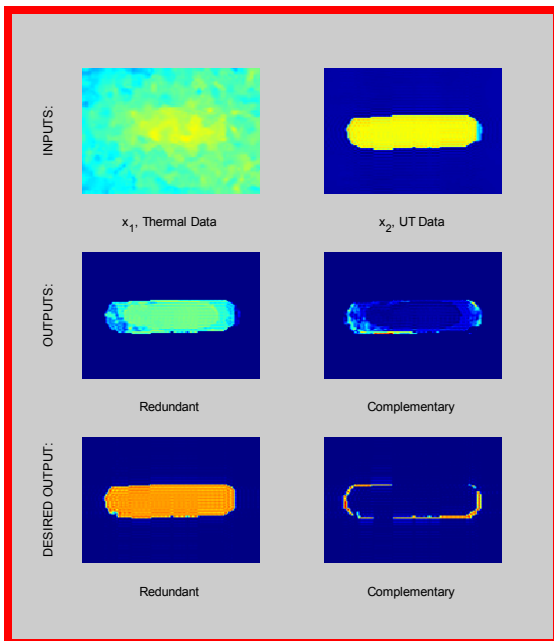
Trial 3: Thermal & UT Results (cont.)



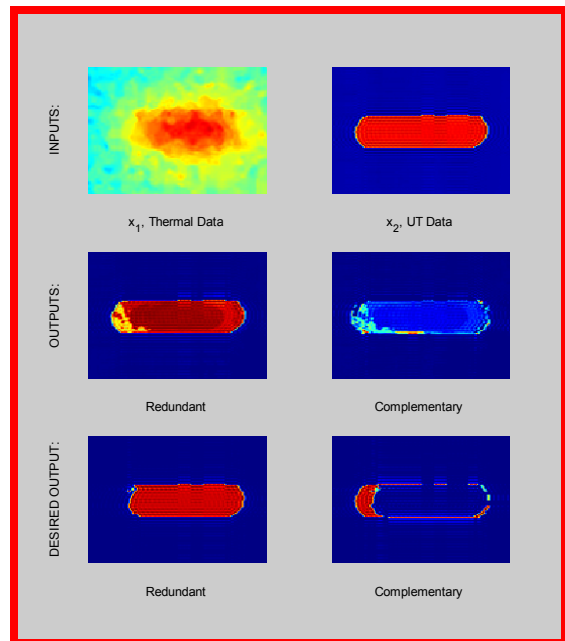
(u) Specimen 10b



(v) Specimen 13b



(w) Specimen 12b



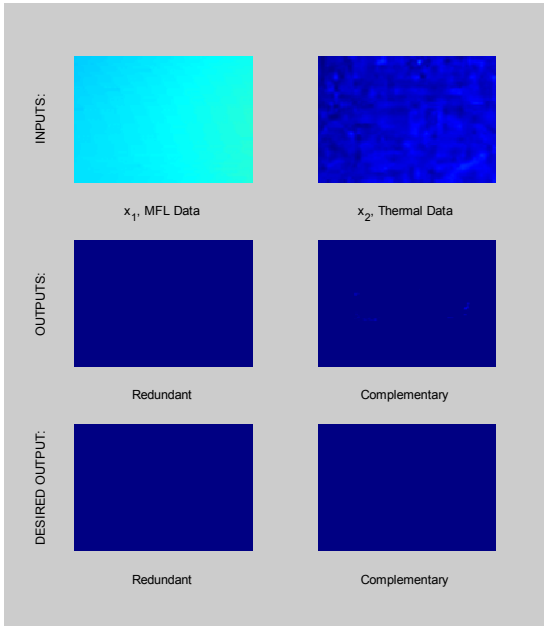
(x) Specimen 11b

Figure 4.22: Thermal & UT combination Trial 3.

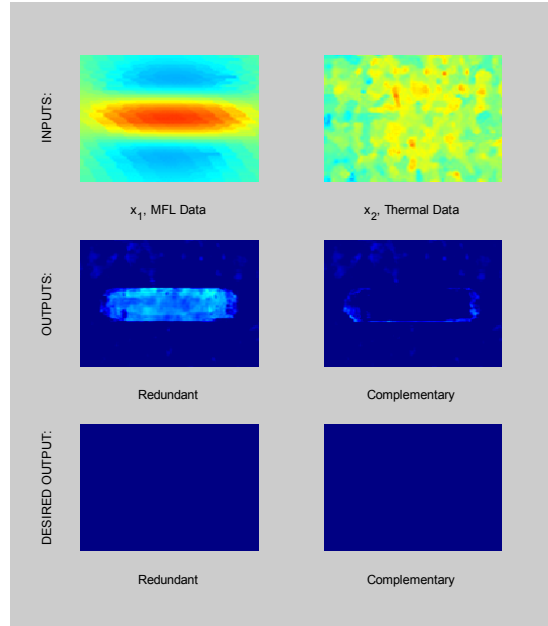
Training Data: (a) – (t); Test Data: (u), (v), (w), (x)

4.2.2.3 MFL & Thermal Data Fusion Results

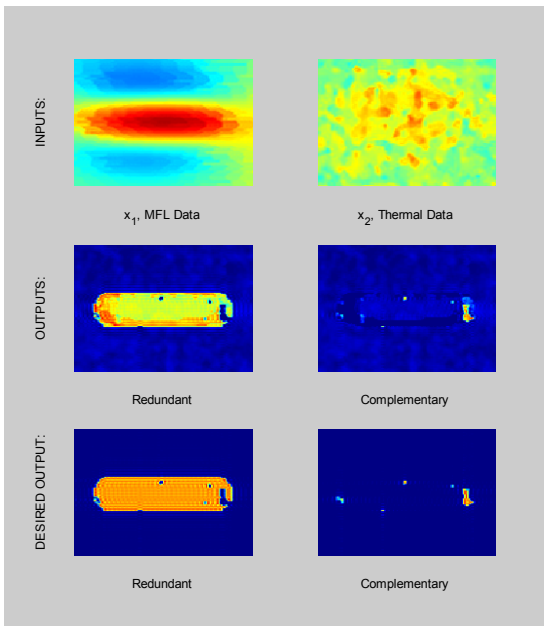
Trial 1: MFL & Thermal Results



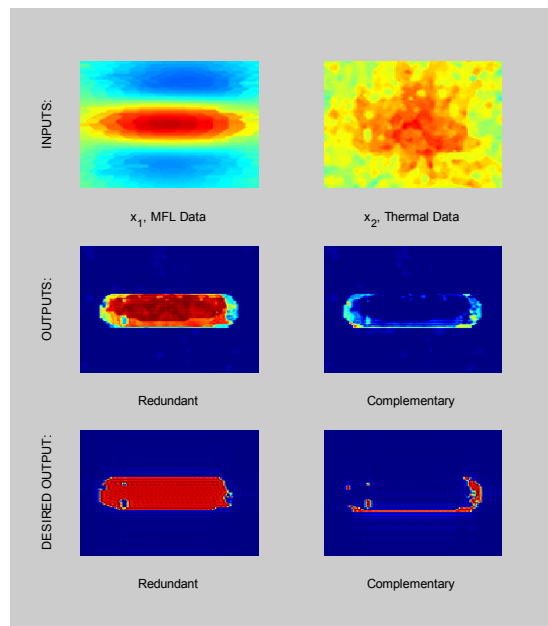
(a) Specimen 00a



(b) Specimen 03a

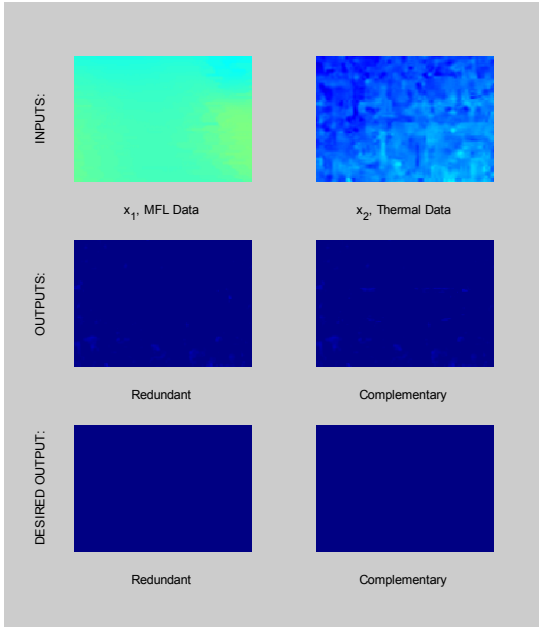


(c) Specimen 02a

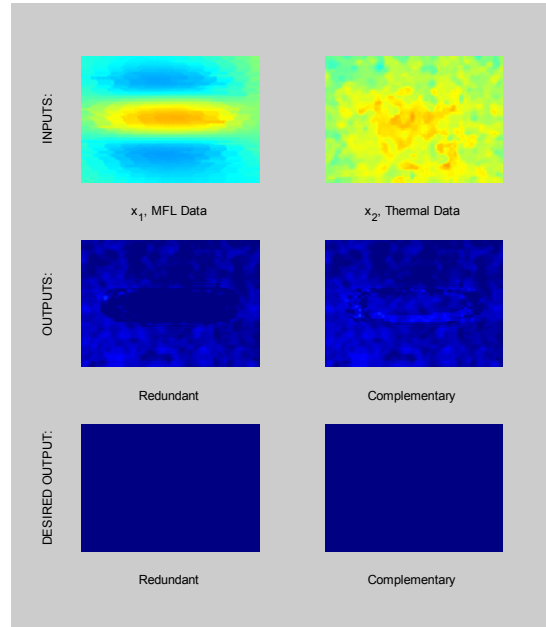


(d) Specimen 01a

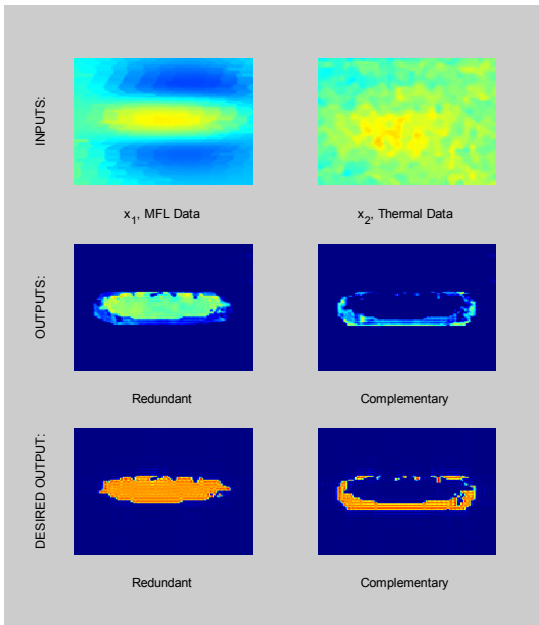
Trial 1: MFL & Thermal Results (cont.)



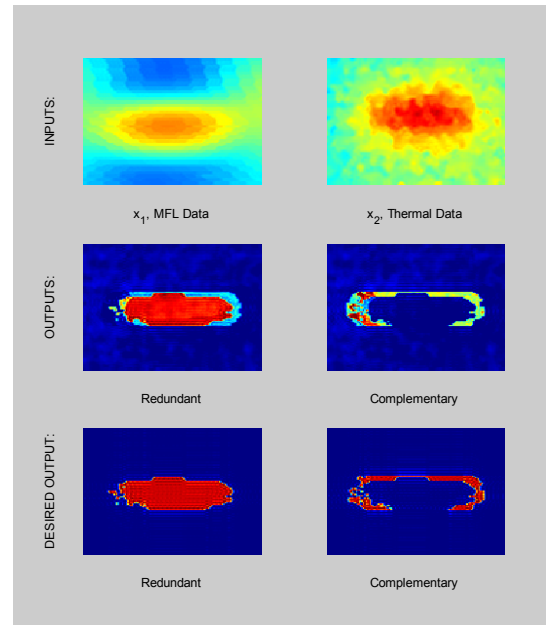
(e) Specimen 10a



(f) Specimen 13a

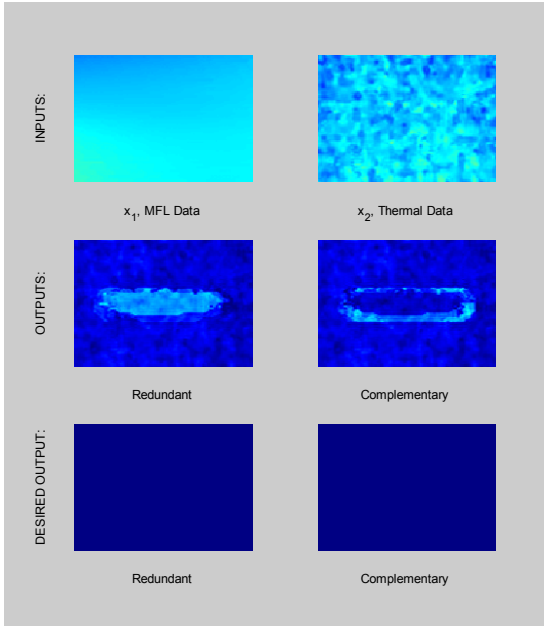


(g) Specimen 12a

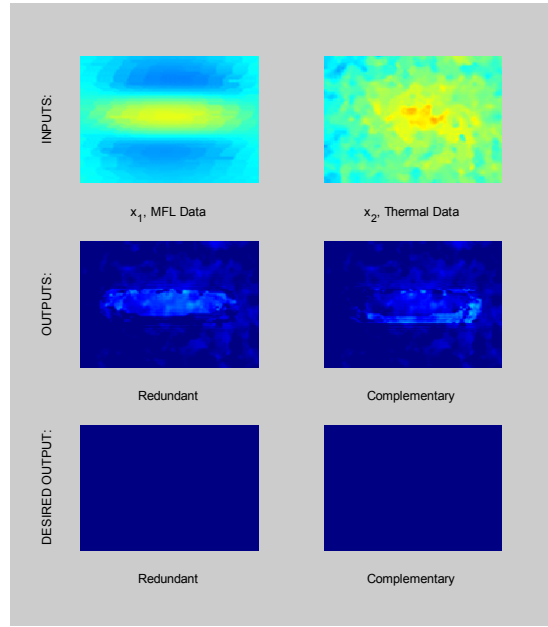


(h) Specimen 11a

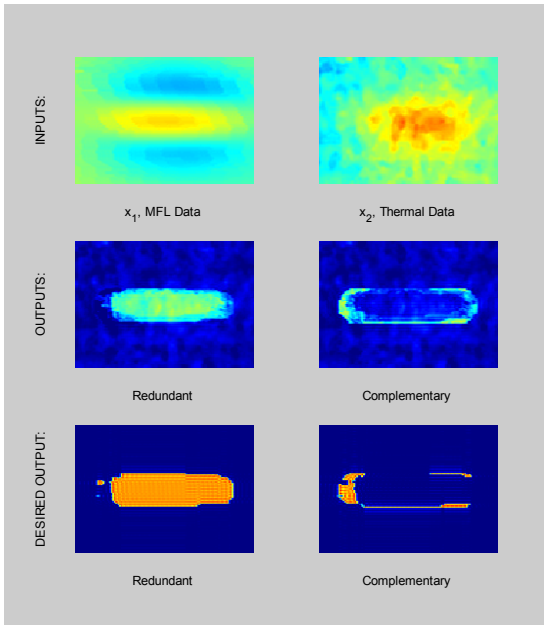
Trial 1: MFL & Thermal Results (cont.)



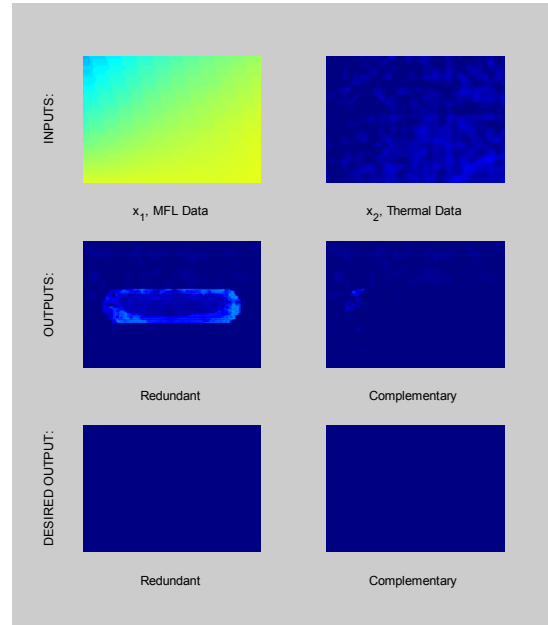
(i) Specimen 20a



(j) Specimen 23a

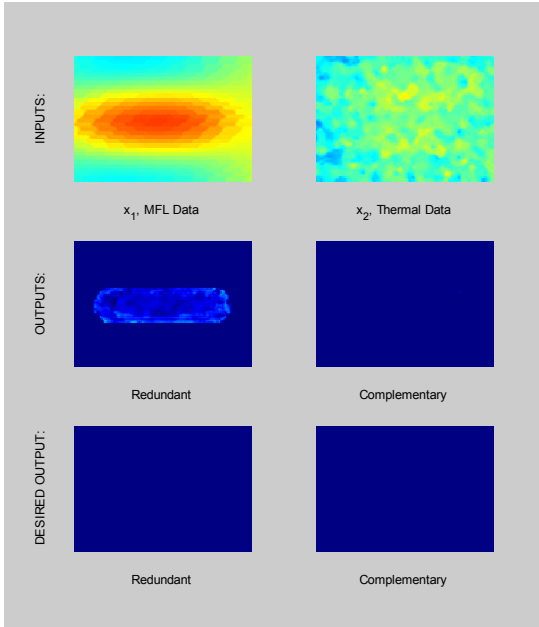


(k) Specimen 22a

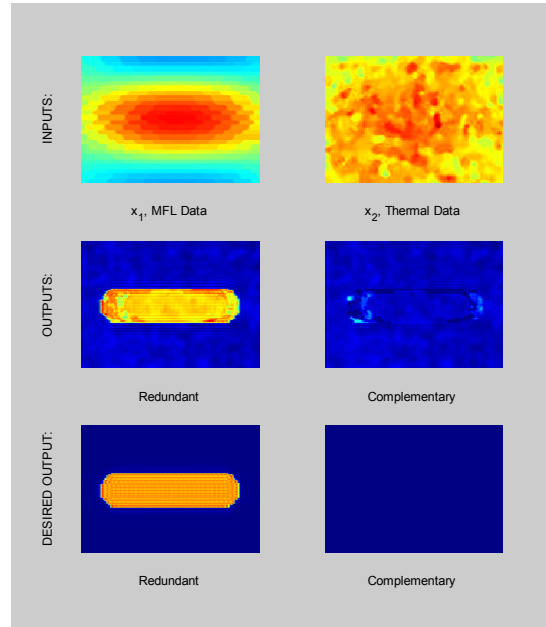


(l) Specimen 00b

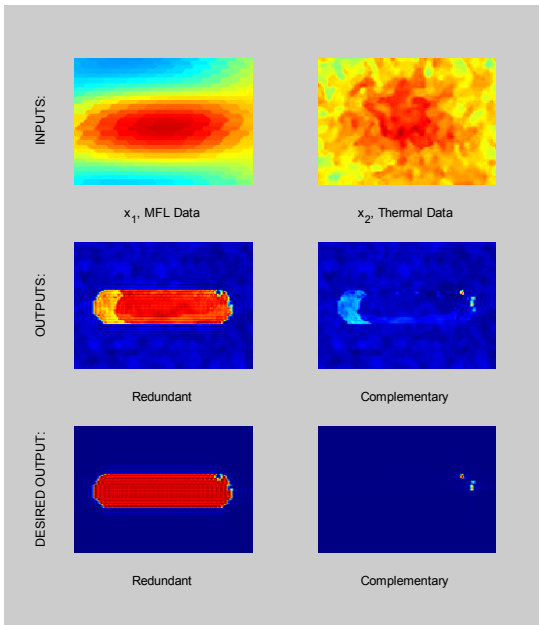
Trial 1: MFL & Thermal Results (cont.)



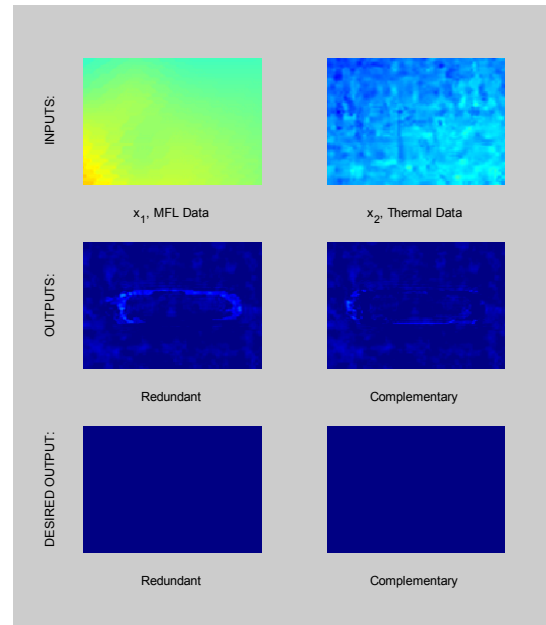
(m) Specimen 03b



(n) Specimen 02b

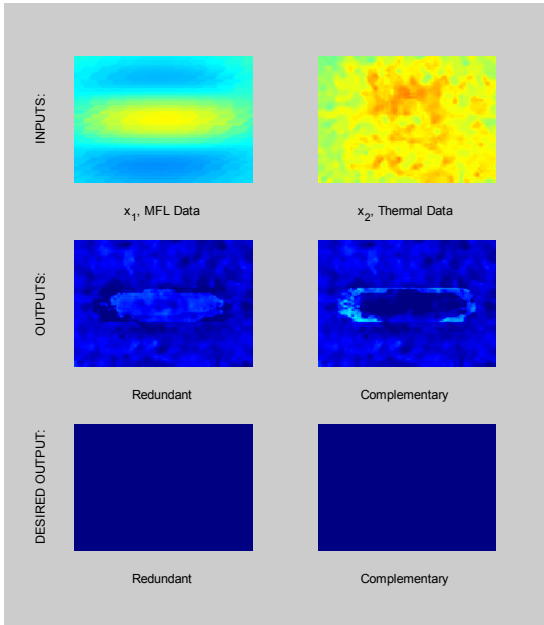


(o) Specimen 01b

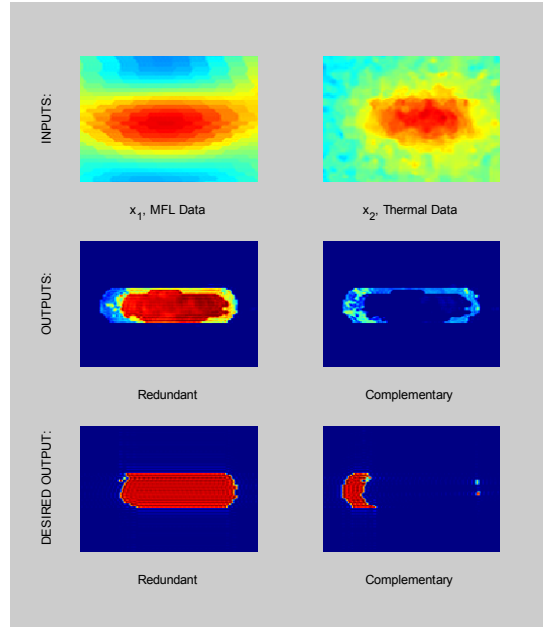


(p) Specimen 10b

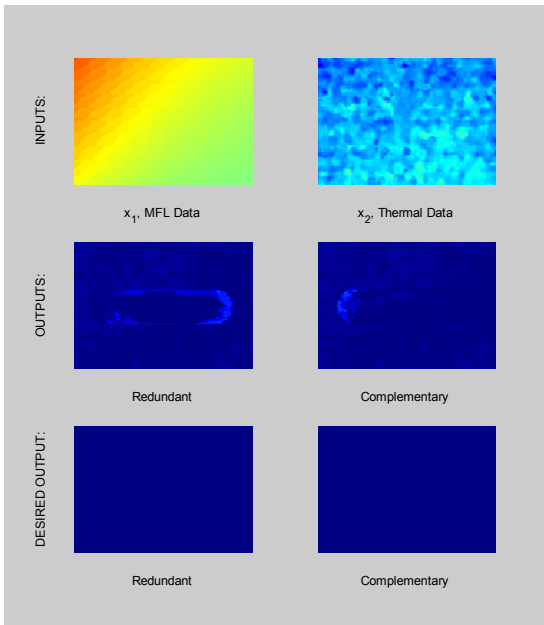
Trial 1: MFL & Thermal Results (cont.)



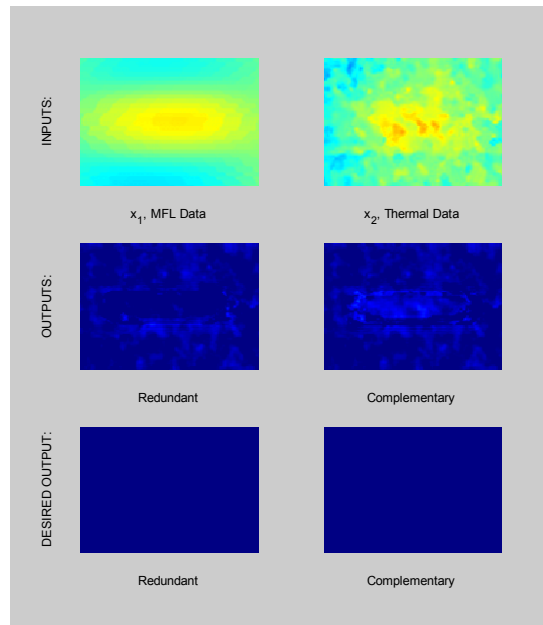
(q) Specimen 13b



(r) Specimen 11b

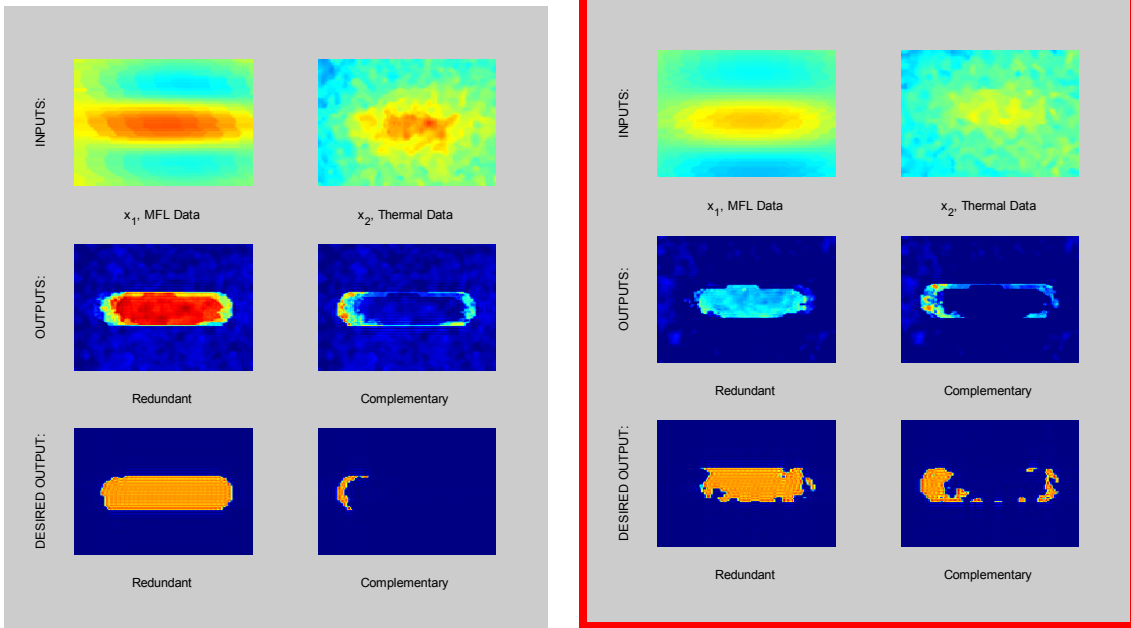


(s) Specimen 20b



(t) Specimen 23b

Trial 1: MFL & Thermal Results (cont.)



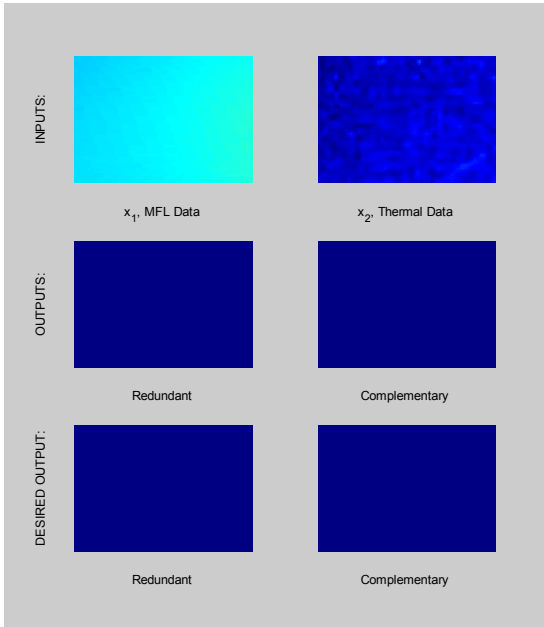
(u) Specimen 21b

(v) Specimen 12b

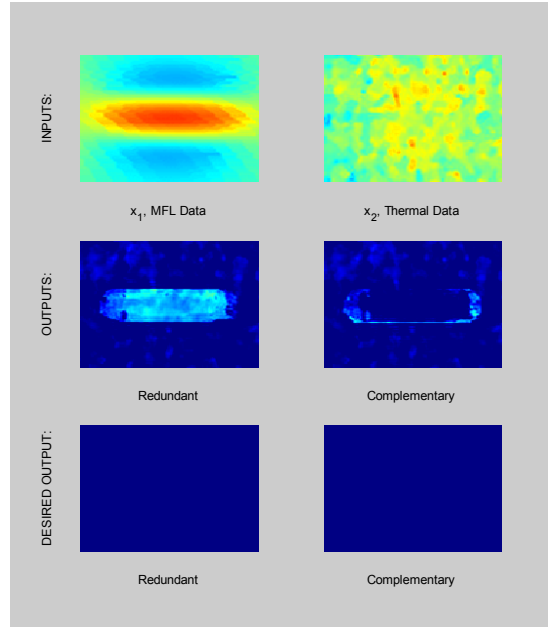
Figure 4.23: MFL & Thermal combination Trial 1.

Training Data: (a) – (u); Test Data: (v)

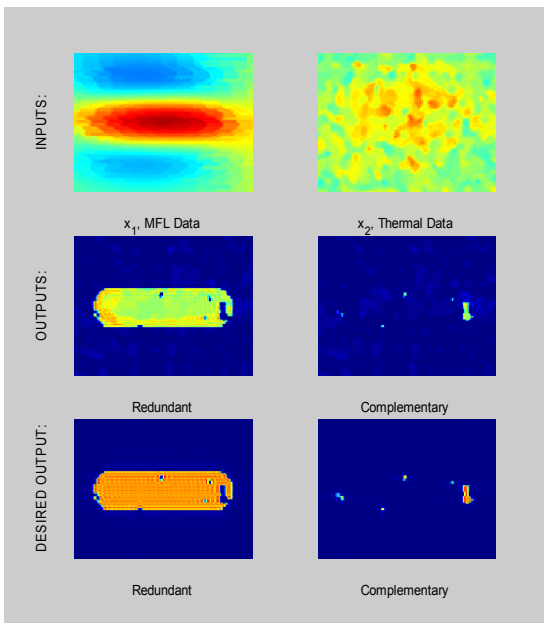
Trial 2: MFL & Thermal Results



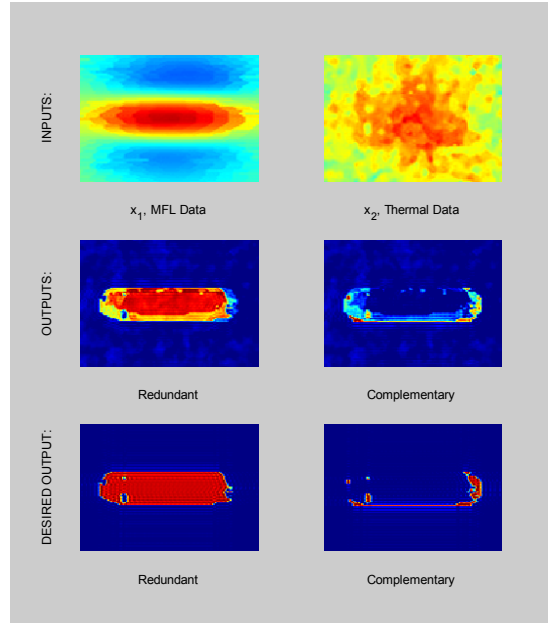
(a) Specimen 00a



(b) Specimen 03a

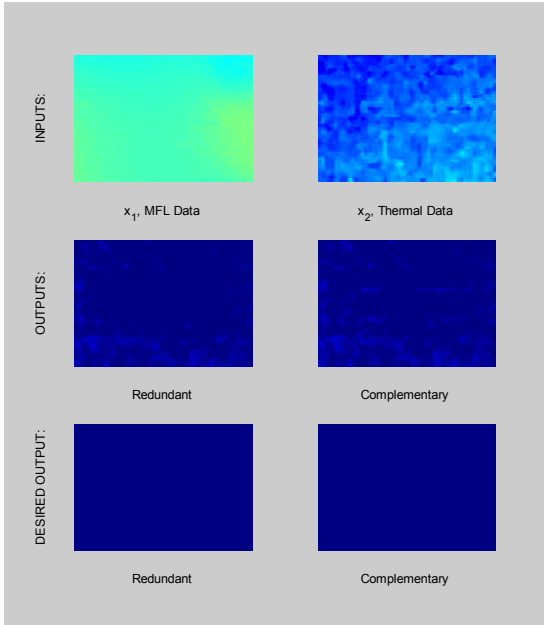


(c) Specimen 02a

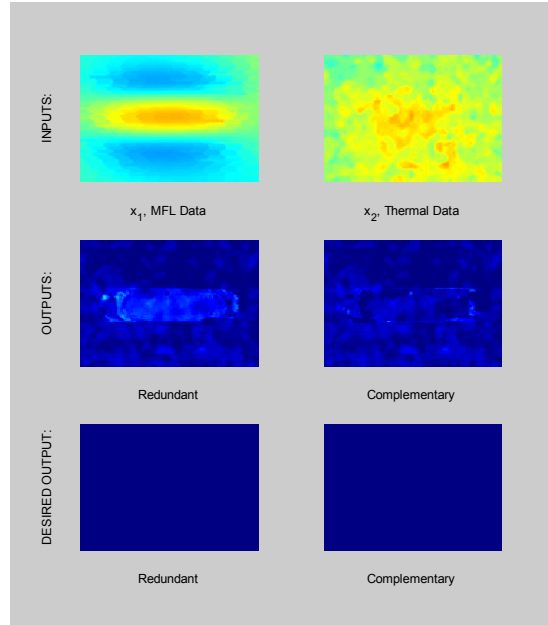


(d) Specimen 01a

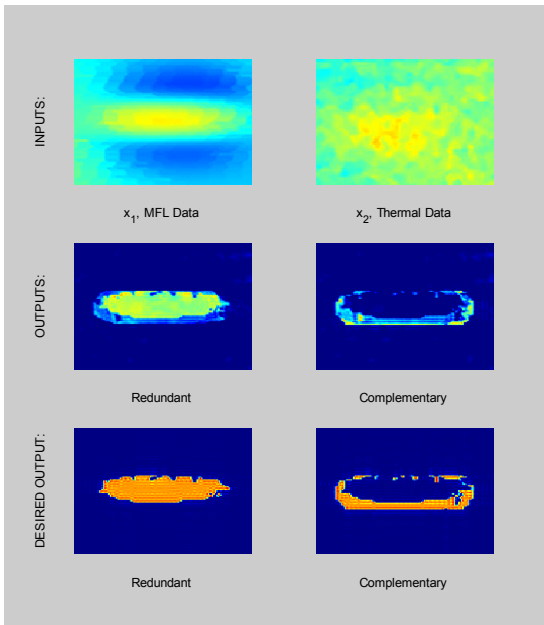
Trial 2: MFL & Thermal Results (cont.)



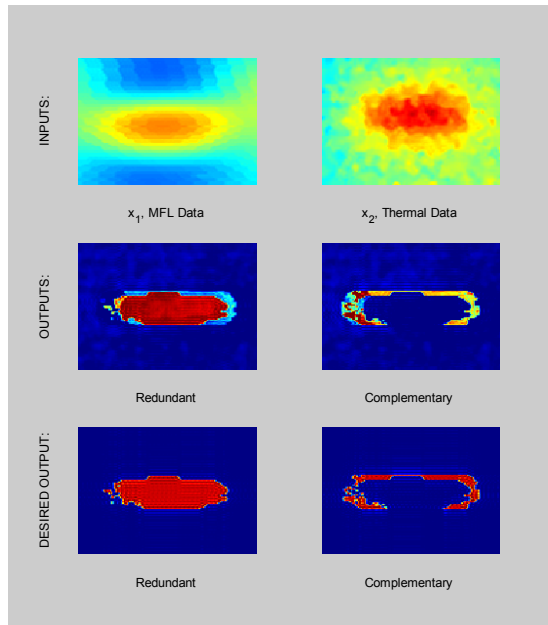
(e) Specimen 10a



(f) Specimen 13a

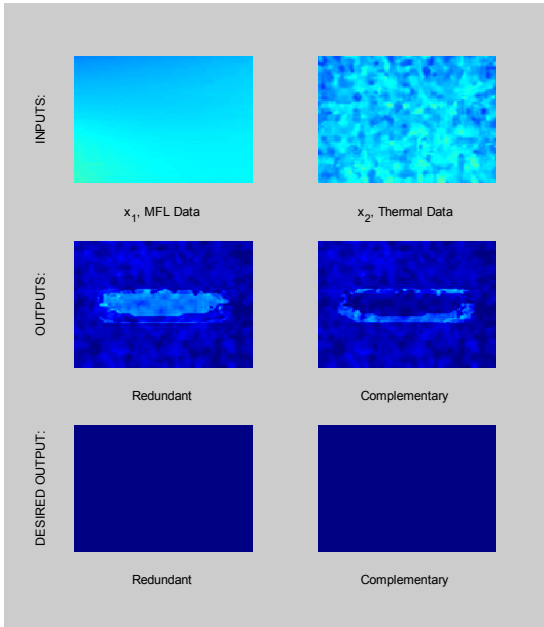


(g) Specimen 12a

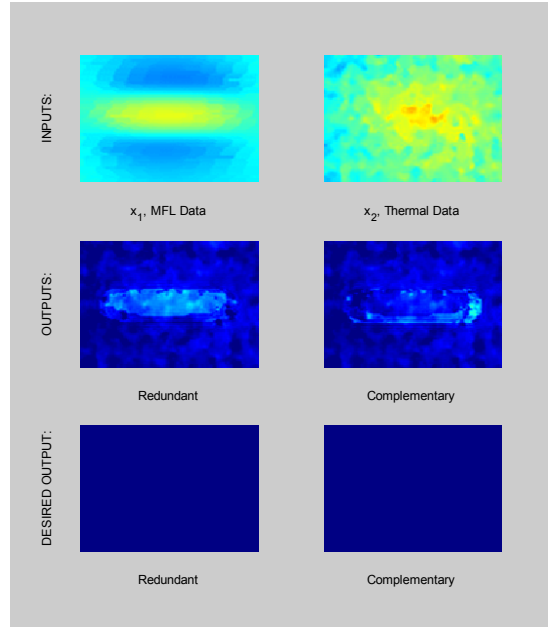


(h) Specimen 11a

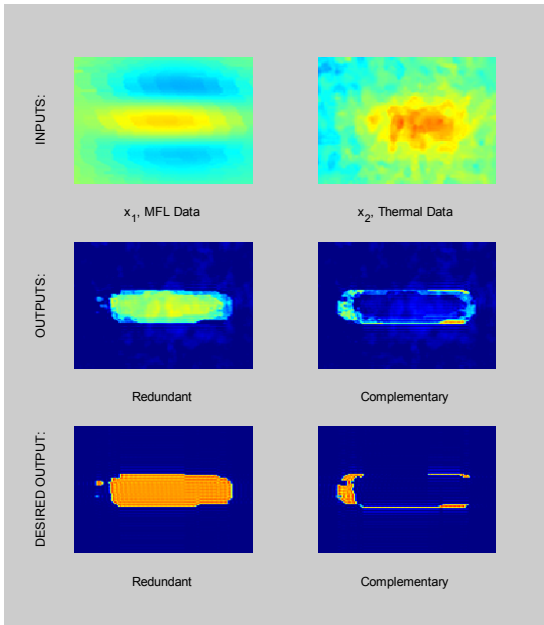
Trial 2: MFL & Thermal Results (cont.)



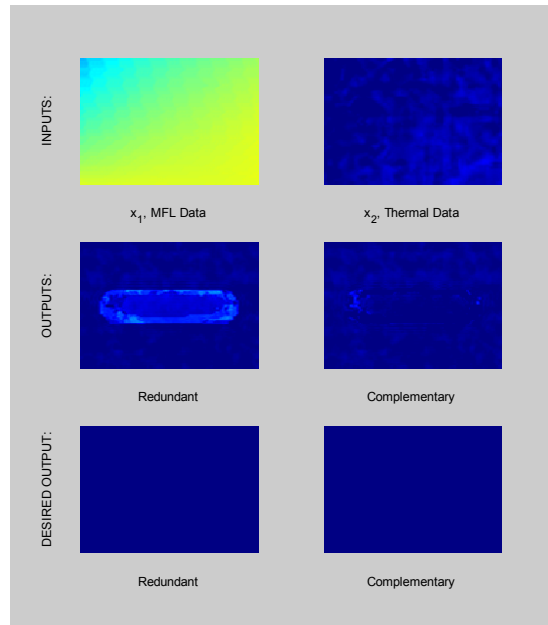
(i) Specimen 20a



(j) Specimen 23a

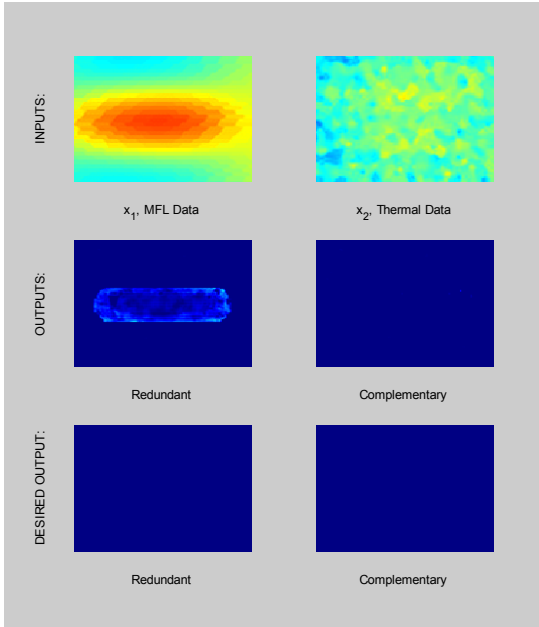


(k) Specimen 22a

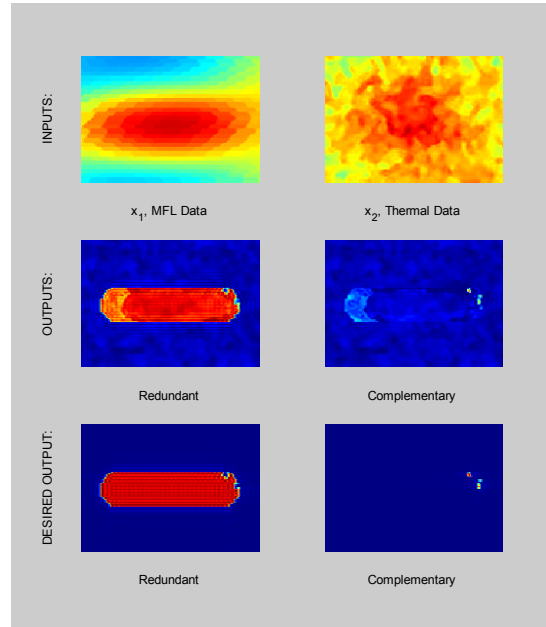


(l) Specimen 00b

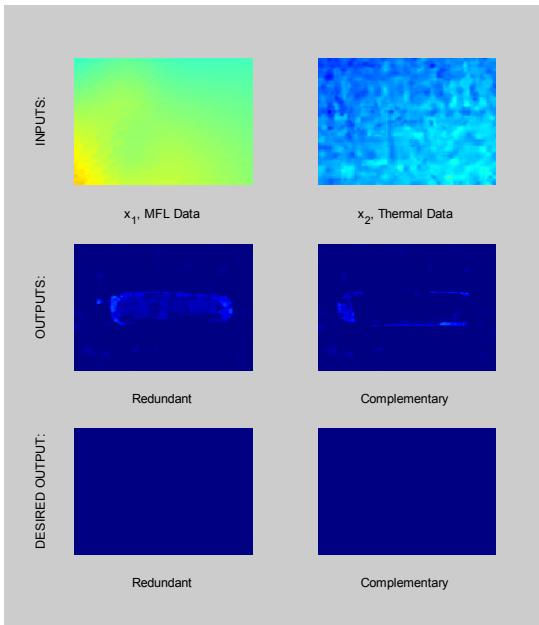
Trial 2: MFL & Thermal Results (cont.)



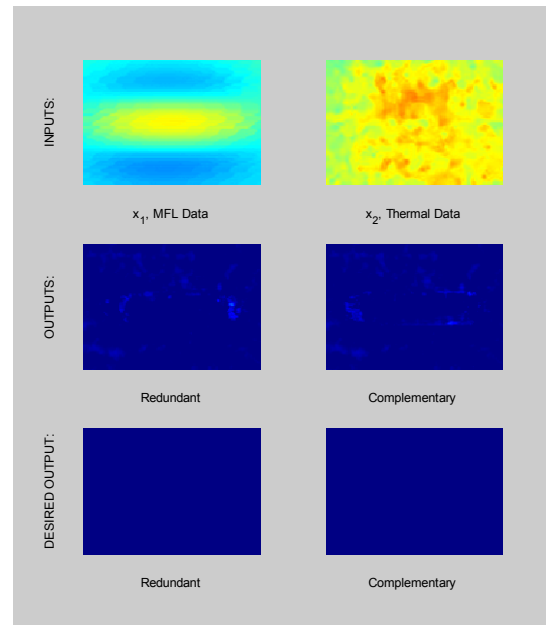
(m) Specimen 03b



(n) Specimen 01b

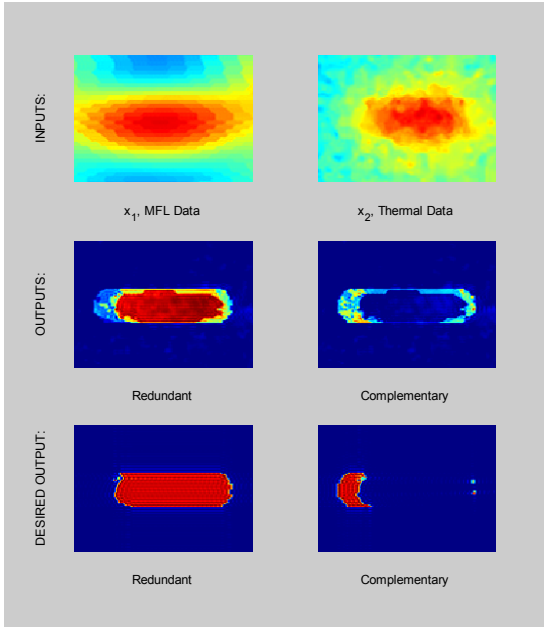


(o) Specimen 10b

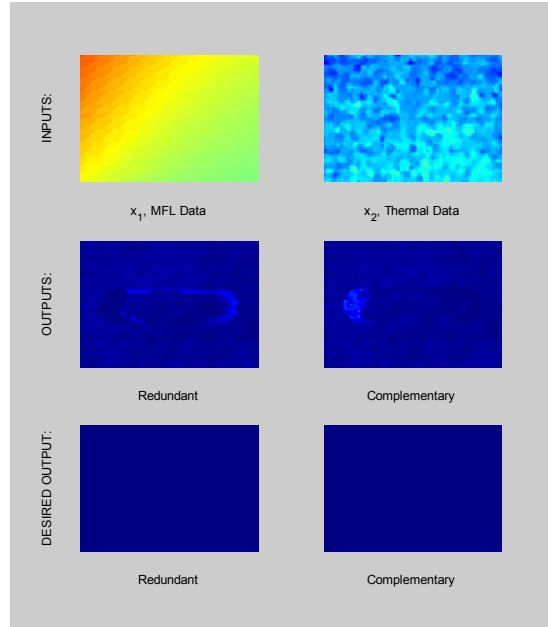


(p) Specimen 13b

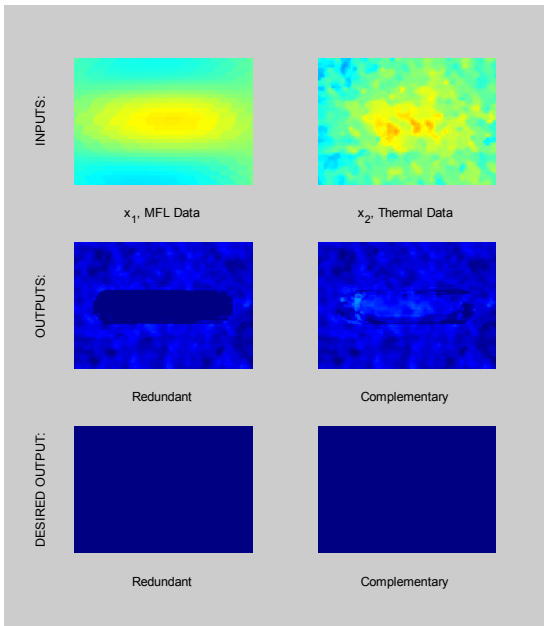
Trial 2: MFL & Thermal Results (cont.)



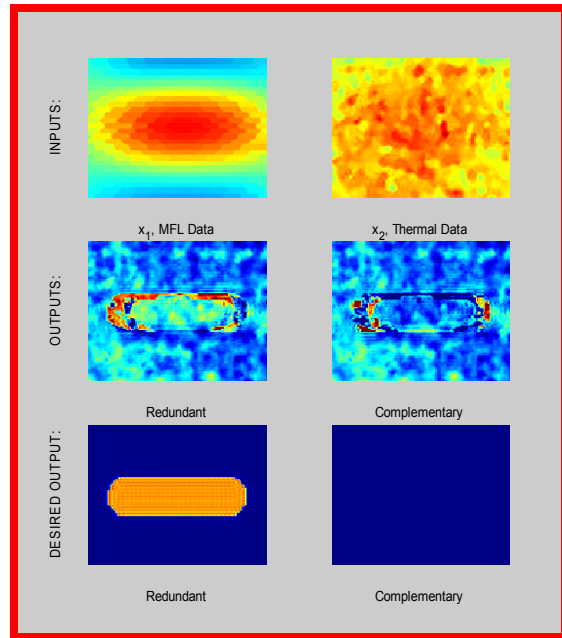
(q) Specimen 11b



(r) Specimen 20b

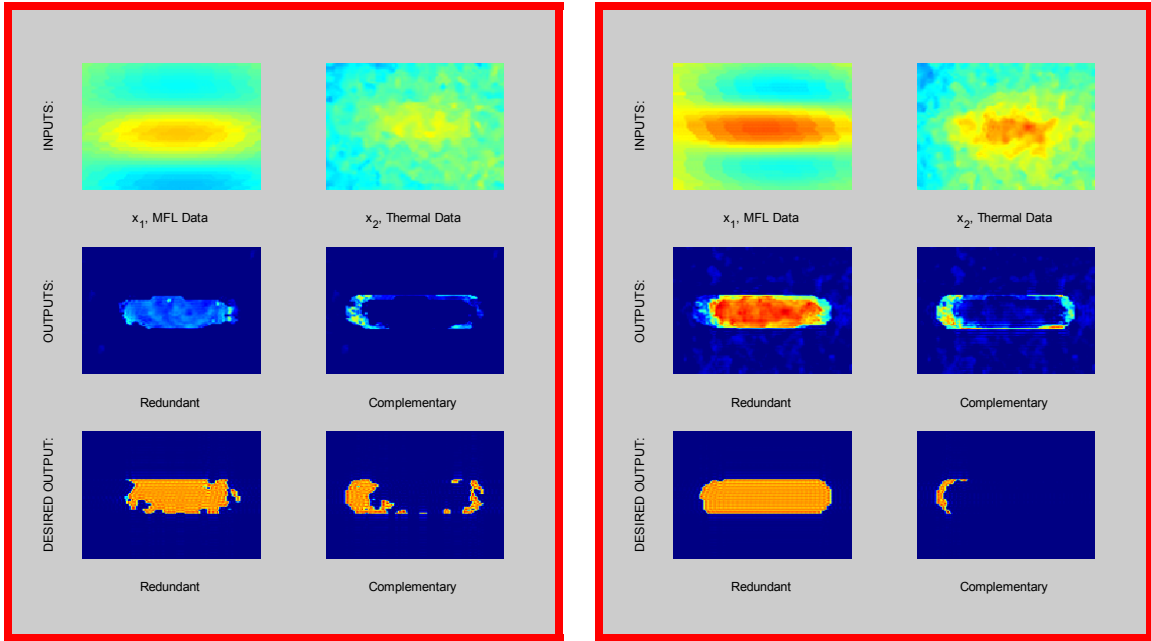


(s) Specimen 23b



(t) Specimen 02b

Trial 2: MFL & Thermal Results (cont.)



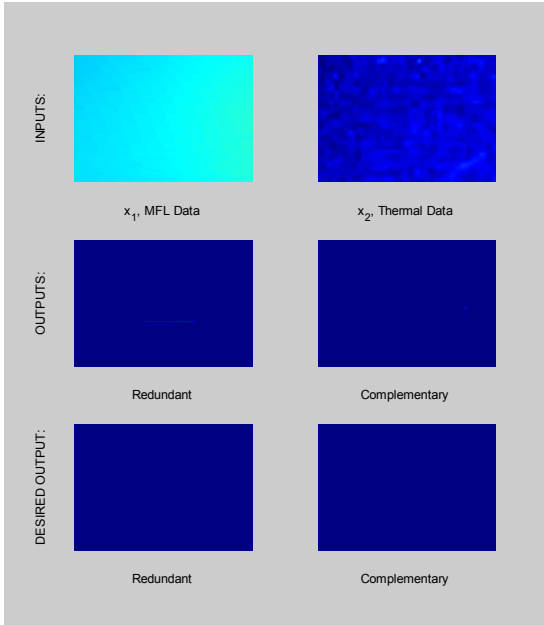
(u) Specimen 12b

(v) Specimen 22b

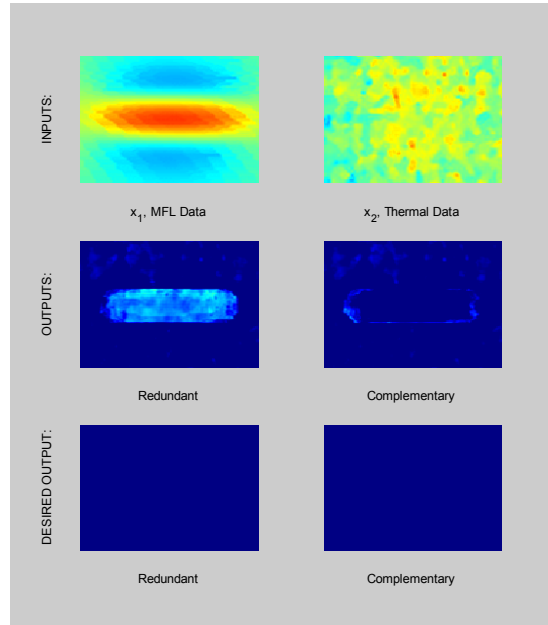
Figure 4.24: MFL & Thermal combination Trial 2.

Training Data: (a) – (s); Test Data: (t), (u), (v)

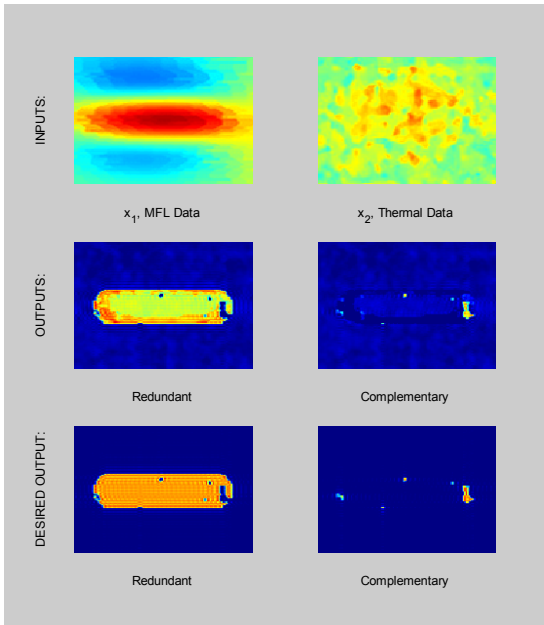
Trial 3: MFL & Thermal Results



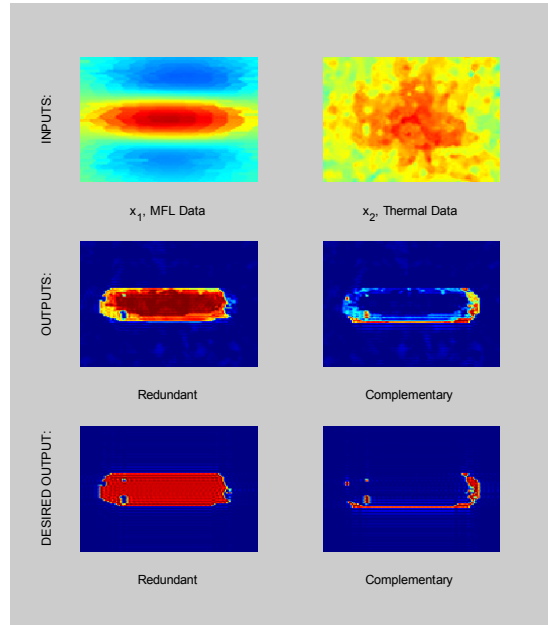
(a) Specimen 00a



(b) Specimen 03a

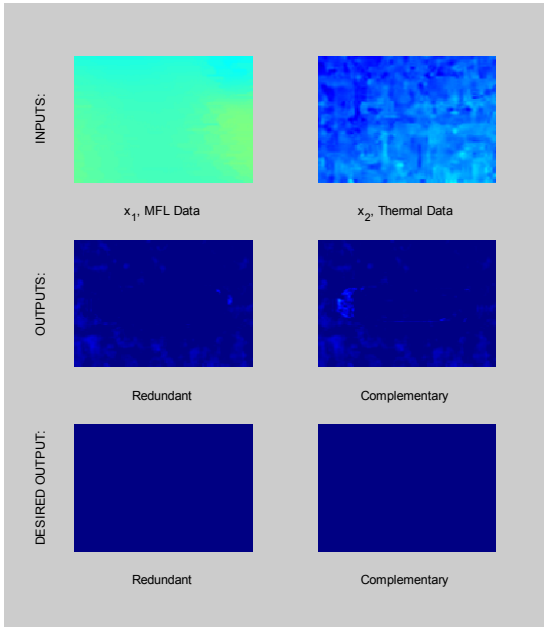


(c) Specimen 02a

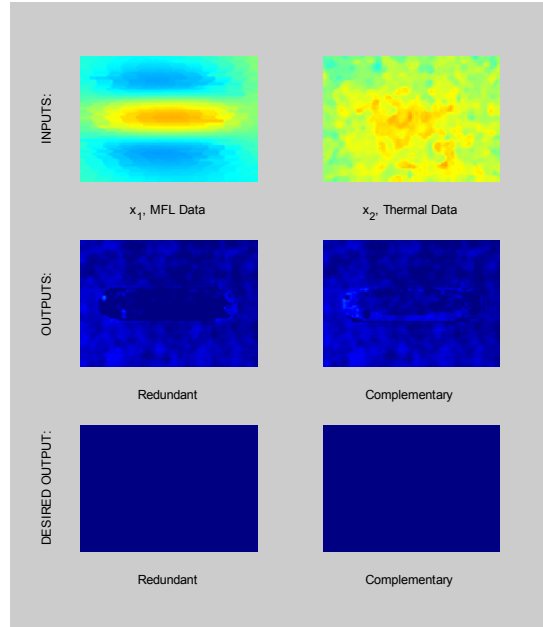


(d) Specimen 01a

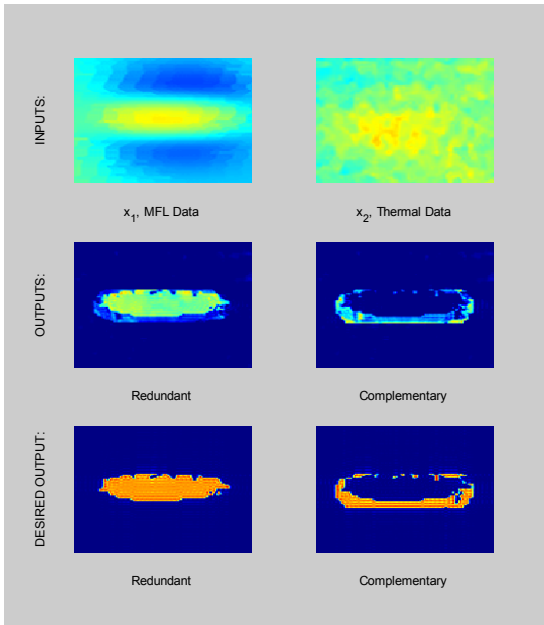
Trial 3: MFL & Thermal Results (cont.)



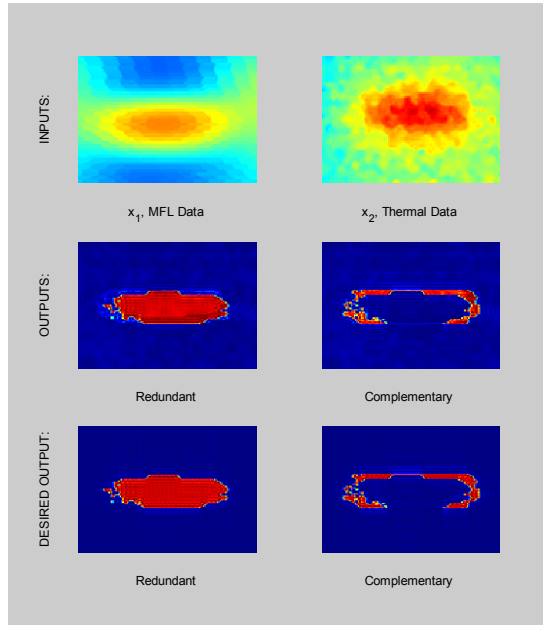
(e) Specimen 10a



(f) Specimen 13a

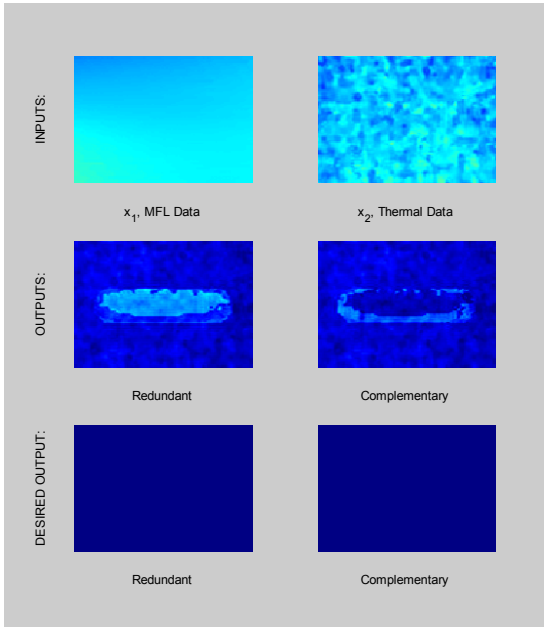


(g) Specimen 12a

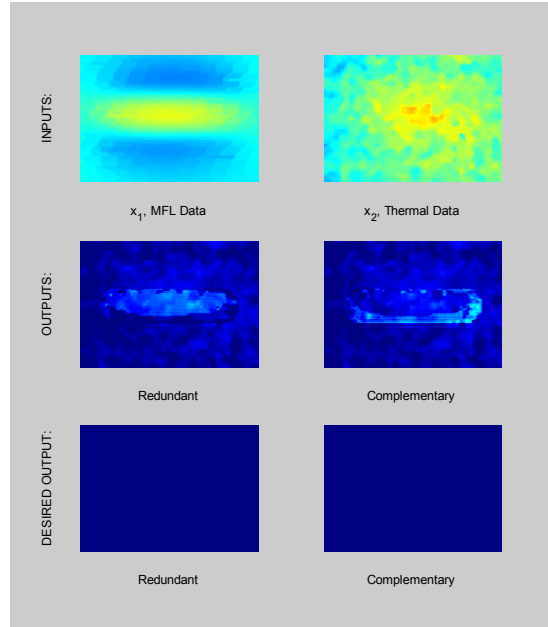


(h) Specimen 11a

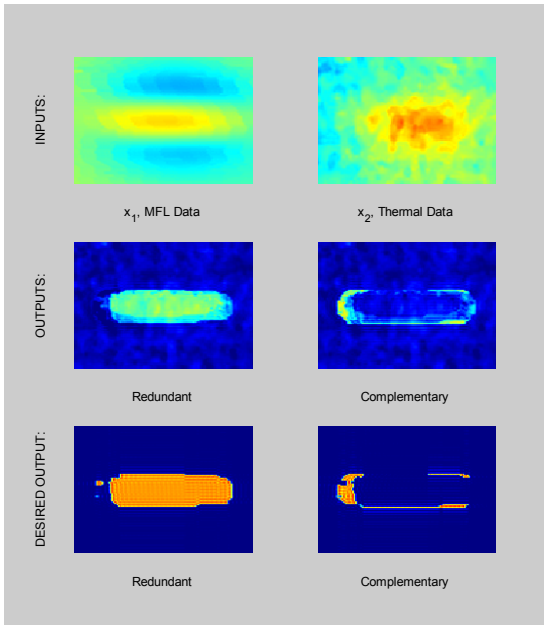
Trial 3: MFL & Thermal Results (cont.)



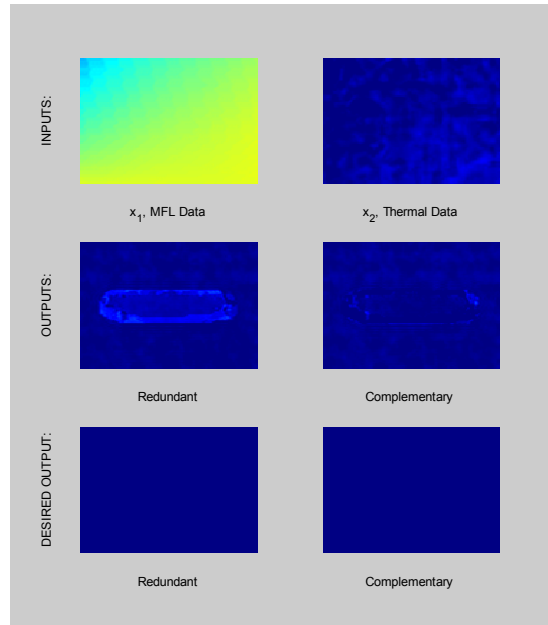
(i) Specimen 20a



(j) Specimen 23a

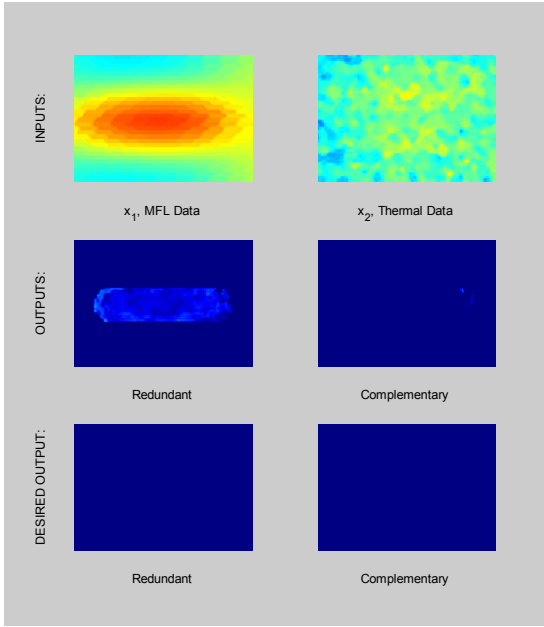


(k) Specimen 22a

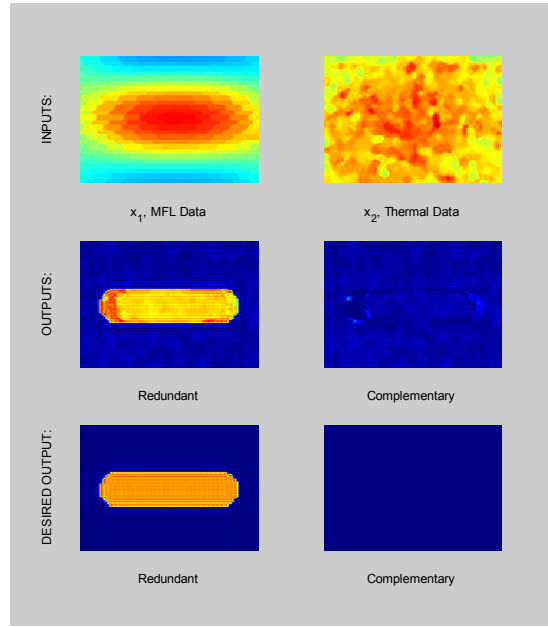


(l) Specimen 00b

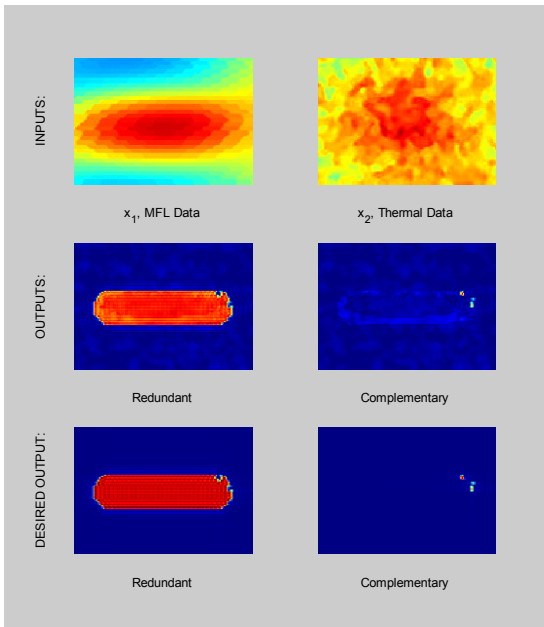
Trial 3: MFL & Thermal Results (cont.)



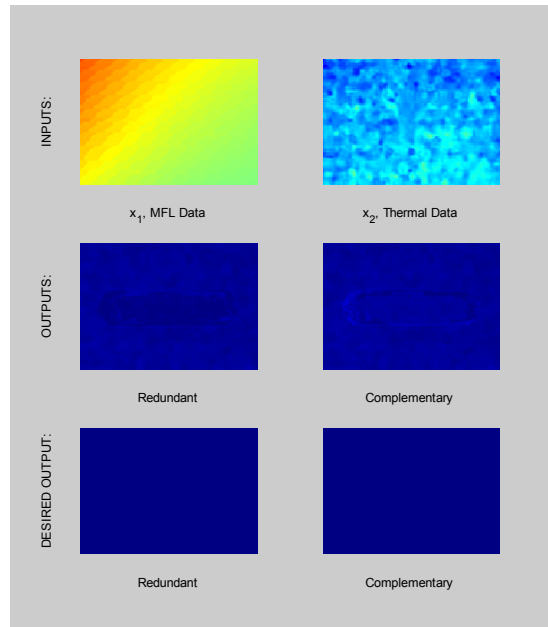
(m) Specimen 03b



(n) Specimen 02b

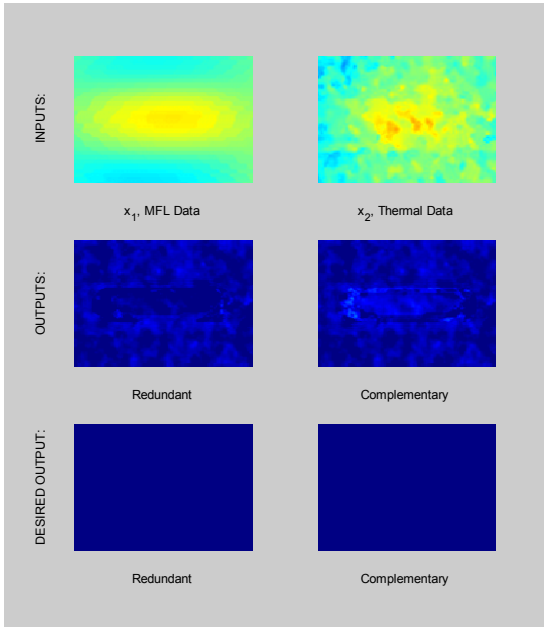


(o) Specimen 01b

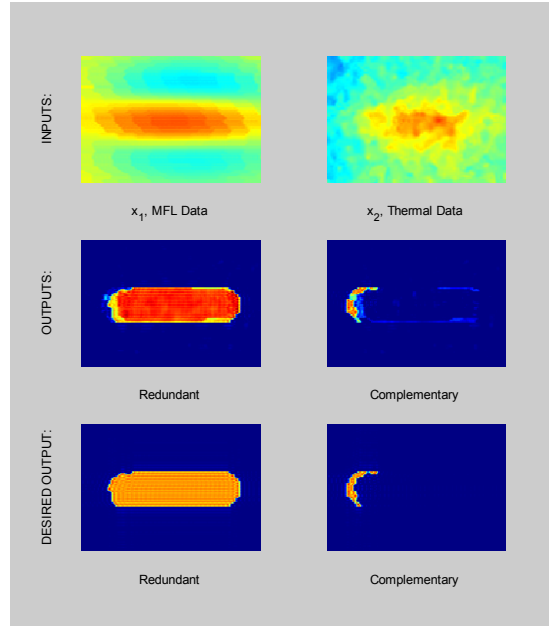


(p) Specimen 20b

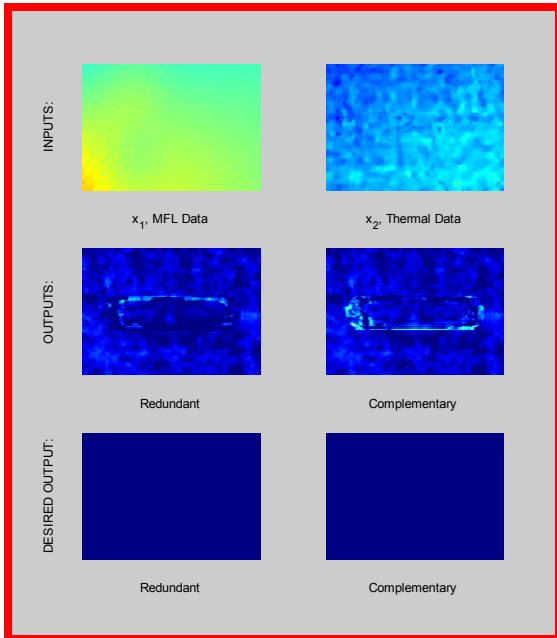
Trial 3: MFL & Thermal Results (cont.)



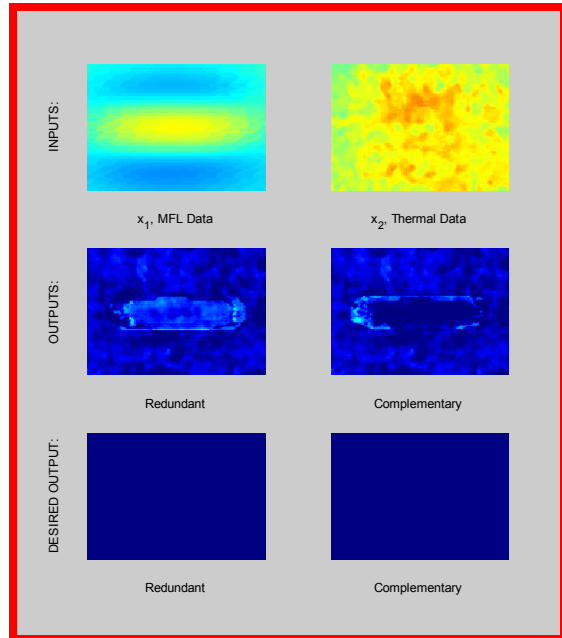
(q) Specimen 23b



(r) Specimen 22b

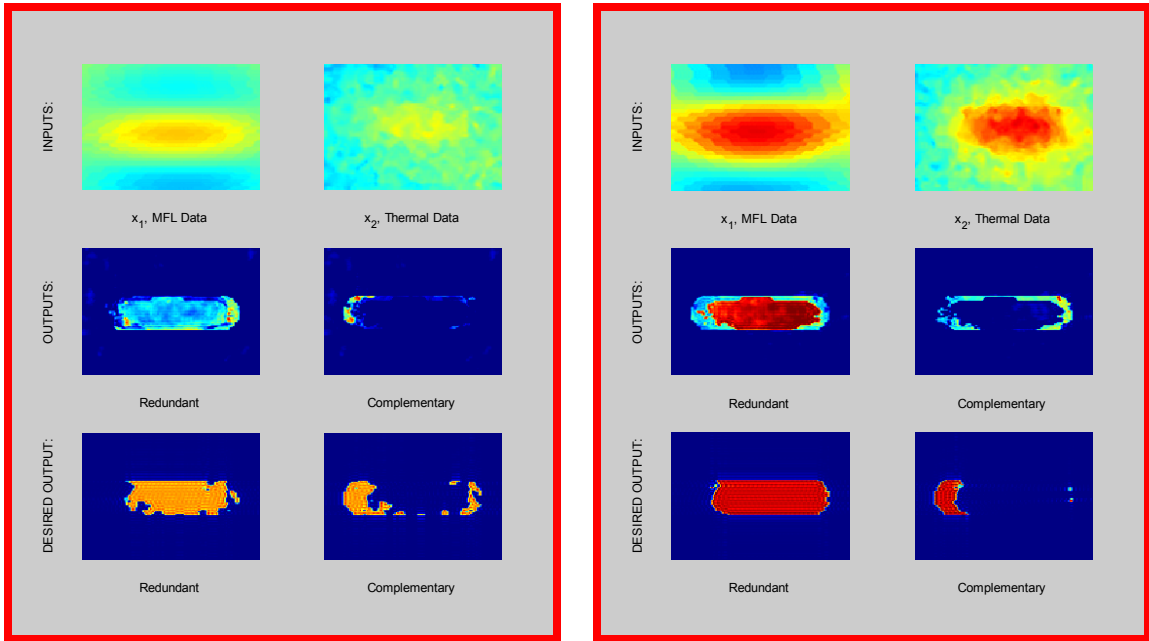


(s) Specimen 10b



(t) Specimen 13b

Trial 3: MFL & Thermal Results (cont.)



(u) Specimen 12b

(v) Specimen 11b

Figure 4.25: MFL & Thermal combination Trial 3.

Training Data: (a) – (r); Test Data: (s), (t), (u), (v)

4.2.3 Heterogeneous Data Fusion

In order to perform a redundant and complementary data extraction process on acoustic emission data it is first necessary to define how the location of AE source points corresponds to the position and shape of the actual defect. Unlike the homogeneous NDE sources, acoustic emission data does not provide the user with geometrical shape information of the defect, but only provides an estimation of where the defect is located. To perform redundant and complementary data extraction it is first necessary to relate the acoustic emission point data to a specific defect location area. Once this process has been performed the homogeneous data fusion process can be employed to extract the redundant and complementary information.

The acoustic emission testing performed in the laboratory seemed to indicate that the acoustic emission source locations do not fall directly over the defect area, but rather form clusters located around the defect. This is also evident from the acoustic emission data seen in Figure 4.15. From this information the assumption can be made that the defect is located somewhere in the area surrounded by the AE source locations. In order to perform the data fusion process it is necessary to characterize this area of the defect so it can be combined with the other NDE testing modalities. The first method in characterizing this area was to perform a K-means clustering algorithm on the raw AE data to determine how many clusters the data had been formed into and which points fell into each cluster. Figure 4.26 shows the AE data from the uniaxial specimen with the 0.16 inch deep defect (also seen in Figure 4.15 (b)) after the cluster algorithm has been performed. In this case two separate classes of data have been clearly defined on either side of the defect.

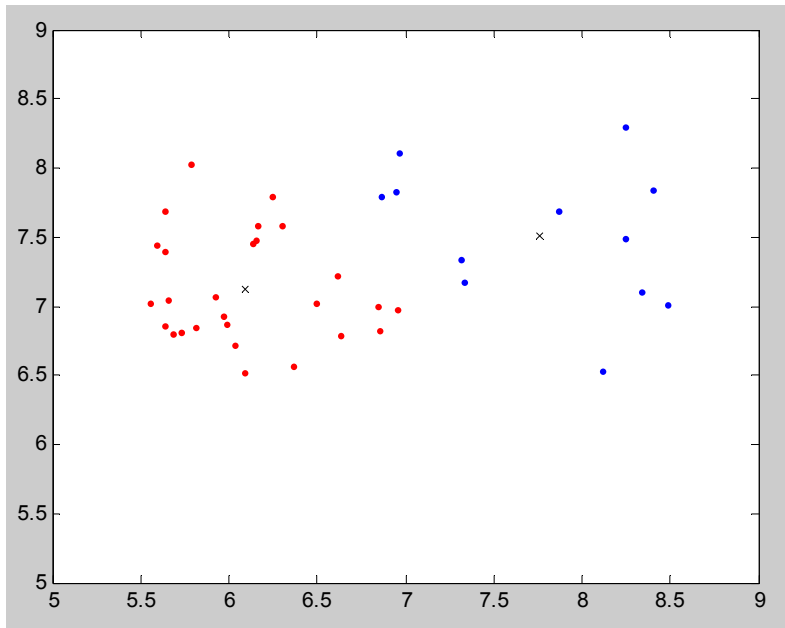


Figure 4.26: K-means clustering on AE data of uniaxial specimen with 0.16” deep defect.

After the two classes of data have been defined, a Parzen windows density estimation is performed on each class separately which can be seen in Figure 4.27. The Parzen windows approximation fits a two-dimensional Gaussian plot over each class of the data to demonstrate the areas of higher density of the AE sources.

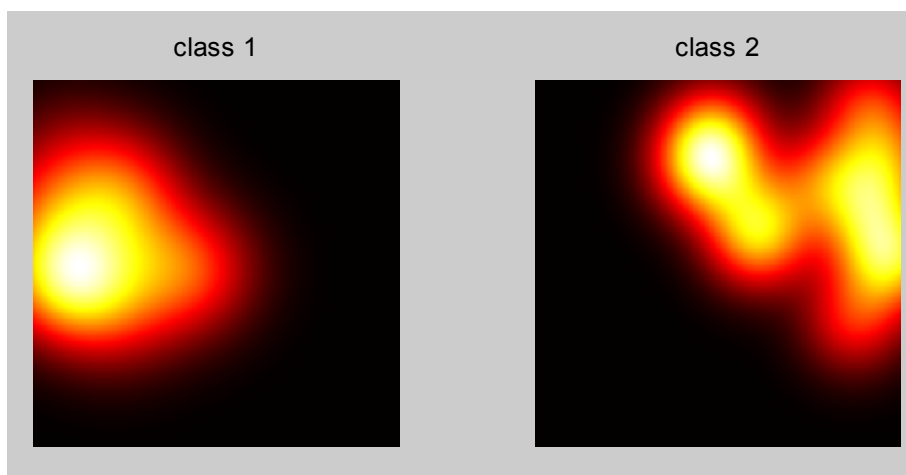


Figure 4.27: Parzen windows density estimation of each class separately.

The Parzen window images are then overlaid on top of each other. Where the density estimations overlap becomes the region in which the AE data predicts the presence of a

defect. To perform this process the Parzen window images are converted to binary images seen in Figure 4.28. A logical AND is then performed between the two image matrixes to determine where the images overlap.

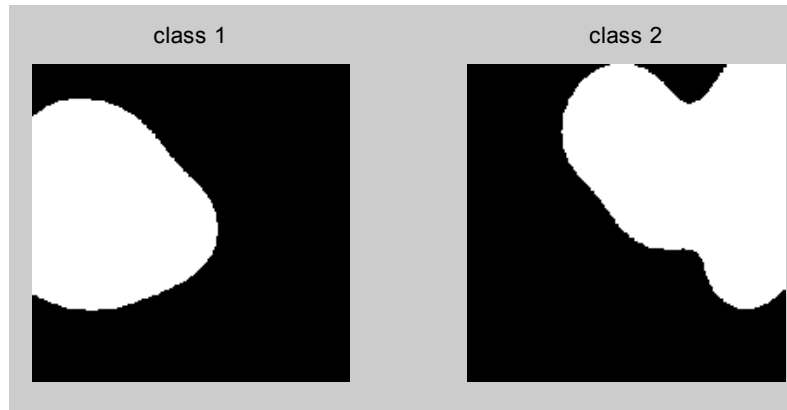


Figure 4.28: Binary representation of Parzen windows AE images.

For the AE tests performed in this project, the number of clusters of data surrounding the defect could vary from one to four classes. The overlapping areas of the Parzen windows images were then weighted from 0 to 1 in increments of 0.25, i.e., if two classes overlap, the overlapped area will be weighted at 50 percent, and for three classes overlapping 75 percent and so on. This allows for a high volume of data surrounding the defect to have a stronger influence on the data fusion process. Figure 4.29 shows the resulting defect area represented from the acoustic emission source data shown above in Figure 4.26.

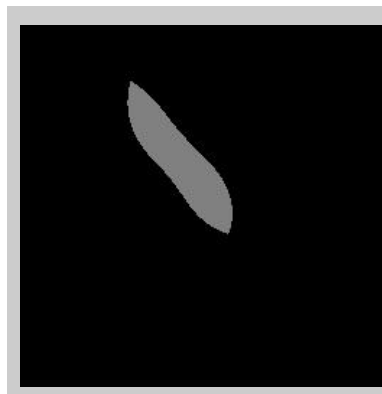


Figure 4.29: Defect location representation from AE data.

The above process was performed on all of the acoustic emission data to generate AE location estimation plots. The resulting images seen in Figure 4.30 can then be inputted to the redundant and complementary data extraction algorithm.

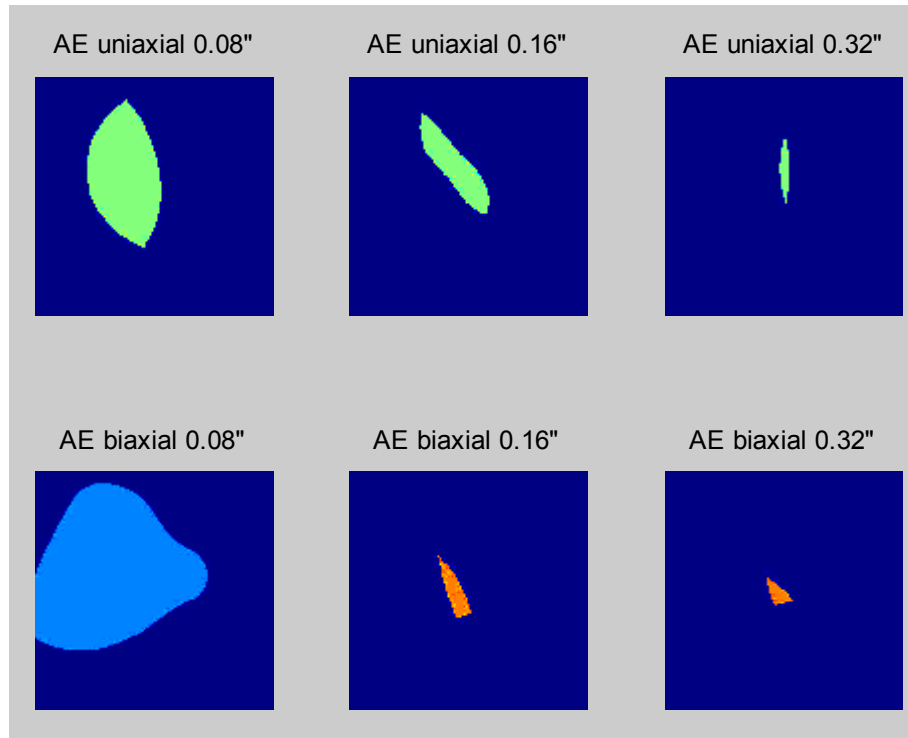


Figure 4.30: AE location estimation plots for the data fusion algorithm.

4.2.4 Heterogeneous Training and Test Datasets

The heterogeneous redundant and complementary data fusion combination process was performed on ultrasonic and acoustic emission data taken of test specimen suite 2. Since only six data instances were available for training and testing purposes only two trials were performed. Trials 1 and 2 seen in Table 4.6 and 4.7 show the division of training and test data.


Table 4.6: Trial 1 training and test dataset.

Specimen #	Type	Plate Thickness (in)	Indication	Crack Depth (in)
Uni08	Uniaxial	0.5	SCC	0.08
Uni16	Uniaxial	0.5	SCC	0.16
Uni32	Uniaxial	0.5	SCC	0.32
Bi08	Biaxial	0.5	SCC	0.08
Bi16	Biaxial	0.5	SCC	0.16
Bi32	Biaxial	0.5	SCC	0.32

 Training data
  Test data

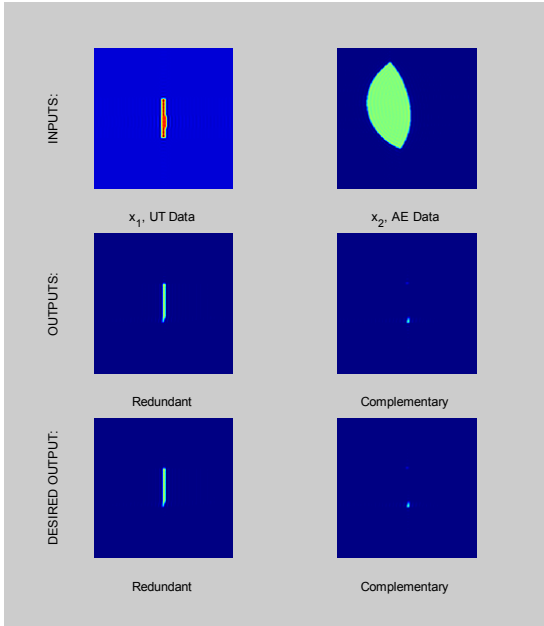
Table 4.7: Trial 2 training and test dataset.

Uni08	Uniaxial	0.5	SCC	0.08
Uni16	Uniaxial	0.5	SCC	0.16
Uni32	Uniaxial	0.5	SCC	0.32
Bi08	Biaxial	0.5	SCC	0.08
Bi16	Biaxial	0.5	SCC	0.16
Bi32	Biaxial	0.5	SCC	0.32

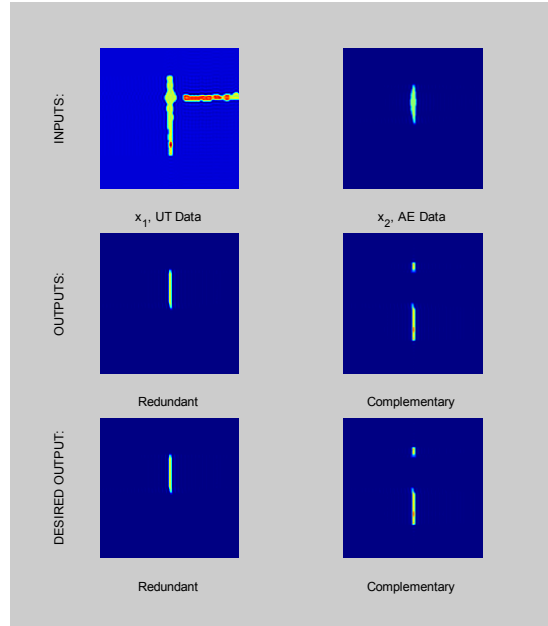
 Training data
  Test data

4.2.4.1 Acoustic Emission & Ultrasound Data Fusion Results

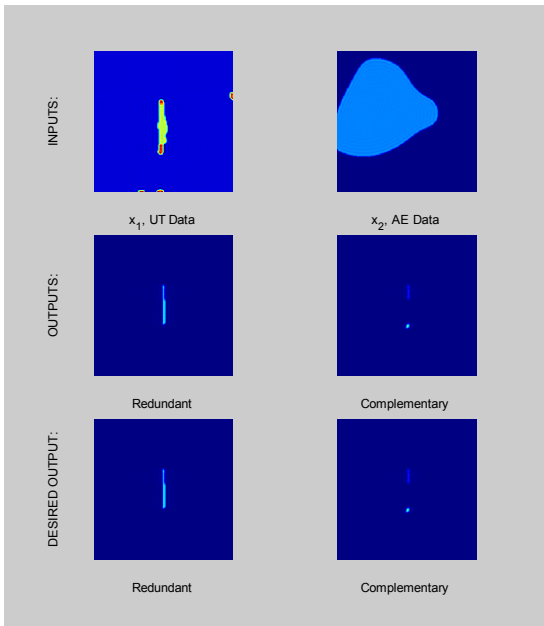
Trial 1: AE & UT Results



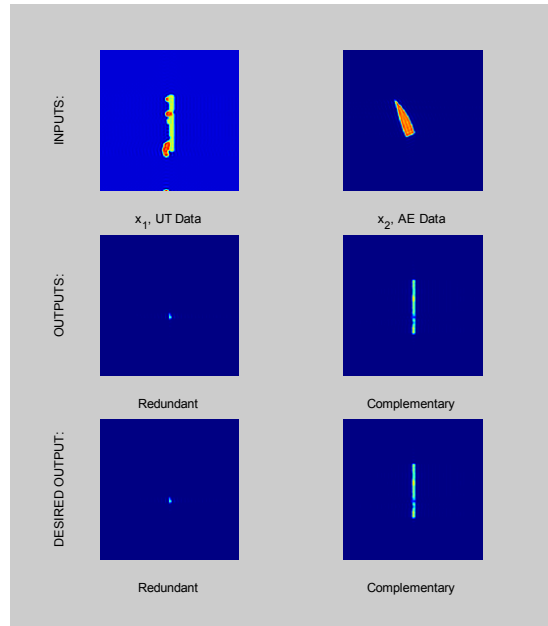
(a)



(b)

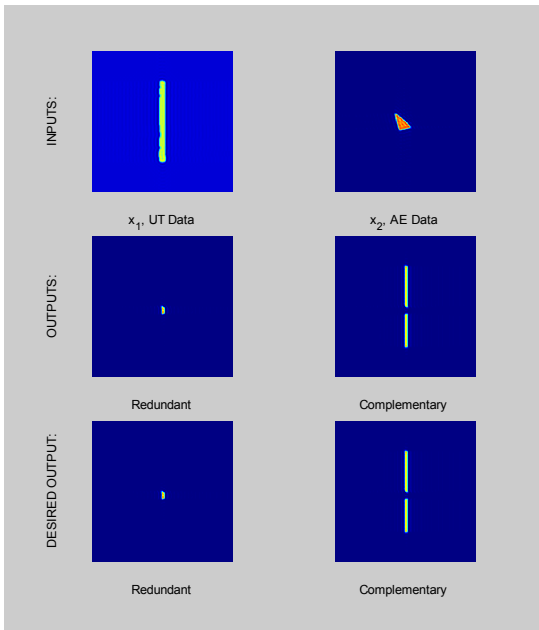


(c)

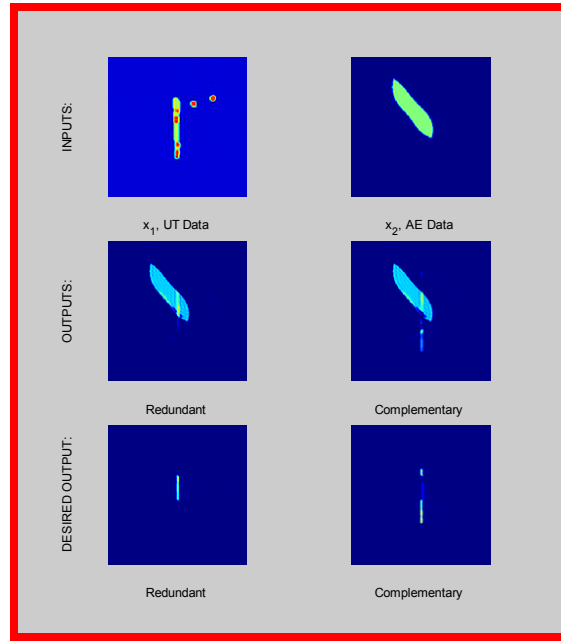


(d)

Trial 1: AE & UT Results (cont.)



(e)

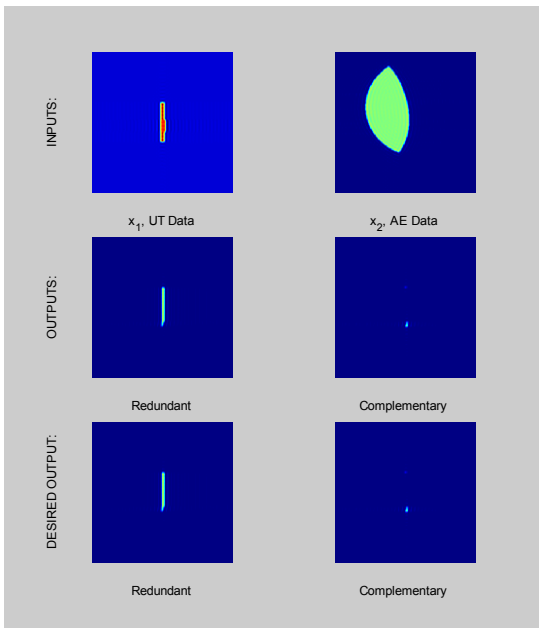


(f)

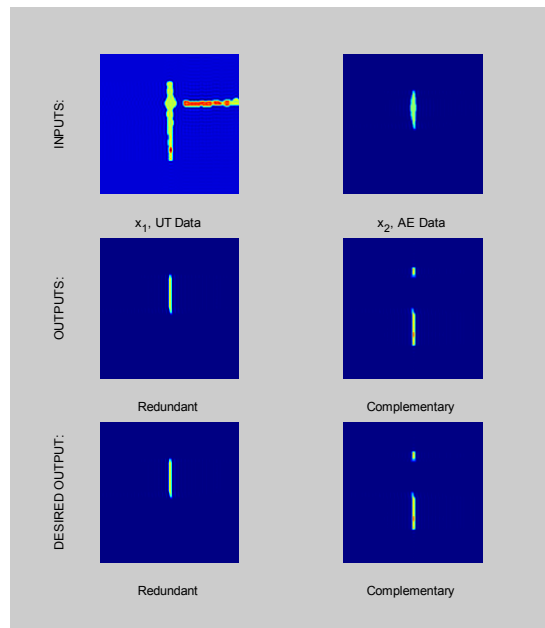
Figure 4.31: AE & UT Combination Trial 1.

Training Data: (a) – (e); Test Data: (f)

Trial 2: AE & UT Results

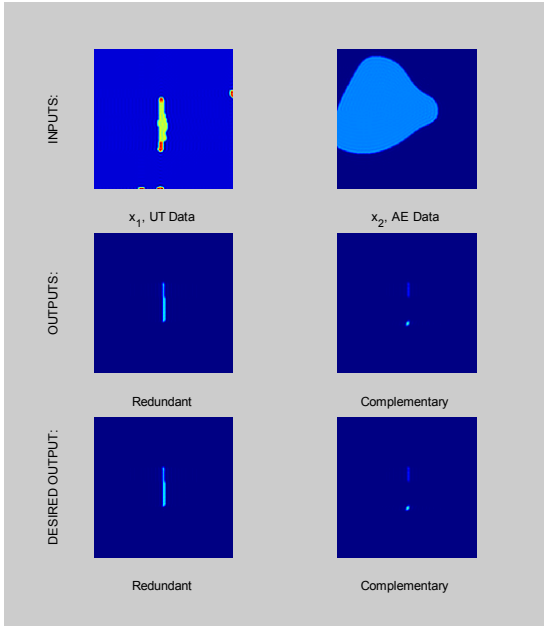


(a)

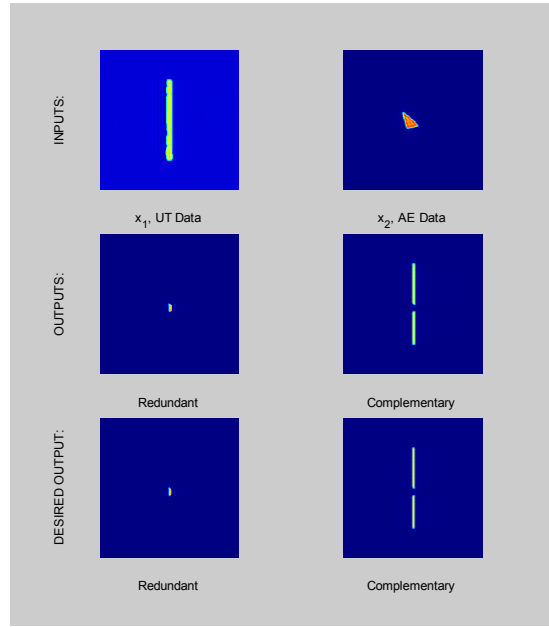


(b)

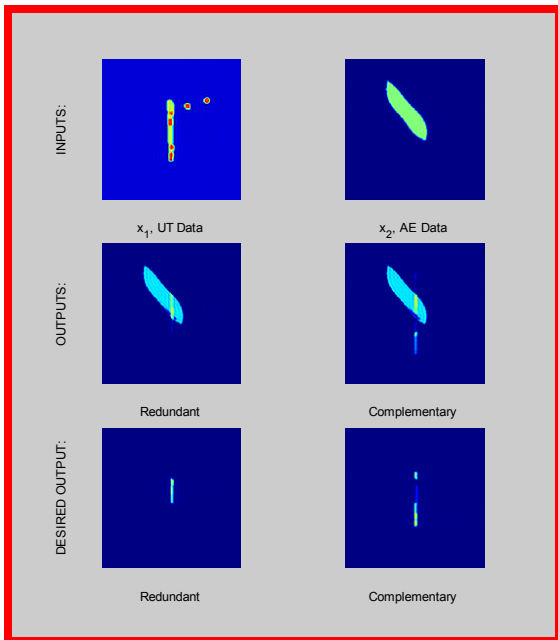
Trial 2: AE & UT Results (cont.)



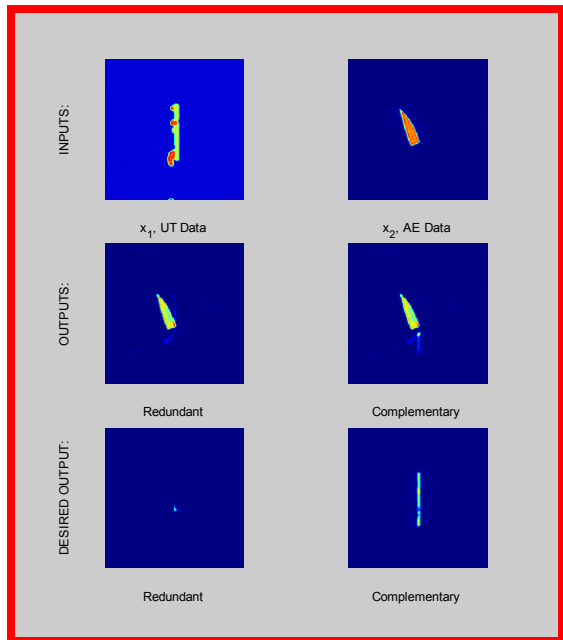
(c)



(d)



(e)



(f)

Figure 4.32: AE & UT Combination Trial 2.

Training Data: (a) – (d); Test Data: (e), (f)

4.2.5 Discussion of Results

The following observation can be made based on the data fusion results shown in Figures 4.17 through 4.25. There exists significant agreement between the predicted and desired redundant and complementary defect depth related information for all instances of training data – this indicates that the information provided to the neural network is distinct and the resulting matrices are non-singular; and is clearly visible especially the UT and MFL data combinations (see Figures 4.17, 4.18, and 4.19). The poorest performance occurs for MFL and thermal image data combinations – this is to be expected since MFL images exhibit “blooming” and cannot precisely identify the edges of the defect (see Figures 4.23, 4.24, and 4.25). This situation is worsened for thermal images where the shallowest defects are barely visible (Figures 4.11 and 4.12).

The homogeneous data fusion results shown in Figures 4.17 through 4.25 are summarized in the Figures 4.33, 4.34 and 4.35 for purposes of comparison. The mean squared error (MSE) difference between the predicted and desired fused images for both redundant and complementary information, for test data cases is shown. The following observations can be made:

1. Over all three trials, the combination UT and MFL images produces the lowest MSE for both redundant and complementary information. This is to be expected, since quantity of information related to the geometry and location of the defect is present in the following NDE methods in decreasing order: UT, MFL, thermal imaging and AE.
2. For all three NDE data fusion combination, the lowest MSE was obtained in Trial 1, where the maximum amount of training data was present. This allowed the

neural network data fusion algorithm to accurately interpolate instances of test data. The exact opposite is true of Trial 3.

3. For almost every data fusion combination and trial number, the redundant information extraction algorithm produced a lower MSE than the complementary information extraction algorithm. This is believed to be the result of the redundant training images containing more overall information than the corresponding complementary images.
4. Overall, algorithm's predicted results matched the desired output values. The total average of the MSE for all combinations of test data was only 0.0201. Very few outputs did not meet the expectations due to poor input data for that test case. All the test data outputs are highlighted red in Figures 4.17 through 4.25 where for the most part, the test data shows excellent results.

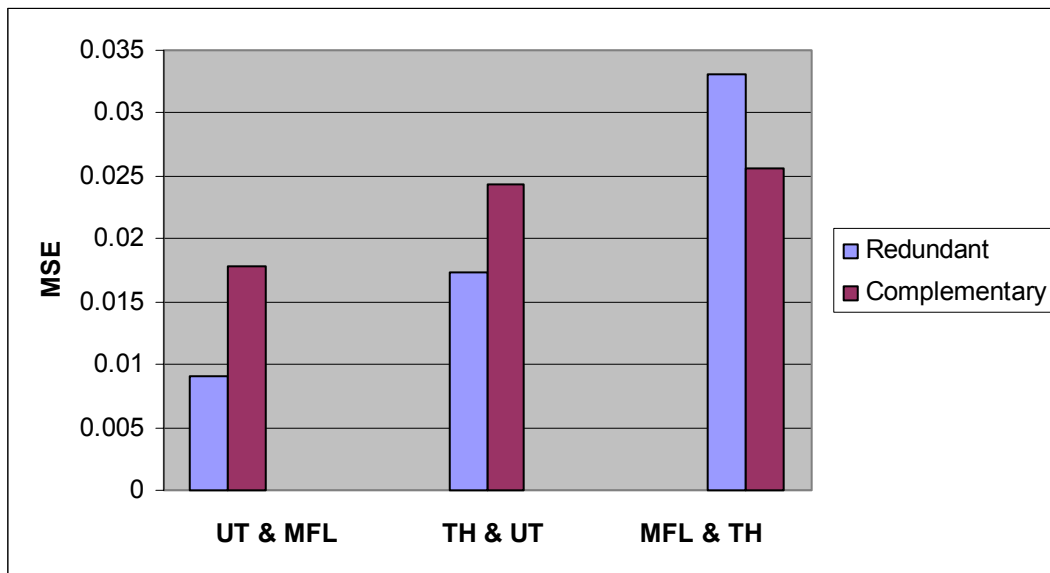


Figure 4.33: MSE plot of Trial 1 for homogeneous data fusion.

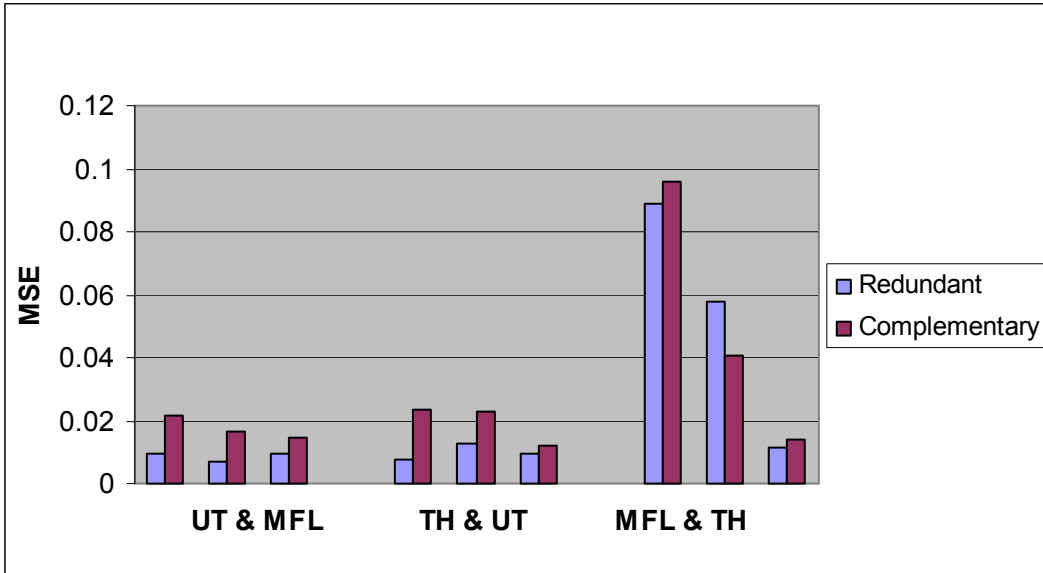


Figure 4.34: MSE plot of Trial 2 for homogeneous data fusion.

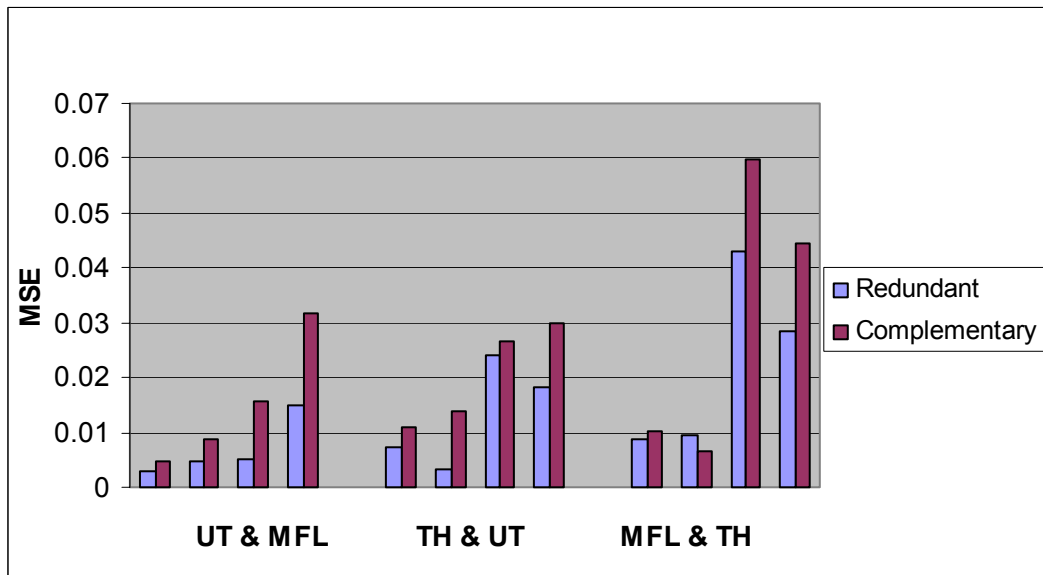


Figure 4.35: MSE plot of Trial 3 for homogeneous data fusion.

The results from the acoustic emission and ultrasound combination can be seen in Figures 4.31 and 4.32. It can be seen from these figures that both Trials 1 and 2 provided very good training data outputs with an average training output MSE of 2.86×10^{-8} . The

test results and are summarized in Figures 4.36 and 4.37 where the MSE of Trial 1 to Trial 2 for both redundant and complementary information are compared. Both Trial 1 and Trial 2 provided minimal MSE compared to the homogeneous data fusion combinations. This is despite the appearance of the actual output images seen in Figures 4.31(a) and 4.32(a) & (b) looking incorrect. In both cases the algorithm made an effort to extract the desired information and suppress the unwanted information although it was not totally successful. This is the result of very limited amount of data that was used to train the network. This procedure shows great promise due to the fact of a very minimal amount of error in the training data. With a greatly increased data it is expected the heterogeneous data fusion method will produce results comparable to that of the homogeneous data fusion method.

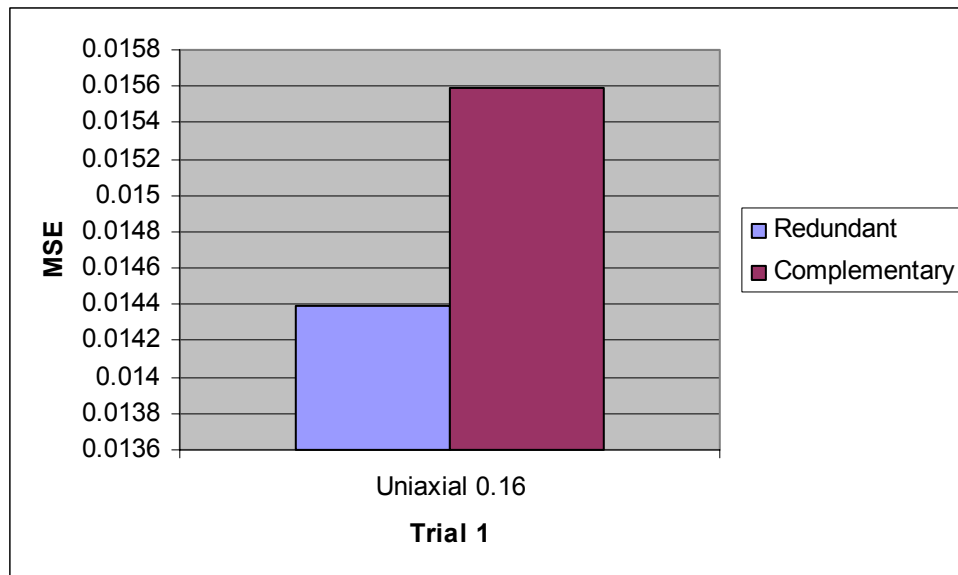


Figure 4.36: MSE plot of Trial 1 for heterogeneous data fusion.

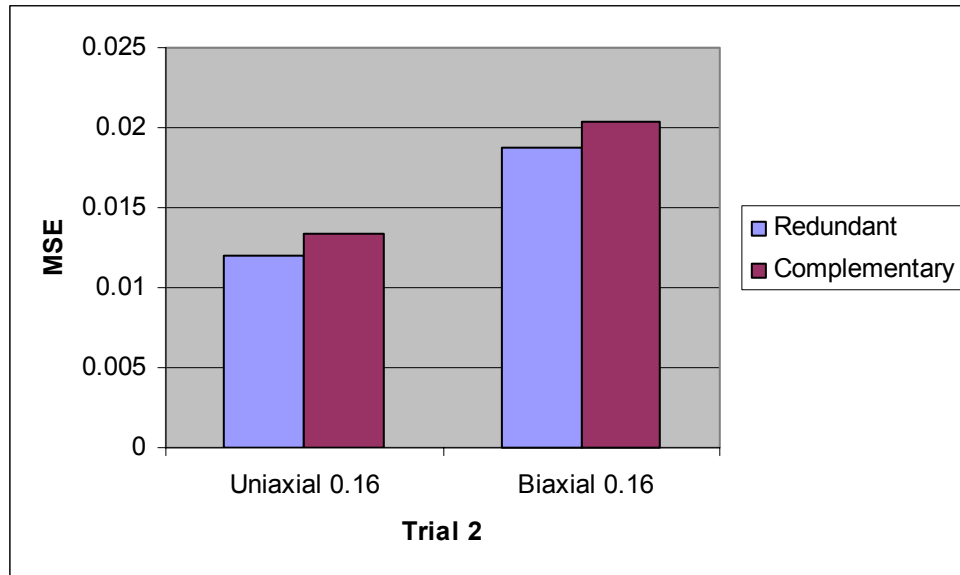


Figure 4.37: MSE plot of Trial 2 for heterogeneous data fusion.

CHAPTER 5: CONCLUSIONS

Assuring the integrity of the nation's gas transmission pipeline network is critical not only for public safety, but also for maintaining uninterrupted access to a key energy supply. Accurate and reliable determination of pipeline condition requires augmentation and improvement of current inspection tools from using single interrogation methods to multiple ones. This calls for a consequent improvement in data characterization algorithms, both in management of data volume, but also in defect characterization. This thesis has described the development and application of multi-sensor data fusion algorithms for a specific set of NDE defect characterization problems. A judicious combination of signal and image processing strategies, including geometric transformations, radial basis function approximations and Parzen windows density estimations, have been used to fuse data from both homogeneous and heterogeneous sensors. Application results using data from laboratory experiments demonstrate the consistency and efficacy of the proposed approach.

One of the principal advantages of the proposed approach for data fusion is that the method explicitly provides numerical measures of the effectiveness of the algorithm in terms of information redundancy and complementarity. Furthermore, the definitions of these quantities can change with application – although the algorithm is not required to. Such opportunities for user definition lends to the versatility of this approach, allowing for possible future applications of multi-sensor data fusion outside the realm of gas transmission pipeline NDE.

5.1 Summary of Accomplishments

The principal contributions of this thesis are listed along with the set of original objectives (that are revisited) below:

5. *The design and development of data fusion algorithms for the prediction of specific information fusion measures – redundancy and complementarity – geometric transformations in combination with radial basis function networks and Parzen windows density estimation techniques have been used.*
6. *The application of the data fusion algorithms to accurately and confidently predict the varying depth profile of surface-breaking pipe wall defects in a gas transmission pipeline – combinations of UT, MFL, thermal imaging and AE NDE data have been fused to predict defect depths in the range of 0.01” – 0.03” for pipe-wall specimens of thicknesses 5/16” – 1/2”. The average MSE between the predicted and desired values for the training and test data for all the combinations is 0.0028 and 0.0201 respectively.*
7. *The demonstration of the algorithms ability to fuse data from multiple homogeneous and heterogeneous sensors – redundant and complementary information related to the location and size of a pipe-wall defect was predicted using homogeneous data combinations that include UT-MFL, UT-thermal imaging and MFL-thermal imaging; the heterogeneous data combination includes UT-AE.*
8. *The design and development of experimental validation test platforms and protocols for measuring the efficacy of the data fusion techniques – a biaxial loading test platform was developed for obtaining AE signatures; standard*

protocols were used for obtaining UT, MFL and thermal imaging NDE signatures. A comprehensive test specimen suite was fabricated to be indicative of gas transmission pipe-wall anomalies. Multiple scans were obtained from the test specimens and database of approximately 500 NDE signatures was created.

5.2 Directions for Future Work

Although, the research work presented in this thesis demonstrates that the stated objectives have been met, many concerns and issues still require attention to develop more versatile and comprehensive data fusion information extraction methods. This is essential to the security and viability of the nation's natural gas transmission pipeline infrastructure. The objectives of this thesis have been met as evident from the results presented, but a considerable amount of research still must be applied before this multi-sensor data fusion technique can be used an industry level. Future developments of this research should include:

1. Additional acoustic emission data must be gathered in order to rigorously test the heterogeneous data fusion algorithm. Multiple specimens must be fabricated that can accommodate the acoustic emission loading platform as well as the ultrasonic scanning, MFL, and thermal imaging test setups.
2. The current data fusion procedure must be adapted to include the combination of information from singular events such as: time-history, anecdotal evidence, and a priori knowledge.

3. In order to truly test the data fusion algorithm, actual pipeline data must be obtained or collected. At this point, modifications can be made to adapt the algorithm for real world NDE data as opposed to current experimental data.
4. Apply the data fusion algorithms to applications outside the NDE realm to test its versatility. A possible application could be hardware implementation such as the development of a smart sensor system.
5. Incorporate the data fusion algorithm into the virtual reality platform for use in data integration, visualization, and data management. This is essential due to the vast amounts of data generated from NDE inspection of gas transmission pipelines.

The accomplishment of these tasks could help to play a vital role in the safety and future of the natural gas transmission pipeline network. As the current infrastructure continues to age, it is extremely important that multi-sensor data fusion methods such as those described in this thesis are implemented and put into action. No longer can a single NDE inspection method characterize the rapidly changing pipeline. It is anticipated that the methods and techniques developed in this thesis will play a significant role in the future on the nation's natural gas transmission pipeline network.

BIBLIOGRAPHY

1. The Federal Aviation Administration, "Managing the aging aircraft problem," FAA Airport and Aircraft Safety R&D Division, October 2001.
http://aar400.tc.faa.gov/Programs/AgingAircraft/Seher_Manchester.pdf
2. Federal Highway Administration, "Better roads & bridges: using new technology to improve mobility and productivity," 1998.
<http://www.cerf.org/PDFs/COLLAB/ptp/ptpch2%2C3.pdf>
3. The Road Information Program (TRIP), "The condition of New Jersey's roads and bridges," October 2000. <http://www.tripnet.org/NewJerseyReport.PDF>
4. The Website for the Power Industry, "Terrorist threat to nuclear power plants," 2004. <http://www.power-technology.com/contractors/nuclear/nuclear-terrorism.html>
5. C. Braun, F. Steinhausler, "International terrorists threat to nuclear facilities," Center for International Security and Cooperation, Stanford University, CA. November 2002. <http://www.numat.at/list%20of%20papers/braun.pdf>
6. Alliance for Energy & Economic Growth, "Energy Infrastructure: Natural Gas Transmission Pipelines," March 2003.
http://www.youenergyfuture.com/docs/sheet_transmission_pipelines.pdf.
7. L. Udpa, S. Mandayam, S. Udpa, Y. Sun and W. Lord, "Developments in gas pipeline technology," *Materials Evaluation*, April 1996, pp. 467-472.
8. Stanley Ness, Patrick Moore, *Nondestructive Testing Handbook: Volume 10 Nondestructive Testing Overview*, American Society for Nondestructive Testing, Inc., 1996.
9. Don E. Bray and Roderic K. Stanley, *Nondestructive Evaluation: A Tool in Design, Manufacturing, and Service*, CRC Press, Boca Raton, 1997.
10. NDT Resource Center, *NDT Education Resources*, Iowa State University, 2004.
<http://www.ndt-ed.org/EducationResources/educationresource.htm>
11. Schmerr, Lester W. *Fundamentals of Ultrasonic Nondestructive Evaluation*, Plenum Press, New York 1998.
12. J. Oagaro, P. Kulick, M. Kim, R. Polikar, J. Chen, S. Mandayam, "A multi-sensor data fusion system for assessing the integrity of gas transmission pipelines," *Proceedings of Natural Gas Technologies II Conference*, Phoenix, Arizona, February 2004.

13. P. Kulick, *Multi-Sensor Data Fusion Using Geometric Transformations For The Nondestructive Evaluation Of Gas Transmission Pipelines*, Masters Thesis, Rowan University, Glassboro, NJ, 2003.
14. David L. Hall and James Llinas, *Handbook of Multi-sensor Data Fusion*, CRC Press, Boca Raton, 2000.
15. Lawrence A. Klien, *Sensor and Data Fusion Concepts and Application*, SPIE Optical Engineering Press, 1999.
16. M. Mina, J. Yim, S. S. Udpa, L. Udpa, W. Lord and K. Sun, "Two-dimensional multi-frequency eddy current data fusion," *Review of Progress in Quantitative Nondestructive Evaluation*, Vol. 15, Plenum Press, New York, 1996.
17. X. E. Gros, J. Bousigue and K. Takahashi, "NDT data fusion at pixel level," *NDT&E International*, Vol. 32, 1999.
18. D. Horn and W. R. Mayo, "NDE reliability gains from combining eddy-current and ultrasonic testing," *NDT&E International*, Vol. 33, 2000.
19. S. Gautier, B. Lavayssiere, E. Fleuet and J. Idier, "Using complementary types of data for 3D flaw imaging," *Review of Progress in Quantitative Nondestructive Evaluation*, Vol. 17, Plenum Press, New York, 1998.
20. J. Yim, *Image Fusion Using Multi-resolution Decomposition and LMMSE filter*, PhD Dissertation, Iowa State University, Ames, Iowa, 1995.
21. Albert Birks, Robert Green Jr., Paul McIntire, *Nondestructive Testing Handbook: Volume 7 Ultrasonic Testing*, American Society for Nondestructive Testing, Inc. 1991.
22. B. Nestleroth, "Magnetic flux leakage (MFL) technology for natural gas pipeline inspection," Battelle, February 1999.
<http://www.battelle.org/pipetechnology/MFL/MFL98Main.html>
23. Physical Acoustic Corporation, *Acoustic Emission Measurement Technologies*, Princeton, NJ, 2004.
<http://www.pacndt.com/index.aspx?go=research&focus=/capabilities/AE%20Research.htm>
24. Ming Jiang, *Digital Image Processing: Geometric Transformations*, Department of Information Science, University of Iowa, September 2003.
<http://ct.radiology.uiowa.edu/~jiangm/courses/dip/html>
25. Rafael Gonzalez, Richard Woods, *Digital Image Processing*, Prentice Hall Inc. New Jersey, 2002.

26. Richard Duda, Peter Hart, David Stork, *Pattern Classification*, John Wiley & Sons, Inc. 2001.
27. S. Theodoridis, K. Koutroumbas, *Pattern Recognition*, Academic Press, Boston, 2003.
28. R. Schalkoff, *Pattern Recognition: Statistical, Structural and Neural Approaches*, John Wiley & Sons Inc. New York, 1992.
29. Robi Polikar, "Lecture 8: non-parametric density estimation", *Theory and Applications of Pattern Recognition*, Rowan University, Electrical and Computer Engineering, Glassboro, NJ 08028, October 2003.
http://users.rowan.edu/~polikar/CLASSES/ECE504_04/Lecture8.pdf
30. K. Hwang, S. Mandayam, S. S. Udpa, L. Udpa, W. Lord and M. Afzal, "Characterization of gas pipeline inspection signals using wavelet basis function neural networks," *NDT & E International*, Volume 33, Issue 8, pp. 531-545, December 2000.
31. S. Mandayam, L. Udpa, S. S. Udpa and W. Lord, "Invariance transformations for magnetic flux leakage signals," *IEEE Transactions on Magnetics*, Vol. 32, No. 3, pp. 1577-1580, May 1996.
32. S. Mandayam, *Invariance Transformations for Processing NDE Signals*, PhD Dissertation, Iowa State University, Ames, Iowa, 1996
33. M. Ciocco, J. Neyhart, S. Mandayam, K. Jahan, D. B. Cleary, "Ultrasonic imaging of defects in concrete pipelines," *Proceedings of 28th Annual Review of Progress in Quantitative NDE*, American Institute of Physics, New York, July 2001.
34. M. Ciocco, *An Invariance Transformation Algorithm for Defect Characterization of Ultrasonic Signals for the Nondestructive Evaluation of Concrete*, Masters Thesis, Rowan University, Glassboro, NJ 08028, 2002.
35. Simon Haykin, *Neural Networks: A Comprehensive Foundation*, Prentice Hall Inc. New Jersey, 1999.